 ©2014 Uspekhi Fizicheskikh Nauk, Russian Academy of Sciences

REVIEWS OF TOPICAL PROBLEMS PACS numbers: 14.80.Nb, **95.35.+d**, 98.70.Rz

Small-scale clumps of dark matter

V S Berezinsky, V I Dokuchaev, Yu N Eroshenko

DOI: 10.3367/UFNe.0184.201401a.0003

Contents

V S Berezinsky Gran Sasso Science Institute (GSSI)
and Laboratori Nazionali del Gran Sasso, INFN,
I-67010 Assergi (AQ), Italy
E-mail: berezinsky@lngs.infn.it
V I Dokuchaev, Yu N Eroshenko Institute for Nuclear Research,
Russian Academy of Sciences,
prosp. 60-letiya Oktyabrya 7a, 117312 Moscow, Russian Federation
E-mail: dokuchaev@lngs.infn.it, eroshenko@inr.ac.ru

Received 6 May 2013
Uspekhi Fizicheskikh Nauk **184** (1) 3 – 42 (2014)
DOI: 10.3367/UFNr.0184.201401a.0003
Translated by K A Postnov; edited by A M Semikhatov

Abstract. Small-scale clumps of dark matter are gravitationally bounded structures that have masses comparable to or lower than stellar masses and consist of noninteracting or weakly interacting dark matter particles. In this paper, the current knowledge about the formation and evolution of such structures is reviewed, various types of spectra of primordial cosmological perturbations are considered, and various dark matter models are discussed. Depending on the particular spectrum type, dark matter clumps may differ considerably in their formation processes and ultimate characteristics. The role of clumps in experiments on indirect detection of dark matter particles via their annihilation products is discussed. A number of astrophysical problems and phenomena that are related to dark matter clumps are examined.

1. Introduction

Modern cosmology (see monographs [1–5], review [6], and historical overview [7]) studies the most fundamental problems of the origin of our Universe by combining the physics of elementary particles and quantum field theory, especially as regards studying the very early epochs. The inflationary paradigm as part of quantum cosmology should be specially mentioned here. This paradigm offers elegant solutions to several cosmological problems simultaneously, but the specific model of inflation remains to be chosen.

The study of the nature of dark matter and dark energy that are present in the Universe is another important field of modern cosmology. The importance of these substances of an unknown nature is dictated by their dominance, 95% of the mass in the modern Universe: dark energy and dark matter (also called 'hidden mass') respectively provide about 68.3% and 26.8% of the total mass, while ordinary baryonic matter (stars, interstellar and intergalactic gas) contributes only about 4.9%. The nature of fields that form dark energy and dark matter particles remains unknown. As in the case of the inflationary paradigm, many theoretical models have been offered for dark energy and dark matter, but it is unclear which of them will be viable in the future and whether there is a true model among them that is realized in 'our Universe'.

The energy-dominating substance at present, dark energy, was discovered by analyzing the accelerating expansion of the Universe inferred from remote type-Ia supernova observations [8–10]. Later, its existence was confirmed by independent measurements of cosmic microwave background (CMB) fluctuations and other effects. Some scalar fields that remain from early epochs or the energy of quantum fluctuations of the vacuum could provide an explanation of dark energy. In this review, we focus on the cosmological epochs in which dark energy effects were negligible.

The problem of dark matter, which is the main topic of this review, has good chances to be solved in the nearest future. Dark matter particles, incident on Earth from space, can be registered by the existing and future detectors, or can be produced in collider experiments (at the Large Hadron Collider, first of all).

There is little doubt that dark matter does exist in the Universe. Dark matter explains the shape of the rotation curves of spiral galaxies, the dynamics of stars in elliptical galaxies, high gas temperatures in the halos of galaxies and galaxy clusters, and the motion of galaxies in small groups and in clusters. The presence of dark matter reconciles the results of primordial nucleosynthesis calculations with the observed elemental abundances by taking CMB anisotropy measurements into account. Only with dark matter is it possible to explain the stability of galactic discs and their spiral structure. The distribution of dark matter can be 'mapped' using strong and weak gravitational lensing observations — the appearance of multiple images of galaxies and their shape distortions [11], including in colliding galaxy clusters (the Bullet Cluster, etc.).

Although the nature of dark matter is unknown, the inflationary paradigm offers a natural model for generating density perturbations from which dark matter halos formed at later stages; ordinary baryonic matter cooled and streamed toward the centers of these halos. This process led to the formation of galaxies, stars, planets, and ultimately life.

Reviews of possible particle candidates for dark matter and methods for searching for them can be found, e.g., in [1, 12].

Weakly interacting massive particles (WIMPs) are most frequently considered to be the likely dark matter candidates. They could have formed in the early Universe in a number suitable to explain the observed dark matter. Among these particles, the neutralino — the lightest supersymmetric particle — is very popular [13, 14]. Other candidates include sterile neutrinos [15, 16], axions [17], gravitinos [18, 19], superheavy particles [20–23], and primordial black holes (PBHs) [24, 25].

The discovery of the light Higgs boson with the mass $m_{\rm H} \simeq 125$ GeV [26–28] has strengthened the status of the neutralino as the dark matter particle. The existence of a light Higgs boson, heavy Grand Unification particles, and supergravity are contradictory in principle because radiation diagrams (loops) predict the mass of the light boson $\delta m_{\rm H}^2 \sim (\alpha/\pi)\,\Lambda^2$, where α is the coupling constant and $\Lambda \sim 10^{16}$ GeV is the Grand Unification scale. Supersymmetry elegantly solves this problem by providing compensation to radiation diagrams, and no simpler and more elegant solution is known in the theory. If the light Higgs boson with a mass $m_{\rm H} < 130$ GeV had not been discovered, the existence of supersymmetry would have been in doubt. The discovery of the light Higgs boson with the mass $m_{\rm H} < 130$ GeV involves supersymmetry as the simplest and most natural explanation for its small mass. Supersymmetry is assumed to be broken using so-called soft terms in the Lagrangian, which are described by at least five free parameters. The fixed mass of the Higgs boson imposes constraints on these parameters and those of the Grand Unification, as well as on the masses of supersymmetric scalar particles (sparticles). The supersymmetric particles and the lightest particle among them, the neutralino, have not been discovered so far in the ATLAS (A Tororidal LHC Apparatus) and CMS (Compact Muon Solenoid) experiments at LHC, possibly not because these particles are too heavy but due to the weakness of their interaction. Future measurements with increasing fluxes of these particles will likely uncover supersymmetric particles (see the discussion of Higgs particles and supersymmetry after the discovery of the Higgs boson in [29]).

The direct registration [30, 31] or production of dark matter particles in accelerator experiments can provide the most reliable information on their nature; however, indirect methods of searching for them (for example, using their annihilation products and other effects) should also be appreciated, for two reasons. First, there is no guarantee as yet that dark matter particles will be directly detected in the foreseeable future. Second, if dark matter particles are directly detected successfully, many 'applied' problems will arise regarding the role of these particles in astrophysics, the influence of these particles and their annihilation and decay products on the composition of cosmic rays, the state of interstellar matter in the past and now, and other astrophysical processes. This means that many questions that are currently being considered in connection with the indirect detection of dark matter particles will be treated at a new level (with the already known dark matter particles).

From the standpoint of indirect detection, searches for signals (first of all, photons) from dark matter particle annihilation seem to be the most promising. If dark matter particles can annihilate, the efficiency of this process is mainly determined by the dark matter density. The local annihilation rate is proportional to the square of the particle number density, and therefore the signal from dense clumps can be higher than from the diffusive dark matter component. For

example, dark halos of galaxies, which were formed from primordial density perturbations several billion years ago, can have a higher density than the average matter density in the Universe. At the time of writing this review, the most distant galaxy was discovered by the Hubble Space Telescope at the redshift $z \approx 11.9$ (without spectroscopic confirmation), which means that the Galaxy was formed when the age of the Universe was 380 mln years (after the Big Bang, or since the end of the inflation stage), when the reionization of the Universe had not yet completed. But even at earlier times, protogalaxies should have been formed — the 'building blocks' of galaxies, which are similar to present-day dwarf galaxies. The character of dark matter clustering, the mass and formation time of these 'blocks', and the efficiency of their merging and mass increase due to the accretion of external matter depend primarily on the density perturbation spectrum. According to the most reliable model, perturbations were generated at the inflation stage from quantum fluctuations. Recently, the fluctuation spectrum was measured with high accuracy by the WMAP (Wilkinson Microwave Anisotropy Probe) [32] mission and the Planck space observatory [33]. However, the telescopes from these space missions can measure the perturbation spectrum only on very large scales. According to the inflationary paradigm, the spectrum of primordial perturbations extends to much smaller scales, which are bounded from below by the cosmological horizon scale at the end of inflation (the mass of dark matter on this scale is about $\sim 10^{-17}$ g). This means that already before the formation of protogalaxies, clumps of dark matter with masses much smaller than the Solar mass could have been formed. These clumps are the first structures that emerged in the Universe. Small-scale clumps of dark matter and their role in astrophysics are considered in detail in this review. For brevity in what follows, we refer to these small-scale clumps of dark matter simply as clumps.

We can visualize a clump as a sufficiently loose 'cloud' of moving dark matter particles that are bound by gravitation forces but do not fall onto a common center because of their angular momenta. The clump has an almost spherical shape and is in a quasistationary state if tidal forces from other objects or density perturbations are absent. The slow evolution of the internal structure of clumps can be due to weak gravitational perturbations, the binary scattering of particles, or annihilations of particles. The slow accretion of dark matter particles onto clumps from the surrounding diffuse component tends mainly to increase the effective radius of the clumps. Rapid and strong restructuring of clumps can be due to gravitational impacts of interacting clumps or collisions with stars. In certain cases, a clump can capture another clump or, just the opposite, can be captured by a larger clump. The boundary between the slow accretion of dark matter particles and the process of gravitational capture of small clumps (coalescence of clumps with strongly different masses) is somewhat conventional, but can be described by the generalized Press–Schechter formalism [34].

We briefly discuss the terminology. In the English-language literature, dark matter clumps are usually referred to as 'clumps', 'DM objects' (dark-matter objects), 'halos', 'minihalos', or 'microhalos'. The last three terms stress that in many respects, clumps are diminished analogs of large dark matter halos in galaxies. Indeed, by neglecting gas-dynamic processes with baryons occurring in galaxies, the equations of gravitational dynamics and principal formation processes of small-scale clumps and galactic halos are basically the same and differ only by the characteristic scales and the form of the perturbation spectrum at these scales. At small scales, the spectrum flattens, leading to rapid aggregation of clumps — the formation of large-scale clumps, with the characteristic time of this clustering being of the order of the formation time of the internal density profile in the clumps. By contrast, during the hierarchical clustering on galactic scales, the objects with density profiles already formed coalesce more frequently.

The formation and evolution of small-scale clumps have been studied in many papers [35–51] (see [52] for a short review of some aspects of the clump problem as of 2009). In some papers (see, e.g., [53]), a phenomenological approach has been used, which postulates the presence of clumps in some fraction of dark matter with a certain density profile and other free parameters, but unrelated to the specific density perturbation spectrum.

The mass spectrum of clumps is bounded by some minimum mass $M_{\min}$ depending on the properties of dark matter particles and their interactions with cosmic plasma in the early Universe at the radiation-dominated stage [54]. The formation of clumps with minimal masses occurs not due to the coalescence of smaller-scale objects but from individual density fluctuations without significant internal inhomogeneities (substructures). Hence, clumps with minimal masses, as well as those emerging from the perturbation spectrum with a high peak, can be segregated into a separate class of clumps to which the analytic model in [55–57] can be applied.

The mass $M_{\min}$ is model dependent; the value of $M_{\min}$ for the neutralino in the Minimal Supersymmetric Standard Model (MSSM) can range from $10^{-11} M_{\odot}$ to $10^{-3} M_{\odot}$ [41, 42, 46, 58, 59]. The minimal clump mass (the mass spectrum cutoff) $M_{\min}$ is determined by collisional and collisionless decay processes (see, e.g., [41] and the references therein). Additionally, the mass spectrum cutoff can be affected by acoustic waves [60] during the kinetic decoupling of dark matter particles [61], as well as by perturbation modes with the horizon scale [62]. Calculations [46] showed that to flatten small-scale perturbations, friction between dark matter particles and cosmic plasma, similar to the Silk effect, is important. Uncertainties in estimates of the minimal clump mass are due to uncertainties in the neutralino models involving free parameters.

A clump wit a minimal mass $M \sim 10^{-6} M_{\odot}$, which is obtained for the most likely supersymmetry parameters for the primordial power-law perturbation spectrum with the exponent $n_s = 0.96$ derived from the CMB data, has the following characteristic parameters. The first dark matter objects, which in this case are formed at the redshift $z \sim 60$ (for 2σ-perturbations) with the mean density $\bar{\rho} = 2.6 \times 10^{-23}$ g cm^{-3}, have the virial radius $R = 8.6 \times 10^{-3}$ pc and the internal velocity dispersion $v = 71$ cm s^{-1}.

The evolution of clumps in general should be studied in the hierarchical framework, which takes coalescence and aggregation of clump into account. Tidal interactions play a fundamentally important role in these processes, because tidal forces destroy most clumps at the early stages of hierarchical structure formation [39]. Clumps that survive the early hierarchical stage are further destroyed by collisions with stars in galactic bulges, halos, and discs. In this review, we show that the collective gravitational field of the disc has a much stronger effect than the total contribution of individual nearby stars.

In the foreseeable future, there is hope to directly register gamma-ray fluxes from particle annihilations in clumps. It is virtually impossible to observe small-scale clumps (they collectively contribute to the diffuse gamma-ray background), but sufficiently large clumps can be observed, in principle, as individual sources: they can form bright spots in the X-ray and gamma-ray sky [63–65]. The contribution of clumps to the annihilation signal is characterized by the enhancement coefficient, or the boost factor, which is by definition equal to the ratio of the signal with account for dark matter clumping to that from diffusively distributed dark matter.

Theoretical studies of dark matter halo formation [55–57, 76] predict power-law internal density profiles $\rho_{\rm int}(r) \propto r^{-\beta}$ with $\beta \simeq 1.8-2.0$. The density profiles obtained in numerical simulations (Navarro–Frenk–White (NFW) profiles and Moore et al's profiles [77]) have a similar divergent central density with $\beta = 1$. A result close to the isothermal power-law profile with $\beta \simeq 2$ was obtained in numerical simulations of small-scale clumps [77]. In [51], it was found that if a clump results from hierarchical clustering, then its density profile coincides with the NFW one. If a clump is formed from an isolated density perturbation (including minimal-mass clumps), its density profile has a central core with $\beta \simeq 1.4$. This means that the singular profiles that have not experienced collisions have central profiles closer to those of Moore et al and Gurevich–Zybin [55–57].

The increase in the density $\rho_{\rm int}(r)$ in the clump center as $r \to 0$ is limited by the total (integral) clump mass and especially by the finite value of the annihilation signal:

$$Q_{\rm ann} \propto \int {\rm d}r\, r^2 \rho_{\rm int}^2(r)\,. \tag{1}$$

For density distributions with $\beta > 1.5$, the presence of the central core is physically necessary, i.e., the core must exist in a wide class of models. Most frequently, the core is postulated in the form $\rho_{\rm int}(r) = {\rm const}$ for $r < r_{\rm c}$. Different physical mechanisms can be responsible for the formation of the central part (core) of clumps during their formation and evolution. It cannot be ruled out that these mechanisms are different for clumps with different masses formed under different conditions. The structure of the clump core is possibly determined by small-scale density and velocity inhomogeneities inside the forming clump; this problem was studied for galaxies in the framework of the entropy theory [78, 79]. A theoretical estimate of the clump core radius can be obtained using the energy criterion: $x_{\rm c} \equiv R_{\rm c}/R \simeq \delta_{\rm eq}^3$, where $\delta_{\rm eq}$ is the density perturbation amplitude at the beginning of the matter-dominated cosmological stage [57]. In application to clumps with a minimal mass $\sim 10^{-6} M_\odot$ formed from 2σ-peaks ($\delta_{\rm eq} \simeq 0.017$) in the spectrum, this estimate yields $x_{\rm c} \simeq 1.8 \times 10^{-5}$. It cannot be ruled out either that the core size or, at least, the characteristic scale of the density profile change β is also determined by tidal forces [39]. There is an alternative core formation mechanism in models with 'metacold dark matter', in which the core appears due to the late decay of dark matter particles into light nonrelativistic particles with low phase density [80, 81].

The low spatial resolution of numerical simulations currently prevents the determination of the core radius. The only example pointing to the presence of a core with a radius $x_{\rm c} \simeq 10^{-2}$ was obtained in calculations in [77]. However, in the simulations in [82], the core was not resolved down to the relative radius $x_{\rm c} \simeq 10^{-3}$, to which the power-law density profile with $\beta = 1.5$ extends. New, dedicated high-resolution modeling is required to solve this problem.

In [40], the conclusion was made that almost all small-scale clumps in the Galaxy are destroyed by tidal interactions with stars and are transformed into 'ministreams' of dark matter. The properties of ministreams can be important for the direct detection of dark matter particles, because dark matter particles in the streams move anisotropically in different discrete directions. However, as shown in [83], cores of clumps (or clump remnants) generally survive in tidal interactions with galactic stars. Although the external layers of clumps are 'stripped off' and produce dark matter ministreams, their cores are shielded by the adiabatic invariant conservation and continue to produce the annihilation signal. Most of the annihilation signal power is generated in the central parts of the clumps, and therefore the total annihilation flux is weakly affected by the tidal destruction process [37, 43]. This statement is critically dependent on the unknown core radius: cores with smaller sizes are more stable, because dark matter particles there have higher orbital frequencies and, accordingly, higher values of the adiabatic parameter. The clump remnants form a low-mass 'tail' of the standard mass function for masses below $M_{\rm min}$.

In addition to the 'standard' clump formation scenario, hypothetical models have been proposed in which superdense clumps are formed at the radiation-dominated stage from entropy [84–87] and adiabatic [88] density perturbations, taking restrictions from primordial black holes into account. Entropy perturbations, for example, can be produced by loops of cosmic strings. Superdense clumps are interesting from the standpoint of annihilation of superheavy dark matter particles, because their small annihilation cross section can be compensated by the high density of the clumps. Therefore, ultra-high energy annihilation signals become possible. In this case, new effects can appear that determine the central density core formation in superdense clumps, such as Fermi degeneration of superheavy dark matter particles in the cores of such clumps. The superdense clumps can be registered by the tidal effects they produce on gravitational wave detectors. In this review, we consider the formation of superdense clumps in much detail, because this problem has not been analyzed sufficiently in the literature.

2. Small-scale spectrum of density perturbations

The presence of matter inhomogeneities at small scales in early epochs is a necessary condition for the formation of small-scale clumps. Galaxies and other structures form from density perturbations $\delta(\mathbf{x}, t) = \delta\rho/\bar{\rho} = (\rho(\mathbf{x}, t) - \bar{\rho})/\bar{\rho}$, which generally can be adiabatic perturbations, entropy perturbations, or a mixture of both. Adiabatic perturbations are also referred to as curvature perturbations because the local curvature in such a perturbation differs from the mean curvature of the Universe. Entropy perturbations represent another possible type of perturbation. These include dark matter perturbations on top of a homogeneous radiation background. The effect of entropy perturbations on the space curvature is typically insignificant, and they are usually called isocurvature perturbations. According to CMB observations, the statistical distribution of adiabatic perturbations is Gaussian with high accuracy, and the contribution of entropy perturbations to the total perturbation amplitude, if present, does not exceed a few percent.

We briefly discuss the perturbation statistics. The Fourier transform

$$\delta_{\mathbf{k}} = \int \delta(\mathbf{r})\, \exp\left(\mathrm{i}\mathbf{k}\mathbf{x}\right) \mathrm{d}^3 x \tag{2}$$

is characterized by a power spectrum $P(k)$,

$$\langle \delta^*_{\mathbf{k}} \delta_{\mathbf{k}'} \rangle = (2\pi)^3 P(k)\, \delta_{\mathrm{D}}^{(3)}(\mathbf{k} - \mathbf{k}')\,, \tag{3}$$

where * denotes complex conjugation, $\mathbf{k}$ is the wave vector, $\delta_{\mathrm{D}}^{(3)}(\mathbf{k} - \mathbf{k}')$ is Dirac's delta function, and the angular brackets mean ensemble averaging, i.e., averaging over a large number of spatial volumes. The power spectrum $P(t, k)$ at an arbitrary time instant t is related to the initial power spectrum $P_p(k)$ (at superhorizon scales) as $P(t, k) = P_p(k)\, T^2(k)\, D^2(t)$, where $T(k)$ is the transfer function and $D(t)$ is the linear growth factor (see, e.g., [89, 90]). For small-scale modes, we have $T(k) \simeq (k_{\mathrm{eq}}/k)^2$ for $k_{\mathrm{eq}}/k \ll 1$ with the logarithmic accuracy. The rms density perturbation $\sigma(R) = \langle \delta^2 \rangle$ on a scale R is expressed in terms of $P(k)$ as

$$\sigma(R) = \frac{1}{2\pi^2} \int_0^\infty k^2\, \mathrm{d}k\, P(k)\, W^2(k, R)\,, \tag{4}$$

where $W(k, R)$ is the Fourier transform of the window function [89].

The statistical properties of forming structures are considered using two basic approaches: (1) by counting the number of peaks with certain characteristics [89]; (2) in the framework of the Press–Schechter formalism and its generalizations (see [34, 91, 92]). The second approach deals with the fraction of the dark matter mass contained in objects with a given mass scale. A generalization of these two approaches, and in some sense their synthesis, the so-called *peak-patch picture*, was developed in [93].

2.1 Generation of adiabatic perturbations at the inflation stage

In the inflation theory, curvature perturbations are generated from quantum fluctuations of a scalar field. The amplitude of the latter, $|\delta\phi| = H(\phi)/2\pi$, is connected with the Hubble parameter $H(\phi) = \dot{a}/a$ during the inflation stage [2], where $a(t)$ is the scale factor of the Universe. The density perturbations at the horizon crossing time are given by

$$\delta_{\mathrm{h}} \sim M_{\mathrm{Pl}}^{-3} V^{3/2} \left(\frac{\mathrm{d}V}{\mathrm{d}\phi}\right)^{-1}, \tag{5}$$

where M_{Pl} is the Planck mass and $V(\phi)$ is the potential of the scalar field (inflaton) that is responsible for the inflation.

The simplest inflation models give a nearly flat perturbation power spectrum $P(k) \equiv \delta_k^2 \propto k^{n_{\mathrm{s}}}$ with $n_{\mathrm{s}} \simeq 1$. However, some tilt of the spectrum is usually predicted, which is fundamentally important for small-scale clump formation, because even a small tilt can significantly change the perturbation amplitudes on low mass scales. The difference between n_{s} and unity is expressed in terms of the slow-roll inflation parameters $\varepsilon = (V'/V)^2/(16\pi G)$ and $\eta = (V''/V)/(8\pi G)$, where G is the gravitational constant, as follows:

$$n_{\mathrm{s}} = 1 - 6\varepsilon + 2\eta\,. \tag{6}$$

In the R^2-model by Starobinsky, $n_{\mathrm{s}} \simeq 1 - 2/N$, where N is the number of e-foldings (increases in the scale factor by e times) since the beginning of the generation of these perturbations until the end of inflation. The value of n_{s} in the inflation model has not been precisely fixed yet; as well as the common normalization constant, n_{s} is determined from the CMB anisotropy measurements and the inhomogeneities of matter distribution in the Universe. Observations thus constrain possible inflation parameters [94].

Immediately after the end of inflation, the perturbations (on the scales considered here) have a size greatly exceeding the cosmological horizon, but as the horizon increases $\sim ct$, they enter under the horizon at some instant of time. To investigate perturbations with scales larger than the horizon size, it is necessary to solve the linearized Einstein equations [2]. Using them, it is possible to match the solutions (and the initial conditions) on subhorizon scales. The perturbations that are deep inside the horizon can be studied using the Newtonian equations (taking the potential of a homogeneous relativistic background into account), but setting the initial conditions does require solving the linearized Einstein equations. At the radiation-dominated stage, small adiabatic perturbations (those on the linear stage), $\delta \ll 1$, grow slowly on subhorizon scales, $\delta_k \propto \ln(t/t_i) + \mathrm{const}$, and after the transition to the dust-like stage, $t > t_{\mathrm{eq}}$, they start increasing rapidly as $\delta_k \propto t^{2/3}$.

2.2 Normalization of the perturbation spectrum from observational data

The normalization constant in perturbation spectra is frequently chosen from the requirement that the relative mass fluctuations on the scale $8h^{-1}$ Mpc correspond to the value $\sigma_8 \simeq 0.82$, which is directly obtained from galaxy and galaxy cluster counts. An alternative method of spectrum normalization, which is nonetheless consistent with the above, is based on referencing to CMB fluctuations, because they are closely related to dark matter density fluctuations.

According to the CMB anisotropy data, it is convenient to normalize the curvature perturbation spectrum [2] as

$$\mathcal{P}_{\mathcal{R}} = A_{\mathcal{R}} \left(\frac{k}{k_*}\right)^{n_{\mathrm{s}}-1}, \tag{7}$$

where $k_*/a_0 = 0.002$ Mpc^{-1}, a_0 is the present-day value of the scale factor, $A_{\mathcal{R}} = (2.46 \pm 0.09) \times 10^{-9}$, and $n_{\mathrm{s}} = 0.9608 \pm 0.0080$ according to the WMAP data [32] and $n_{\mathrm{s}} = 0.9608 \pm 0.0054$ according to the Planck data [33]. Here, the typical perturbation amplitude is $\Delta_{\mathcal{R}} \simeq 5 \times 10^{-5}$. With only low multipoles used in the CMB power spectrum, the WMAP data [32] correspond to the constant n_{s} with an accuracy $\mathrm{d}n_{\mathrm{s}}/\mathrm{d}\ln k = -0.019 \pm 0.025$, but taking higher multipoles into account shows a (presently statistically insignificant) tendency of decreasing n_{s} toward small scales, $\mathrm{d}n_{\mathrm{s}}/\mathrm{d}\ln k = -0.022^{+0.012}_{-0.011}$. The Planck data [94] also point to a statistically insignificant (at a level of 1.5σ) decrease in n_{s}, $\mathrm{d}n_{\mathrm{s}}/\mathrm{d}\ln k = -0.0134 \pm 0.0090$. If such a decrease actually takes place, small-scale clumps form with a smaller efficiency than for the constant $n_{\mathrm{s}} \approx 0.96$.

The rms amplitude of density perturbations normalized to the CMB data on the horizon scale at the radiation-dominated stage has the form [95]

$$\sigma_{\mathrm{h}}(M) \simeq 9.5 \times 10^{-5} \left(\frac{M}{10^{56}\ \mathrm{g}}\right)^{(1-n_{\mathrm{s}})/4}. \tag{8}$$

For $n_s < 1$, the mean amplitude of perturbations decreases with decreasing the mass. Nevertheless, clumps can be formed before galaxies due to the transfer function $T(k)$, which for not too small n_s leads to an rms perturbation increase with decreasing the mass. For estimates, it is useful to write the mean value of perturbations on scales $M \leqslant M_\odot$ at the time of transition to the dust-like stage t_{eq}:

$$\sigma_{eq}(M) \simeq 8.2 \times 10^{3.7(n_s-1)-3} \left(\frac{M}{M_\odot}\right)^{(1-n_s)/6} \times \left(1 - 0.06 \log \frac{M}{M_\odot}\right)^{3/2}. \quad (9)$$

It can be seen that for $n_s \approx 1$, the logarithmic term in the transfer function is very important.

It should be borne in mind that the use of the spectrum normalized to the CMB data assumes a huge extrapolation, by more than 15 orders of magnitude. Such an extrapolation is justified for inflation models that give power-law spectra in a wide range of scales. However, strictly speaking, the predictions of inflation models for small scales have not been confirmed by observations so far. Therefore, to a large extent, the shape of the spectrum remains a 'free parameter'.

If the existence of small-scale clumps is confirmed (for example, by observations of dark matter particle annihilation), the clump properties can allow determining the shape of the perturbation spectrum on small scales and studying the processes of perturbation generation at the inflation stage. For example, it will be possible to fix parameters in the Lagrangians of the specific field models.

2.3 Perturbation spectra with peaks

Although the perturbation spectrum is sufficiently well known on the scales of galaxies and galaxy clusters, a nonstandard form of the spectrum cannot be ruled out on small scales, deviating from the simple power-law dependence and possibly containing local maxima or narrow peaks. As we can see from (5), an increase in δ_h is possible if the inflation potential $V(\phi)$ has a flat part [24, 96], i.e., if $dV(\phi)/d\phi \to 0$ at some value of the scalar field ϕ. The increase in δ_h can occur inside a wide region or in several regions. The clumps are formed in a broad mass range if the primordial perturbation spectrum has a power-law shape or there is a broad maximum in the spectrum. On the other hand, if the flat part of the potential is local, the clumps are formed near the corresponding mass. We note that outside these regions, the spectrum can remain close to the Harrison–Zeldovich one (Fig. 1) and lead to the formation of galaxies and galaxy clusters in the standard way.

A peak at the minimal scale produces clumps with the highest dark matter density in the Universe. The discovery of such clumps could provide invaluable information on the inflation potential. The presence of peaks can also lead to a more effective formation of PBHs with narrow mass distribution [24, 97].

Inflation models with several scalar peaks represent another class of models producing spectra with peaks [98, 99]. Theoretical models of nonstandard spectra were discussed, in particular, in [100–102].

An interesting mechanism in which the generation and amplification of perturbations is possible, including the appearance of spectra with peaks, is provided by cosmological phase transitions, for example, the quantum chromodynamics (QCD) transition at a temperature $\sim 150-200$ MeV (the time instant $\sim 10^{-5}$ s) [35, 37]. During the QCD transition, the equation of state of matter becomes softer (the ratio $w = p/\rho$ decreases), and perturbations grow more efficiently. However, in the model with a standard ($m \sim 100$ GeV) neutralino, the peak corresponding to the QCD transition is somewhat flattened in the subsequent evolution due to free-streaming and the corresponding spectral cutoff [62].

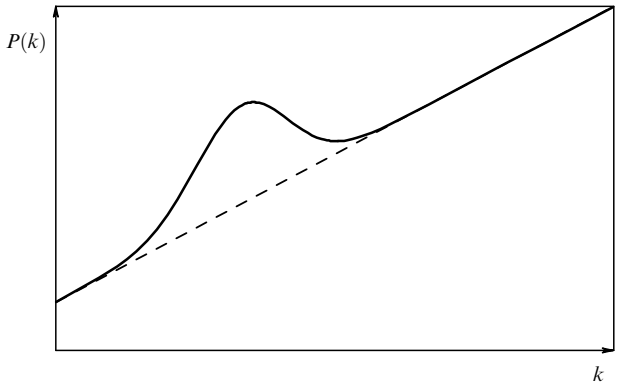

Figure 1. Schematic view of a local maximum in the primordial density perturbation spectrum.

2.4 Entropy perturbations

Entropy perturbations can be generated, in particular, in axion dark matter and lead to the formation of axion miniclusters [84, 85, 104].

Primordial black holes and various topological defects can also generate entropy perturbations. The nature of these perturbations can be illustrated as follows. We consider a point-like object with a mass M_c on the background of homogeneously distributed dark matter. We encircle this object by a sphere containing dark matter with a mass M. Then the effective value of perturbations within the volume of the sphere is $\delta = M_c/M$, where δ is obviously dependent on the sphere radius and decreases as the radius increases. For the motion of test particles at the spherical boundary, only the mean value of δ is important, and the specific density distribution of dark matter inside the sphere does not matter, according to the Kirchhoff theorem, if the density distribution is spherically symmetric. Perturbations produced by a seed mass evolve according to the 'secondary accretion' mechanism [76, 105, 106]. For example, PBHs or their clusters or cosmic string loops can serve as seed masses.

Strongly nonspherical perturbations, which have an entropy nature, can be generated by infinite cosmic strings or textures [107]. From the standpoint of the evolution of perturbations, the difference between entropy perturbations and adiabatic perturbations is in the absence of relatively large initial peculiar velocities of dark matter particles in the entropy perturbations.

2.5 Constraints from primordial black holes

The adiabatic perturbation spectrum is bounded by the effect of PBH formation in the early Universe, because, for a sufficiently large number of perturbations, an inadmissibly large number of PBHs would be created, in contradiction to observational constraints.

The possibility of a collapse of a small mass in general relativity (GR) and the creation of BPHs was first discovered in [108], and later PBH formation at the radiation-dominated stage was studied in many papers (see, e.g., [109–112]). In fact, photons and a mixture of relativistic particles collapse into PBHs. The formation of PBHs is also possible at the early dust-like stages [113]. PBH studies became especially relevant after the Hawking quantum evaporation was suggested, which can lead to high-energy gamma-ray emission at the final stages of evaporation. The observational absence of such sources strongly constrains the density perturbation spectrum at a mass scale corresponding to evaporating PBHs [114].

The threshold perturbation value $\delta_{\rm th} = 1/3$ leading to the formation of a PBH was found analytically in [110], and numerical simulations [111, 112] approximately confirmed this value, although they indicate a more complicated character of the gravitational collapse than was assumed in the simple model in [110]. Subsequent numerical experiments discovered the phenomenon of critical gravitational collapse, when the mass of the forming PBH is $M_{\rm BH} = AM_{\rm h}(\delta_{\rm h} - \delta_{\rm th})^{\gamma}$ [115, 116], where $A \sim 3$, $\gamma \simeq 0.36$, $\delta_{\rm th} \simeq 0.65-0.70$, and $M_{\rm h}$ is the mass of matter inside the horizon. The mass $M_{\rm BH}$ can be significantly smaller than $M_{\rm h}$; however, the PBH mass distribution is concentrated near $M_{\rm BH} \sim M_{\rm h}$ [117].

We set $\Delta_{\rm h} \equiv \langle \delta_{\rm h}^2 \rangle^{1/2}$. The fraction of the mass of radiation transformed into a PBH at the time instant $t_{\rm h}$ is expressed as [110]

$$\beta = \int_{\delta_{\rm th}}^{1} \frac{{\rm d}\delta_{\rm h}}{\sqrt{2\pi}\,\Delta_{\rm h}} \exp\left(-\frac{\delta_{\rm h}^2}{2\Delta_{\rm h}^2}\right) \simeq \frac{\Delta_{\rm h}}{\delta_{\rm th}\sqrt{2\pi}} \exp\left(-\frac{\delta_{\rm th}^2}{2\Delta_{\rm h}^2}\right), \tag{10}$$

and the present-day PBH density parameter is $\Omega_{\rm BH} \simeq \beta a(t_{\rm eq})/a(t_{\rm h})$. The above relations allow imposing bounds on $\Delta_{\rm h}$ from observational constraints on PBHs [118]. Constraints on the perturbation spectrum, in turn, impose bounds on the parameters of the clumps being formed (see Section 3.3).

3. Clump formation scenarios and models

There are two basic methods to study the process of formation and clustering and the internal structure of clumps: numerical modeling and the use of approximate analytic models. Analytic approaches, in historical sequence, were developed in [55, 56, 76, 106, 119], and the fundamentally important results in numerical modeling were obtained in [105, 120–123], where the formation of galaxies and large-scale structures was mainly studied. Numerical methods are permanently improving by increasing the spatial resolution and the time-scale range. It is expected that in the nearest future, numerical modeling will improve our knowledge of processes involving clumps. However, analytic calculations, which remain (and will remain in the future) the necessary link in formulating numerical problems, are important for a qualitative understanding of both physical processes and the results of numerical simulations.

In this section, we discuss some analytic approaches, in the order of increasing complexity and detail. For a more detailed discussion of the theory of structure formation in the Universe, without an accent on the small-scale clumps of interest here, we can recommend concise introductory courses [124, 125].

3.1 Spherical model of the evolution of perturbations

Let there be an isolated positive density perturbation $\delta(\mathbf{r})$, a protohalo. The clump is detached from the cosmological expansion at the time of transition of fluctuations to the nonlinear stage, growing to $\delta \geqslant 1$. Starting from that instant, the clump is compressed by its own gravity with a small correction due to tidal forces from nearby perturbations. In the first approximation, the protohalo can be considered a spherically symmetric object [34, 91]. Because of a fairly simple evolution, this approximation proves to be very useful — it suffices to understand basic processes and to obtain quantitative estimates.

We first write the very general equation for the evolution of a spherical layer with a radius r on scales much smaller than the horizon scale, $r \ll ct$. Let the mass of dark matter inside this layer be M. The contribution of the pressure of relativistic density components to the energy–momentum tensor can be taken into account in the Newtonian equations by substituting $\rho \to \rho + 3p/c^2$ [126, 127]. Then the evolution of the layer radius is described by the equation

$$\frac{{\rm d}^2 r}{{\rm d}t^2} = -\frac{G(M_{\rm BH} + M)}{r^2} - \frac{8\pi G\rho_{\rm r} r}{3} + \frac{8\pi G\rho_{\Lambda} r}{3}\,. \tag{11}$$

Equation (11) takes into account that $\varepsilon_{\rm r} + 3p_{\rm r} = 2\varepsilon_{\rm r}$ for radiation and $\varepsilon_{\Lambda} + 3p_{\Lambda} = -2\varepsilon_{\Lambda}$ for the cosmological constant, where $\varepsilon_{\rm r}$ and $p_{\rm r}$ are the energy density and pressure of radiation, and ε_{Λ} and p_{Λ} are the energy density and pressure of the cosmological constant. For generality, the possibility of the presence of a seed mass $M_{\rm BH}$, for example, the mass of a central black hole, is taken into account.

We first consider the scenario of clump formation at the matter-dominated stage. The small-scale perturbations we consider are formed at $z \gg 1$ ($t \ll t_{\Lambda}$), when the dark energy contribution to the total density of the Universe can be neglected. The initial conditions for (11) are set from the linear theory of perturbation growth, according to which dark matter perturbations grow as [2]

$$\delta(k, z) \simeq \frac{27}{2}\,\Phi_{\rm i}(k)\,\frac{1 + z_{\rm eq}}{1 + z}\,\ln\left(0.2k\eta_{\rm eq}\right), \tag{12}$$

where $\Phi_{\rm i}$ is the gravitational potential at the time the perturbation scale was much larger than the cosmological horizon. The distribution of $\Phi_{\rm i}$ can be obtained from (7). The power spectrum of the potential is described by a formula similar to Eqn (7), but with $A_{\Phi} = (4/9)\,A_{\mathcal{R}}$ [2]. Although it is possible to use $\delta \simeq \delta_{\rm eq}(t/t_{\rm eq})^{2/3}$ for estimates, expression (12) gives a more precise result because the transition to the dust-like stage with the equation of state $p = 0$ takes some time.

At $t \gg t_{\rm eq}$, the nonlinear stage of the evolution of perturbations is described by Eqn (11) without the last two terms in the right-hand side and with $M_{\rm BH} = 0$:

$$\frac{{\rm d}^2 r}{{\rm d}t^2} = -\frac{GM}{r^2}\,. \tag{13}$$

The initial expansion rate of the layer is smaller than that of the Hubble expansion due to the presence of peculiar velocities directed toward the center of the perturbation. These velocities can be specified using linear theory [128], according to which

$$\mathbf{v} = \frac{Ha}{4\pi}\,\nabla_x \int \frac{{\rm d}^3 x'\,\delta(\mathbf{x}')}{|\mathbf{x}' - \mathbf{x}|}\,. \tag{14}$$

in a flat universe. Then the initial expansion rate of a spherical layer at some instant of time $t_i \gg t_{eq}$ (but as long as $\delta(t_i) \ll 1$) takes the form $dr/dt(t_i) = H(t_i)(1 - \delta_i/3)$. The solution of Eqn (13) with the initial conditions as above can be parametrically expressed as [128]

$$r = r_s \cos^2\theta\,, \quad \theta + \frac{1}{2}\sin(2\theta) = \frac{2}{3}\left(\frac{5\delta_i}{3}\right)^{3/2}\frac{t - t_s}{t_i}\,, \qquad (15)$$

where

$$t_s = t_i\left[1 + \frac{3\pi}{4}\left(\frac{5\delta_i}{3}\right)^{-3/2}\right] \qquad (16)$$

is the time of the maximum expansion, θ is a parameter, and

$$r_s = r_i\left(\frac{3}{5\delta_i}\right) \qquad (17)$$

is the radius of the layer at the time of maximum expansion. If we assume that the Hubble flow is not perturbed (this is possible for entropy perturbations at an instant close to t_{eq}), i.e., the correction $\delta_i/3$ is absent in $dr/dt(t_i)$, then the substitution $5\delta_i/3 \to \delta_i$ should be made in Eqns (15)–(17) [76, p. 40].

At the instant $t_c = 2t_s$, the collapse of the layer to a point should formally occur, but in the simple model under consideration we assume that prior to this time, when the layer is compressed from the radius $r = r_s$ to $R \equiv r_s/2$, the spherical layer is virialized and the compression stops. The virialization, which represents the mixing and relaxation of different elements inside the layer, occurs due to radial oscillations, the presence of inhomogeneities in the compressing layer, and nonradial motions of matter. These processes take some time; therefore, the virialization is mainly completed by the time $t \simeq 3t_s$ [125].

If perturbations are also present on larger scales, a further increase in the protohalo mass occurs until its coalescence with other objects due to the segregation and virialization of new spherical layers. As a rule, large-scale perturbations decrease with time, which leads to collapses at later times. When the zero-energy boundary is reached, where $\delta_i = 0$, the object growth stops. After the virialization, the system becomes highly nonlinear, $\delta \gg 1$, but if the initial density perturbation can be formally extrapolated to the instant t_c using a linear law, we obtain the perturbation amplitude $\delta_c = \delta_i(t_c/t_i)^{2/3} = 3(12\pi)^{2/3}/20 \simeq 1.686$. The criterion of object formation with $\delta(t_c) = \delta_c$ is used in the Press–Schechter formalism; the collapse time t_c can be found from here. At this time, the density of the virialized object is $\kappa = 18\pi^2 \simeq 178$ times larger than the mean density of the universe, $\bar{\rho}_{int} = \kappa\bar{\rho}(z_c)$, and its radius is

$$R = \left(\frac{3M}{4\pi\bar{\rho}_{int}}\right)^{1/3}. \qquad (18)$$

The perturbation amplitude is expressed in units of the rms perturbations $\nu = \delta/\sigma$; typical objects are formed from perturbations with $\nu \sim 1-2$. Frequently, the virial radius is assumed to equal r_{200}, inside which the dark matter density is 200 times larger than the mean density of the universe.

Figure 2 shows the mean clump density ρ obtained using the above formalism as a function of the clump mass M for different primordial perturbation spectral exponents n_s; we formally assume an arbitrary clump mass M.

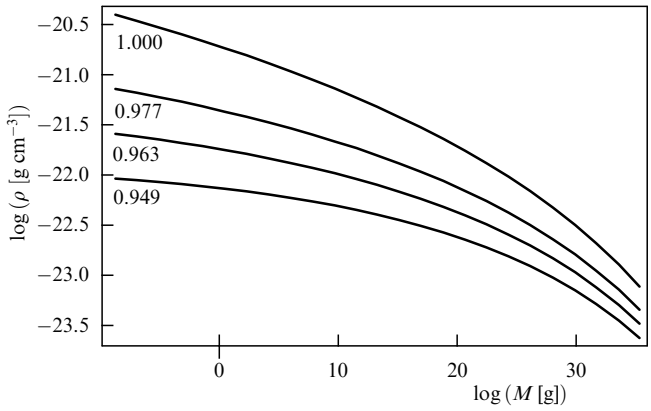

Figure 2. The mean clump density ρ as a function of its mass M for the spectral power-law exponents n_s (marking the curves), calculated in the framework of the simple spherical model at the dust-like stage.

3.2 Spherical model for entropy perturbations

The evolution of entropy perturbations, including at the radiation-dominated (RD) stage, is studied in detail in [85]. The main difference between entropy perturbations and adiabatic ones appears at the radiation-dominated stage of cosmological evolution. At this stage, adiabatic perturbations inside the horizon, as long as they are small, increase logarithmically, while small entropy perturbations are 'frozen' and, according to the Meszaros solution, increase only by a factor of 5/2 by the time t_{eq}. However, sufficiently large entropy perturbations can evolve and lead to the formation of clumps already at the RD stage.

Equation (11) for a spherical layer can be conveniently rewritten in the form [85, 129]

$$y(y+1)\frac{d^2b}{dy^2} + \left(1 + \frac{3}{2}y\right)\frac{db}{dy} + \frac{1}{2}\left(\frac{1+\delta_i}{b^2} - b\right) = 0\,, \qquad (19)$$

where $y = a(\eta)/a_{eq}$, $d\eta = dt/a(t)$ is the conformal time, $a_{eq} = a(\eta_{eq})$, and $\delta_i = \delta\rho_{DM}/\rho_{DM}$ is the initial relative dark matter density perturbation. Here, the perturbed region radius is parameterized as

$$r = a(\eta)\,b(\eta)\,\xi\,, \qquad (20)$$

where ξ is the initial comoving coordinate and the function $b(\eta)$ takes the expansion deceleration into account.

The cosmological expansion of the clumps stops at the time when $dr/dt = 0$, which is equivalent to the condition $db/dy = -b/y$ [85]. We let b_{max} and y_{max} denote b and y at the time of the expansion stopping. At that time, the cold dark matter density in the clump is

$$\rho_{max} = \rho_{eq}\,y_{max}^{-3}\,b_{max}^{-3}\,, \qquad (21)$$

and the clump radius is

$$R_{max} = \left(\frac{3M}{4\pi\rho_{max}}\right)^{1/3}. \qquad (22)$$

At a later time, the object is virialized when compressed by a factor of two in radius.

For entropy perturbations, the initial conditions are $\delta_i = \delta\rho_{DM}/\rho_{DM}$ and $db/dt = 0$ [85]. According to numerical

simulations [85], the clump density can be approximated with good accuracy as

$$\rho \simeq 140\delta_{\rm i}^3(\delta_{\rm i}+1)\,\rho_{\rm eq}\,. \tag{23}$$

For example, $\delta_{\rm i} \simeq 10^0 - 10^4$ for axion dark matter, and masses of emerging 'axion miniclusters' [84] fall within the range $\sim (10^{-13} - 10^{-1})\,M_\odot$. Possible observational appearances of the axion miniclusters in the galactic halo were discussed in [85, 104].

3.3 Spherical model for adiabatic perturbations at the radiation-dominated stage

In order to consider the evolution of adiabatic perturbations at the RD stage in a similar way, the initial conditions for (19) should be chosen in accordance with the linear solution for $\delta \ll 1$. On subhorizon scales [37],

$$\delta = \frac{3A_{\rm in}}{2}\left(\ln\frac{k\eta}{\sqrt{3}} + \gamma_{\rm E} - \frac{1}{2}\right), \tag{24}$$

where $\gamma_{\rm E} - 1/2 \approx 0.077$, $A_{\rm in} = \delta_{\rm h}/\phi$, $\phi \simeq 0.817$, and $\delta_{\rm h}$ is the radiation density perturbation at the horizon crossing time. For $k\eta \gg 1$ and $y \ll 1$, we have the relation [88]

$$k\eta = \frac{\pi}{2^{2/3}}\left(\frac{3}{2\pi}\right)^{1/6}\frac{yc}{G^{1/2}M^{1/3}\rho_{\rm eq}^{1/6}}\,. \tag{25}$$

The value of b in (20) can be expressed through δ as [129]

$$b = (1+\delta)^{-1/3}. \tag{26}$$

This relation means the transition from the Euler description, Eqn (24), to the Lagrange description, Eqn (19), of the perturbation evolution. For adiabatic perturbations, we can set $\delta_{\rm i} = 0$, but the initial velocity $\mathrm{d}b/\mathrm{d}t$ is nonzero and is determined by the linear stage of evolution.

It is convenient to connect analytic solution (24), obtained in the linear theory, to a numerical solution of nonlinear equation (19) at the time corresponding to the 'transitional' perturbation amplitude $\delta = 0.2$ (see [88]). At that time, we determine the initial velocity of the spherical layer from

$$\frac{\mathrm{d}b}{\mathrm{d}y} = -\frac{\delta_{\rm h}b^4}{2y\phi}\,. \tag{27}$$

The example of the evolution of $\delta = b^{-3} - 1$ is shown in Fig. 3.

The linear version, for $\delta \ll 1$, of the formalism described above (including the solution of the linear limit of Eqn (19) at the RD stage) is typically used to calculate the transition function and perturbation spectrum at the dust-like stage [90]. However, the clumps can already be formed at the RD stage from sufficiently large perturbations.

The characteristic clump densities ρ (cross section of the surface in Fig. 4) are shown in Fig. 5. We see that at small $\delta_{\rm h}$, the curves converge to $\rho \sim \rho_{\rm eq} \sim 10^{-19}$ g cm^{-3}. This corresponds to solution (15), according to which the perturbation evolution at the dust-like stage does not depend on mass and is determined by the initial perturbation amplitude (at $t = t_{\rm eq}$).

To produce superdense clumps, excessive small-scale perturbations are needed, e.g., in the form of peaks. It is clear from (8) that perturbations with a simple power-law

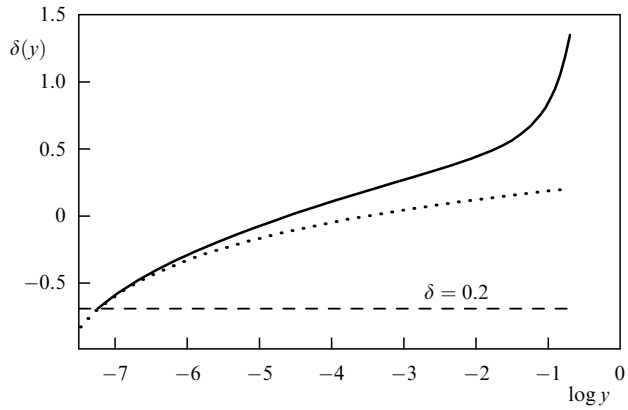

Figure 3. Example of the evolution of a cold dark matter density perturbation δ for $\delta_{\rm h} = 0.04$, $M = 0.1M_\odot$, $\Omega_{\rm m} = 0.3$. Up to the point ($y_{\rm i} = 4\times10^{-6}$, $\delta_{\rm i} = 0.2$), the solid curve is obtained using formula (24), and for $y > y_{\rm i}$, from a numerical solution of Eqn (19). The clump decouples from the cosmological expansion at the radiation-dominated stage at $y = a/a_{\rm eq} \simeq 0.5$. The dashed curve shows the evolution of δ according to the linear theory, Eqn (24).

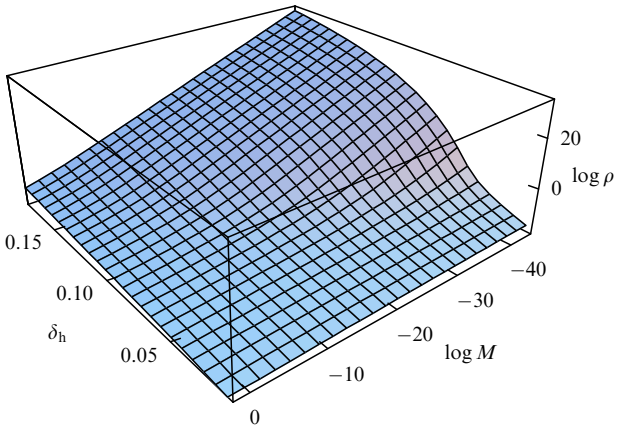

Figure 4. Mean clump density ρ [g cm^3] as a function of the clump mass M (in units of $M_\odot$) and the radiation density perturbation $\delta_{\rm h}$ on the horizon scale.

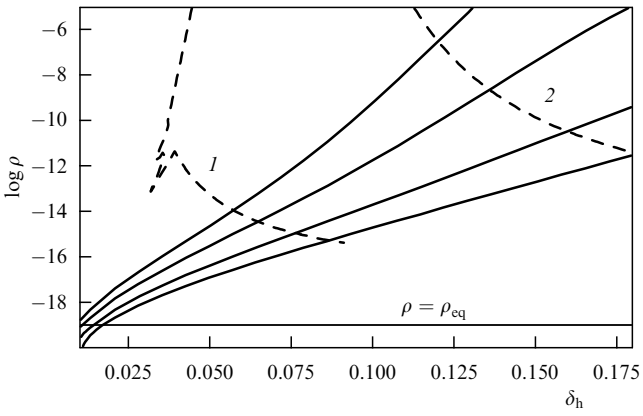

Figure 5. Mean clump density ρ [g cm^{-3}] as a function of the radiation density perturbation amplitude $\delta_{\rm k}$ on the horizon scale. The solid curves (from top down) respectively correspond to the clump masses $M = 10^{-11}M_\odot$, $10^{-6}M_\odot$, $10^{-1}M_\odot$, $10^2M_\odot$. The dashed curves correspond to the clump density limits from primordial black hole overproduction for the formation thresholds $\delta_{\rm th} = 1/3$ and $\delta_{\rm th} = 0.7$ (curves *1* and *2* respectively).

spectrum and $n_s < 1$ are too small to form clumps at the RD stage. We note that superdense clumps formed from the spectrum maximum do not aggregate into hierarchical structures for a long time and are therefore almost unaffected by tidal forces, and their mass function is concentrated around some mass corresponding to the spectral maximum.

The clump formation scenario from adiabatic perturbations at the RD stage is constrained by the PBH formation effect. In the model of 'neutralino stars' with masses close to $\sim 0.1 M_\odot$, this constraint was obtained in [88]. Following, e.g., [24, 96, 98], we assume that there is a sufficiently high maximum on some comoving scale $\xi = r/a(t)$ in the cosmological perturbation spectrum. Fluctuations with $\delta_h > \delta_{th} \sim 1/3$ collapse to form PBHs, and smaller perturbations turn into clumps. The mass fraction of such dark matter clumps is expressed, as in (10), by the integral [103]

$$\beta_{cl} = \int_0^{\delta_{th}} \frac{d\delta_h}{\sqrt{2\pi}\,\Delta_h} \exp\left(-\frac{\delta_h^2}{2\Delta_h^2}\right). \tag{28}$$

As noted in Section 2.5, to avoid overproduction of PBHs, the condition $\Delta_h \ll \delta_{th}$ should be satisfied; therefore, $\beta_{cl} \approx 1/2$. That is, half of the dark matter is in the region of positive perturbations. However, not every perturbation from this region can evolve into clumps. In Section 3.4, we precisely determine the fraction of superdense dark matter clumps, taking the nonsphericity of perturbations into account.

The relation of the PBH mass, which is equal to the total dark matter mass under the horizon M_h by an order of magnitude, to the dark matter mass M in fluctuations of the same comoving scale at the horizon crossing time $t_h \simeq GM_h/c^3$ has the form [88]

$$M_h = \frac{1}{2^{2/3}}\left(\frac{3}{2\pi}\right)^{1/6} \frac{M^{2/3}c}{G^{1/2}\rho_{eq}^{1/6}} \simeq \tag{29}$$

$$\simeq 1.5\times 10^5 \left(\frac{M}{0.1M_\odot}\right)^{2/3} M_\odot . \tag{30}$$

Using (10) and (29), we can express the cosmological PBH density parameter Ω_{BH} at the present time through dark matter perturbations. Thus, PBHs put bounds on the clump parameters shown in Fig. 5. The cusp on curve *1* corresponds to PBHs that are evaporating at the present time via Hawking radiation.

We recall that PBH formation occurs on the tail of the Gaussian distribution of fluctuations, and most of the clumps are formed from fluctuations with the rms amplitude $\delta \sim \Delta_h$. Therefore, we repeat, not every fluctuation that produced a clump could collapse into a PBH at the instant t_h. In other words, due to the high PBH formation threshold, a significant fraction of fluctuations did not collapse into PBHs and continued to evolve (Fig. 6).

Because the clumps and PBHs originate from the same perturbation spectrum, the mass and radius clump distributions can, in theory, restore the form of the perturbation spectrum and the PBH mass functions can be obtained using a formalism similar to the Press–Schechter theory [114]. Such a calculation will be possible once clumps are discovered.

3.4 Nonspherical models

The form of primordial perturbations is typically not spherically symmetric, and the asymmetry can increase with time. Therefore, in studying clump formation, it is necessary to go beyond simple spherical models.

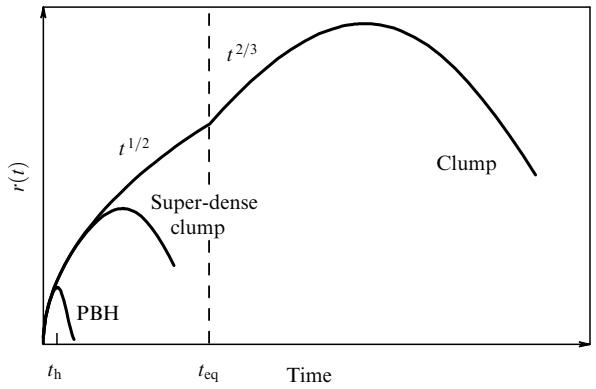

Figure 6. Different evolutions of a density perturbation as a function of its amplitude. Perturbations above the threshold collapse to form PBHs immediately after the horizon crossing time t_h. If the perturbation amplitude is insufficient to form a PBH, but the perturbed region becomes self-gravitating at the radiation-dominated stage at $t < t_{eq}$, a superdense clump is formed. Clumps with lower densities are produced at $t > t_{eq}$.

The simplest generalization of the spherical model is the model of a homogeneous ellipsoid (see its detailed description, e.g., in [128, 130]). Although the homogeneous ellipsoid approximation does not take the density increase toward the center and other inhomogeneities into account, it is useful because it allows taking the evolution of nonsphericity into account in the framework of a simple analytic model, as well as considering the interaction of external tidal forces with the quadrupole moment of the perturbation. This interaction increases the angular momenta of protogalaxies at their formation stage [130]. The evolution of a self-gravitating homogeneous ellipsoid preserves the ellipsoidal form and volume homogeneity of the object, although both the density and the ratio of different ellipsoid axes can change. The initial compression velocities along different ellipsoid axes can be inferred from the peculiar velocities.

The use of the homogeneous ellipsoid model in [131] to investigate the problem of superdense clump formation at the radiation-dominated stage (a generalization of the model described in Section 3.3) allowed finding the growth factor of perturbation nonsphericity $s(t)$. We can assume that the boundary of maximum admissible nonsphericity satisfies the condition $s_f/b_f < 1$, and at higher nonsphericities, the clump disintegrates and is not virialized. If the growth factor is known, the clump formation condition can be expressed through the initial data nonsphericity: $s_i/b_i < (b_f/b_i)(s_i/s_f)$. The shape distribution of Gaussian perturbations can be calculated using the results in [132] or [89, 133]. The closer the perturbation shape is to the spherical one, the more rarely such a perturbation occurs. As a result, for the least dense clumps forming at $t \leqslant t_{eq}$, the number of clumps decreases by an order of magnitude due to the initial perturbation nonsphericity. For dense clumps that are formed earlier, at $t \leqslant t_{eq}$, this decrease can be as high as 4–5 orders of magnitude.

For objects that are formed at the dust-like stage, the model of ellipsoidal collapse allows precisely determining the halo formation criterion in the Press–Schechter formalism. In [133], corrections to the spherical model were obtained that improved the Press–Schechter mass function, and the modified mass function is widely used in theoretical calculations of galaxy and galaxy cluster formation.

Another method to go beyond the spherical approximation is to use the Lagrangian method to describe the perturbation growth. The Zeldovich approximation [134, 135] provides a remarkable example of such an approach. It allows studying different aspects of three-dimensional compression of dark matter. The Zeldovich approximation was generalized to the evolution at the RD stage in [129], where corrections to the linear theory were obtained. Simpler Lagrangian approaches are also used, in which the dark matter density growth due to the velocity boost is studied, and gravitational forces are neglected over most of the time of evolution. This method is used, for example, to study the evolution of clumps from strongly nonspherical topological defects [107, 136].

3.5 Clumps around topological defects

Topological defects (infinite strings, cosmic string loops, and textures) are considered as clump seeds in [107]. Moving infinite strings or loops produce a velocity boost for dark matter particles, which leads to the density increase along the trajectories of motion of the topological defects.

We focus on the scenario of clump formation around cosmic string loops, which serve as seeds for entropy perturbations, as described in Section 2.4. These clumps are formed at the RD stage, and their density can greatly exceed $\rho_{\rm eq}$. Linear topological defects — cosmic strings — can be formed during the early cosmological phase transitions (see reviews [137, 138]). In addition to the formation of infinite strings, closed string loops can be formed due to string self-crossing [139, 140]. Only low-velocity loops can form very dense clumps around them [85]. We require the shift of a string, starting from its formation time $t_{\rm i}$ to its destruction time $t_{\rm d}$, to be small in comparison with the loop radius $l/(2\pi)$. For the Maxwell loop velocity distribution, the string formation probability satisfying this condition is estimated to be $P_{\rm lv} \sim 10^{-7}$ [141]. However, the requirement of a small shift compared with the loop radius is redundant. Even if it is violated, a clump can be formed, although with a lower mean density [136].

Clump formation around loops at the RD stage was studied in [85] using Eqn (19). In the approach in [85], the maximum clump density is restricted by the adiabatic expansion of clumps that have already formed due to the evaporation of loops. In [141], this density restriction was modified in the case where loop decay occurs before clump virialization. The clump density can then be $\rho_{\rm cl} \gg 140\rho_{\rm eq}$.

The loop length distribution is obtained in the form [142]

$$\mathrm{d}n_{\rm loop} = \frac{N\,\mathrm{d}l}{c^{3/2}t^{3/2}l^{5/2}} \tag{31}$$

with $N \sim 2$. This distribution is translated into the clump distribution, which can be used to calculate dark matter annihilation signals [141] or to study gas ionization [136].

4. Internal structure of clumps

Besides the typical characteristics of clumps, their internal structure is very important, especially in the central core, where dark matter particle annihilation can occur most efficiently due to the high density. The model of galaxies with a power-law increasing central density profile was elaborated in [105, 106] and [76] in the framework of the 'secondary accretion model'. This model assumes that dark matter 'accretes' onto an initially existing central object, a 'seed mass' $M_{\rm c}$, which can be a compact clump or a black hole. This central object produces a perturbation $\delta = M_{\rm c}/M$, as shown in Section 2.4. In an approximate approach, the evolution of caustics that arise during gravitational contraction and the crossing of dark matter layers was also discussed in [76]. Later, the model of a dissipationless gravitational singularity was proposed in [55–57], which also produces a power-law density profile, and the calculations in [55–57] were performed by a powerful method of adiabatic invariants, enabling the study of evolution in the nonlinear regime. We note the fundamentally important advantage of the model developed in [55–57] over the secondary accretion models. As shown in [55–57], under the action of self-gravity, a density perturbation with an initially smooth profile takes an approximately power-law form without any seed mass:

$$\rho_{\rm int}(r) = \begin{cases} \rho_{\rm c}\,, & r < R_{\rm c}\,, \\ \rho_{\rm c}\left(\dfrac{r}{R_{\rm c}}\right)^{-\beta}, & R_{\rm c} < r < R\,, \\ 0\,, & r > R\,, \end{cases} \tag{32}$$

where $\rho_{\rm c}$ is the clump central density, $R_{\rm c}$ is the radius at which the density growth stops, R is the virial radius or the radius of the last layer that was singled out from the cosmological expansion and stabilized after the nonlinear compression stage, and $\beta = 1.7-1.9$.

Because Gaussian primordial density perturbations yield smooth initial conditions, the model in [55–57] describes the physical processes more realistically. However, so far we have considered the formation of an individual object from an isolated density perturbation. Coalescences of objects during hierarchical clustering can appreciably modify the density profile (see Section 4.9).

The internal structure of the clumps has been studied in many papers, but this problem remains unsolved in one important aspect: which physical process stops the density increase during the clump formation and at what radius? The region bounded by a circle of this radius is called the clump core. The core radius is very important for studying the annihilation signals, and we discuss some processes that are possibly responsible for the central core formation in Sections 4.1–4.9.

4.1 Physics of violent relaxation and virialization

Virialization is the mixing of dark matter streams until the entire halo reaches an equilibrium inside some radius, the so-called virial radius. Outside this radius, the mixing is not completed, and new layers of dark matter, which decouple from the cosmological expansion, continue to fall toward the center. The virialization occurs due to radial oscillations, the presence of large inhomogeneities, and the nonspherical motions of matter. According to Lynden-Bell [143], these processes are called 'violent relaxation'. The virialization leads to an energy redistribution between different density clumps and between the kinetic and potential energy.

Inasmuch as dark matter particles scatter mainly on large clumps and inhomogeneities of matter during 'violent relaxation', a nearly Maxwell velocity (not energy) distribution is established. The virialization also leads to the tidal destruction of large clumps and their mixing and results in the formation of a sufficiently smooth density profile. The total energy $E = T + U$ in some dark matter layer is the sum of the kinetic and potential energies. At the linear stage, $|E| \ll |T| \approx |U|$, but after the virialization, $E \approx -T \approx U/2$.

This state is reached when the layer radius decreases by a factor of two, $R = R_{\max}/2$, after the expansion stop at the time t_s (because the potential energy of the layer $U \approx GM/R$) and, accordingly, the mean density of the stabilized object is $\rho = 8\rho(t_s)$.

In the approach considered here, we reliably assume that most of the mass of dark matter is concentrated in the outer layers, which have just been virialized; therefore, the contribution of the internal mass to the mean density is not very significant.

Initially, the 'violent relaxation' concept by Lynden-Bell was based on radial oscillations of an object, which are accompanied by rapid variations of the gravitational potential. As the picture of the hierarchical clustering of large-scale structures emerged, it became clear that nonradial motions during the aggregation of objects, which represent large inhomogeneities, also produce a variable gravitational potential leading to violent relaxation in the forming halo [144]. Hierarchical clustering and the relaxation related to it produce, besides virialization, a universal density profile, for example, an NFW one. According to the results of calculations in [145], an instability in the phase space, phase mixing, and a moderate 'violent relaxation' should be present for the relaxation to begin.

Nonradial motions of dark matter particles in the halo play an important role in the relaxation process because these motions lead to dark matter mixing inside each dark matter layer with energy redistribution until the virial equilibrium is reached. Nonradial motions occur due to coalescences of different subhalos, the initial inhomogeneities, and tidal forces from the external mass distribution. Adiabatic capture in the multi-stream regime [55–57] is an important mechanism of energy redistribution between the layers. Although this mechanism operates only in the radial direction, it also leads to the universal density profile $\rho \propto r^{-1.8}$ in isolated halos.

In a real situation, even in the case of an isolated object formed from a peak in the perturbation spectrum at some scale k, both the inhomogeneity and nonsphericity appear on scales $\Delta k \sim k$. At the beginning of the nonlinear stage, the proto-object consists of several (for example, N) large inhomogeneities with masses $M_s \sim M/N$. The two-body relaxation time in this 'cluster' is

$$t_r \simeq \frac{N t_{\rm dyn}}{10 \ln N} \tag{33}$$

and does not differ significantly from the dynamical time $t_{\rm dyn}$. Thus, the object experiences a ''violent relaxation'' accompanied by energy redistribution due to binary scattering of large inhomogeneities, which ultimately leads to virialization.

The virialization of early formed clumps can occur even at the RD stage. Does this process differ from the ordinary violent relaxation at the matter-dominated stage? Disintegration and dissociation of very irregular halos can be a new feature of the nonlinear evolution of clumps at the RD stage. Indeed, if the protohalo is sufficiently elongated, the mass of radiation inside the minimal sphere encircling the protohalo exceeds that of dark matter, and the object self-gravity cannot hold its parts together. The protohalo decays and its pieces fly apart due to cosmological expansion. To find the nonsphericity above which such an evolution is possible, numerical simulations of clump formation at the RD stage are required.

4.2 Secondary accretion, self-similar solutions, and 'ultra-compact minihalos'

In the spirit of secondary accretion models [76, 105, 106], we assume that at the radiation-dominated stage, there is a seed mass M_c, and dark matter is distributed homogeneously in its nearby surroundings prior to the dust-like stage (the effect of nearby perturbations is to be discussed below). At $t \ll t_{\rm eq}$ for mass scales $M \gg M_c$, a dark matter perturbation $\delta_i = M_c/M$ does not evolve. Indeed, according to the Meszaros solution, $\delta = \delta_i(1 + 3x/2)$, where $x = a/a_{\rm eq}$ [128]. This solution can easily be found from Eqn (19) in the linear approximation. Later, at $t > t_{\rm eq}$, we can use solution (15) with the substitution $5\delta_i/3 \to \delta_i$, as noted in Section 3.1. The object formation threshold in the spherical model in this case is $\delta(t) = \tilde{\delta}_c = (3\pi/2)^{2/3} \approx 2.81$. Then the virialized object mass as a function of the redshift takes the form

$$M(z) = \frac{3}{2}\left(\frac{2}{3\pi}\right)^{2/3} \frac{1+z_{\rm eq}}{1+z}\, M_c \approx 1.7 \times 10^3 \left(\frac{M_c}{10^2 M_\odot}\right)\left(\frac{1+z}{100}\right)^{-1} M_\odot\,, \tag{34}$$

with $(3/2)[2/(3\pi)]^{2/3} \approx 0.53$, and the radius $r_c = r_s/2$ of the layer that was virialized is

$$r_c = \frac{1}{3}\left(\frac{3}{4\pi}\right)^{1/3} \frac{M^{4/3}}{\rho_{\rm eq}^{1/3} M_c} \simeq 3.2\left(\frac{M_c}{10^2 M_\odot}\right)^{1/3}\left(\frac{1+z}{100}\right)^{-4/3} [\mathrm{pc}]\,. \tag{35}$$

Using halo's mass–radius relation (35), we find the density profile

$$\rho(r) = \frac{1}{4\pi r_c^2}\left.\frac{{\rm d}M(r_c)}{{\rm d}r_c}\right|_{r_c=r} \simeq 3\times 10^{-21}\left(\frac{r}{1\ \mathrm{pc}}\right)^{-9/4}\left(\frac{M_c}{10^2 M_\odot}\right)^{3/4} [\mathrm{g\ cm^{-3}}]. \tag{36}$$

In the case of a noncompact central mass, for example, an extended PBH cluster, the density profile differs from $\rho \propto r^{-9/4}$. Adding new layers at the periphery does not strongly affect the already formed internal density profile due to a relatively high central density, which is confirmed by analytic estimates and numerical simulations [145]. The constant flux of a new mass onto the system shifts its state by 10% from virial equilibriums, i.e., the constant in the energy relation $2T/|U| = \mathrm{const}$ differs from unity [145].

The total mass of the induced halo increases with time, as more and more remote layers decouple from the cosmological expansion and are virialized around the seed mass. The induced halo growth stops when ordinary dark matter fluctuations (those originating from inflation perturbations) with mass M equal to the induced halo mass enter the nonlinear stage. The growth law $\propto t^{2/3}$ is the same for usual perturbations and those induced by a seed mass; therefore, the halo growth stopping condition is simply [145, 147]

$$\nu\sigma_{\rm eq}(M) = \frac{9}{10}\,\frac{M_c}{M}\,, \tag{37}$$

where ν is the density perturbation amplitude in units of the rms fluctuation value. The right-hand side of (37) is the fluctuation amplitude due to the mass M_c taking the two

correction factors described above into account. The left-hand side describes usual Gaussian fluctuations taken at the time t_{eq}. The numerical solution of Eqn (37) yields the ultimate mass of the induced halo, which for $M_c \sim (10^0 - 10^4)\, M_\odot$ is $M \sim 10^2 M_c$. In [103, 148–152], it was assumed that the growth of clumps stops at $z \sim 10-30$, when large-scale dark matter structures start forming intensively. A more accurate quantitative criterion of the cessation of growth is given by Eqn (36).

Notably, clumps can be formed by this mechanism around PBHs [146–148, 150], and the idea that PBHs can be seeds of more extended objects was first put forward in [153]. Dark matter annihilation in mini-peaks around black holes (of stellar origin or resulting from collapses of gas clouds in the first halos) was considered in [154]. Of special interest is the case where dark matter particles annihilate to produce a narrow line. This line is broadened due to relativistic effects near the black hole horizon, which offers an observational signature of dark matter annihilation around black holes [155]. The character of line broadening must depend on the dark matter density distribution at distances up to several gravitational radii from the black hole; however, no detailed calculations of this dependence have yet been performed.

In [76, 156], self-similar accretion regimes were found in the framework of the secondary accretion model, in which collapses of new spherical layers maintain a power-law density profile. However, for this to be possible, the initially singular density profile $\delta\rho_i \propto r^{-\varepsilon}$ with an infinite central density in the protohalo is required. The rate of the virial radius r_s increase then depends on the parameter ε, and characteristics of all halos in the self-similar solutions are expressed in terms of the variable $X = r/r_s$. Initially, the density perturbation is not singular; therefore, the central density can be lower than in self-similar solutions, and the completion of the accretion of fresh outer layers can violate the self-similar regime and flatten the density profile $\rho \propto r^{-3}$ in the halo periphery [145]. The formation of singular profiles from the initially smooth perturbations cannot be explained by the secondary accretion model and self-similar solutions. This problem was solved by Gurevich and Zybin [55–57].

Recently, some papers [103, 148–152, 154, 157–163] have discussed so-called ultra-compact mini-halos — clumps formed at the very early stages (at the beginning of the dust-like stage) from large density perturbations of different natures: spectral peaks or perturbations enhanced in phase transitions in the early Universe. The important idea formulated in [158, 159] is that the annihilation limits, in principle, allow constraining the primordial perturbation spectrum from which clumps are formed. A sufficiently strong annihilation signal would violate the gamma-ray background limits; hydrogen recombination retardation or a delay in the reionization in the Universe may also have taken place, which would leave imprints in the CMB spectrum. However, to obtain reliable constraints, it is necessary to know, in addition to dark matter particle properties, the internal structure of dark matter clumps, especially in the core.

If the clump was formed around a superdense clump, which in turn originated at the RD stage, a modification of the object density at the center would be required. To calculate the mean density of the central superdense clump, the formalism in [85, 88, 164], described in Section 3.3, is required. In superdense clumps, due to their individuality, the Gurevich–Zybin profile is likely to arise. The issue of superdense clump cores also remains open.

4.3 Nondissipative gravitational singularity (Gurevich–Zybin theory)

The dissipationless gravitational singularity is reviewed in detail in [57], and therefore this model, in spite of its importance, is discussed here only very briefly.

We consider some individual perturbation with a smooth density profile. Given that adiabatic perturbations are characterized by one scalar function whose derivatives give peculiar velocities (perturbations relative to the homogeneous Hubble flow), the problem was reduced in [55–57] to the collapse of a density perturbation at rest by introducing some effective density. By assuming a small deviation from spherical symmetry, a nonlinear growth law for density perturbations was found. The central density of the perturbation increases and becomes formally infinite at some instant, after which dark matter flow crossing emerges.

The novelty of the approach in [55–57] and the key factor of its success are the use of the adiabatic invariant method in the multi-stream evolution regime. The conservation of adiabatic invariants allowed the authors to find the dark matter particle distribution function in forming halos. It was shown, as a result, that in the nonlinear regime with $\delta \geqslant 1$, a multi-stream instability arises, and power-law density profile (32) is formed in the clump. After the cessation of cosmological expansion, the forming clump starts compressing to the radius $R = \lambda R_{max}$, where λ is a nonlinear compression factor. It is usually assumed [165] that after the cosmological expansion stops, the clump is virialized by compressing by a factor of two in radius, i.e., $\lambda = 0.5$. But according to the gravitational instability theory, $\lambda \simeq 0.3$ in the multi-stream region [166]. In [55–57], the clump core radius is estimated to be $R_c/R \simeq \delta_{eq}^3 \ll 1$ from the analysis of the velocity field in the decaying perturbation mode.

As mentioned in Section 4.2, an important advantage of the Gurevich–Zybin theory is that it explains the power-law density halo formation from initially smooth perturbations without the central seed mass that is a prerequisite in the secondary accretion models. What is not fully accounted for by this theory so far is the effect of hierarchical clustering of halos with different scales, which is now considered to be the main factor for the universal density profile formation. As a whole, the theory in [55–57] is in good agreement with observations and numerical results at intermediate scales. However, in the central parts of galactic halos, the power-law exponent β in profile (32), apparently cannot take values $\beta = 1.7-1.9$, as pointed out in [55–57], because microlensing observations and measurements of star dynamics suggest that $\beta \leqslant 1.5$ near the galactic center [167]. By contrast, in the cores of minimal-mass clumps and cores formed in spectral peak models, the values $\beta = 1.7-1.9$ are quite possible, because these clumps are formed from decoupled smooth density perturbations.

4.4 Constraints on the core radius from the Liouville theorem

The constraint for the maximum density of an object, following from the constraint for the phase density $F_L(p, q, t)$, which is conserved according to the Liouville theorem, was considered in [168] in application to hypothetical heavy leptons. For the Liouville theorem to be applied, only the Hamiltonian character of the system is required. The Liouville theorem remains valid when multi-stream flows emerge (the formation of caustics), because the distribution function remains single-valued in the phase space.

If particle annihilation and other effects violating the Liouville theorem conditions are unimportant, $F_L(p, q, t) =$ const along the particle trajectories. Unfortunately, R_c can only be restricted but not obtained from the Liouville theorem applied only to the initial and final clump states. This is related to entropy generation in the intermediate processes, which is taken into account in the entropy theory [79]. In other words, the phase volume is rendered very dispersive by the process of nonlinear dark matter mixing (see Fig. 8.3 in [2]).

For a comparison with observations in astrophysics, it is convenient to use the quantity $Q = \rho/\sigma^{3/2}$ as a distribution function, where $\sigma = \langle v_{||}^2 \rangle = \langle v^2 \rangle/3$ is the one-dimensional velocity dispersion. Numerical modeling shows that over several orders of magnitude in radius, $Q \propto r^{-1.875}$ [169]. For theoretical estimates, we can use $f_c = \rho_c/v^3$ as the distribution function in the clump core, where ρ_c is the core density and v is the characteristic core particle velocity. For nearly isothermal profile $\rho(r) \propto r^{-2}$, the velocity v is of the order of the virial velocity in the entire clump.

We find the constraint on R_c from the Liouville theorem applied to the initial and final states. There are two sources of the initial entropy or the initial velocity dispersion σ: thermal velocities of dark matter particles at the decoupling and peculiar velocities in the case of adiabatic perturbations.

The thermal part can be found from the distribution function at the kinetic decoupling instant t_d [2, Section 8.3.2]. The neutralino gas is nonrelativistic and nondegenerate at the decoupling time t_d, and hence the Maxwell distribution is a good approximation at that time:

$$f_p(p)\,\mathrm{d}^3r\,\mathrm{d}^3p = \frac{\rho_m}{m(2\pi m k_B T)^{3/2}} \exp\left(-\frac{p^2}{2mk_B T}\right) \mathrm{d}^3r\,\mathrm{d}^3p\,. \quad (38)$$

Here, m is the dark matter particle mass and ρ_m is the dark matter density, which can be expressed through the temperature in the Universe at any time from the local entropy conservation law $g_* T^3 a^3 =$ const, where g_* is the effective number of the degrees of freedom at the temperature T. The core distribution function is smaller than the initial distribution function that has a maximum at $p = 0$. Hence, $f_c < f_p(p = 0)$. For the isothermal density profile in the clump, this condition yields a constraint on the relative core radius:

$$\frac{R_c}{R} > \frac{2\pi^{1/2}\bar{\rho}^{1/4} T_d^{3/4}}{3^{1/4} G^{3/4} M^{1/2} m^{3/4} \rho_m^{1/2}(t_d)}\,. \quad (39)$$

In this calculation, we have used the fact that for the isothermal density profile $\rho(r) = \rho_c(r/R_c)^{-2}$, the relative core radius $x_c = R_c/R$ is expressed as $x_c = (\bar{\rho}/3\rho_c)^{1/2}$, where $\bar{\rho}$ and ρ_c are the mean and central clump density.

In the constraints found from the Liouville theorem, peculiar velocities that are generated by the gravitational instability can play a role similar to that of thermal velocities. The velocity of the increasing perturbation mode is smaller than the peculiar velocity in (14) by a factor of 2/5 [128]. After the time t_{eq}, the decreasing mode rapidly decays, and peculiar velocities are formed that later increase with time as $t^{1/3}$. However, the dark matter density in the Universe decreases as t^{-2}, and hence the distribution function in the phase volume decreases. We consider a time instant close to $t \sim t_{eq}$. By calculations similar to those given above with the substitution of thermal velocities by peculiar ones, we find the core radius as $R_c/R \simeq 0.01\delta_{eq}^{9/2}$. The results of calculations of R_c/R for three example cases are listed in the Table (for the neutralino mass $m = 100$ GeV and the decoupling temperature $T_d \approx 25$ MeV), which shows that the peculiar velocities are unimportant for standard clumps, but can become decisive for superdense clumps.

4.5 Entropy theory

To date, theoretical calculations and numerical N-body simulations of the halo density profiles on galactic scales have not been able to fully reproduce the results of observations. Some galaxy types (low surface brightness (LSB) galaxies and dwarf spheroids) demonstrate a sufficiently large core with the density that is constant or slowly increases toward the center. The density profile outside the central region is also better described by the Burkert profile than by analytic approximations of numerical simulations (see Section 4.9 for more details). In this connection, new factors should be sought to describe this discrepancy.

In [79], effects were found that can be responsible for the observed density profiles, including the initial entropy due to the peculiar velocities of small perturbations on the halo background and entropy generation during nonlinear clustering. In [79], the initial entropy was calculated analytically, and the generated entropy was taken from the results of N-body calculations. Presently, numerical modeling is the only tool capable of tracking the mean distribution function. In [79], by uniting the initial and generated entropies, the entropy function was found and the dark matter halo density profiles on galactic scales were calculated. It turns out that taking these effects into account enables significantly improving the agreement of the calculated density profile with observations. The additional entropy provides more effective core formation (in [79], the profiles with $\beta \leqslant 1$ are referred to as the core). An important element of the entropy theory is also that the initial Gaussian density distribution

Table. Three examples of clump parameters and the relative core radii caused by different effects discussed in the text.

Example	$M/M_\odot$	$\bar{\rho}$, g cm^{-3}	δ	x_c, thermal velocities*	x_c, peculiar velocities**	x_c, annihilation***
1	10^{-6}	3×10^{-23}	$\delta_{eq} = 0.009$	4×10^{-3}	6×10^{-12}	2.6×10^{-5}
2	10^{-6}	4.2×10^{-16}	$\delta_h = 0.05$	2.4×10^{-1}	1×10^{-1}	1×10^{-1}
3	10^{-1}	2.5×10^{-17}	$\delta_{eq} \simeq 1$	4×10^{-4}	1×10^{-2}	2.5×10^{-2}

* Bounds on $x_c = R_c/R$ from the Liouville theorem.
** Bounds on $x_c = R_c/R$ from peculiar velocities.
*** Bounds on R_c/R from annihilation.

produces a sufficiently broad distribution of the galactic central core properties.

The entropy theory enabled explaining density profiles of sufficiently massive galaxies. However, for low-mass galaxies, the entropy corrections are small due to the low initial entropy, which is caused by small peculiar velocities in low-mass halos [79]. Therefore, the applicability of the entropy theory to small-scale clumps considered here requires additional inspection. As shown in Section 4.4, the initial entropy can be important for superdense clumps.

Calculations using entropy and the Liouville theorem are useful because they give some general constraints and predictions without the need for detailed study of complicated gravitation dynamics. Another version of the entropy function was also used in [170] to study phase mixing processes and violent relaxation.

4.6 Tidal effects on the density profile

Modification of the density profile at the formation stage is possible due to tidal forces from external perturbations or internal inhomogeneities of the medium. These factors cause particles in a forming clump to acquire angular momentum, which leads to the central density profile flattening and, possibly, to the formation of a core [39, 119, 171].

In the framework of the simple spherical model considered in Section 3.1, with the correction due to tidal forces taken into account, we find the characteristic scale at which the density profile can have a kink [39]:

$$x_c = \frac{R_c}{R} \simeq 0.3 \nu^{-2} f^2(\delta_{eq}) , \tag{40}$$

where ν is the peak amplitude expressed in units of the rms perturbations introduced in Section 3.1, and the function $f \sim 1$. For perturbations with $\nu \sim 0.5-0.6$, $x_c \sim 1$, i.e., the corresponding clumps are destroyed by tidal forces already at the formation stage. In [119], it was found that the angular momentum of dark matter particles modifies the density profile to produce a kink similar to that in the NFW profile and to form an effective core in the dark matter halo center. Similar results were also obtained in [171–174]. In [159], the core radius $R_c/R \sim 3 \times 10^{-7}$ was estimated from an examination of nonradial velocities.

The tidal forces partially prevent the appearance of the central singularity of the density (or decrease the density divergence) during evolution of the clump, but if this singularity (a very high density in the clump center) has already been formed in some way, then the tidal interactions cannot disintegrate it any more due to the adiabatic invariant conservation. Indeed, core particles in the clump oscillate along orbits with a very high frequency, and therefore slowly varying tidal forces cannot affect their motion. Clumps, and especially their cores, can be destroyed only at later stages of evolution due to tidal interaction with stars and galactic discs.

4.7 Annihilation limit of the maximum density

In [175], the maximum central density in the clump was estimated using the annihilation rate and the time elapsed after clump formation,

$$\rho(r_{min}) \simeq \frac{m}{\langle \sigma v \rangle (t_0 - t_f)} , \tag{41}$$

where t_0 is the present time and t_f is the clump formation time. According to this estimate, the core radius increases with time due to annihilation losses of particles in orbits passing near the clump center. For the isothermal density profile $\rho(r) \propto r^{-2}$, the core radius

$$\frac{R_c}{R} \simeq \left(\frac{\langle \sigma v \rangle \, t_0 \bar{\rho}}{3m} \right)^{1/2} \tag{42}$$

is listed in the Table for the annihilation cross section $\langle \sigma v \rangle \simeq 3 \times 10^{-26}$ cm^3 s^{-1} corresponding to thermal particle creation and $m = 100$ GeV. This approach assumes that particle orbits near the clump center are not refilled after annihilation of their particles. The value in (41) was used to calculate the annihilation signal from ultra-compact mini-halos in [103, 149–152, 158, 159].

The opposite case with compensation of losses was considered in [176, 177]. The authors of [176] inferred the core radius from the annihilation limit at the dark matter halo formation stage. The minimal radius was obtained from the condition that the characteristic annihilation time is of the order of the Jeans instability time, $t_{halo} \sim (G\bar{\rho})^{-1/2}$, because this time gives the characteristic halo formation time scale. The characteristic core radius in that case is

$$x_c^2 \simeq \frac{\langle \sigma_{ann} v \rangle \rho^{1/2}}{G^{1/2} m} . \tag{43}$$

In [177], the core radius of the already formed clump was found by assuming a permanent hydrodynamic flow of dark matter onto the clump center. The free-fall time of a particle onto the clump center was assumed to be equal to the characteristic annihilation time in the core, and the flow was assumed to be permanently refilled by new particles. This approach yields the most conservative estimate of the core radius.

In a real clump, external gravitational perturbations must lead to the complete or partial regeneration of orbits with low angular momenta passing through the clump core. The orbit refilling leads to a higher central density than the one in (41).

4.8 Gravothermal catastrophe for superheavy particles

Superheavy particles with masses $m \geqslant 10^{11}$ GeV can be born immediately after the inflation stage due to a nonstationary gravitational field or other mechanisms; they can also be dark matter particles [20–22, 178–180]. Several constraints on the possible properties of super-heavy particles are discussed in review [113].

If a superdense clump consists of superheavy particles, an interesting effect, called the 'gravothermal catastrophe' in stellar dynamics, can occur [164, 181]. In globular stellar clusters, the instability and the gravothermal catastrophe are developed due to binary gravitational scatterings of stars. A similar process can become the dominant evolutionary factor of superdense clumps that formed early at the RD stage and consist of superheavy dark matter particles, which scatter on each other like stars.

In the gravothermal catastrophe regime, particles are evaporated (ejected) from the clump cores, which are decreasing in radius. The time when the gravothermal catastrophe occurs is smaller than the Hubble time only for extremely dense clumps (see [164, 181] for more details). The singular density profile $\rho \propto r^{-2}$ resulting from the gravothermal catastrophe can be formally continued to very small radii R_c. There are physical effects that restrict the density: electroweak particle scattering, particle annihilation (considered in Section 4.7), and degenerate Fermi-gas pressure.

The results of calculations in [181] suggest that for superheavy fermions in superdense clumps, the Fermi degeneration is the crucial effect. The maximum core density and, accordingly, the core radius can be found by equating the momentum of a degenerate Fermi-gas particle to its virial momentum at the core boundary, $p_F = (3\pi^2)^{1/3}(\rho_c/m)^{1/3} = mv_c$, where $v_c = (GM_c/r_c)^{1/2}$ is the particle velocity at the core boundary. Expressing the core radius as $x_c = (\bar{\rho}/3\rho_c)^{1/2}$, we obtain

$$x_c^2 = \pi^2 \frac{\bar{\rho}}{m^4}\left(\frac{GM}{R}\right)^{-3/2}. \quad (44)$$

For example, for superdense clumps with the mass $M \sim 1 \times 10^5$ g, the central density $\bar{\rho} \sim 3 \times 10^3$ g cm^{-3}, and $R \sim 3$ cm, the core radius is $x_c \sim 10^{-11}$. We also note that superdense dark matter objects that are kept in equilibrium by dark matter Fermi-gas pressure were considered in [182].

4.9 Numerical *N*-body simulations

Presently, numerical N-body simulations already use arrays of $N \sim 10^9$ points, which allows achieving a mass resolution of three orders of magnitude. The galaxy formation modeling has shown that halos with simple scaling density profiles are formed. For example, the NFW profile [120] is expressed as

$$\rho_h(r) = \frac{\rho_0}{(r/R_s)(1 + r/R_s)^2}. \quad (45)$$

For the Galactic halo, $R_s = 20$ kpc, the halo size (its virial radius) is $R_{halo} = 200$ kpc, and the mean halo density at the distance $r = r_\odot = 8.5$ kpc from the Galactic center (the distance of the Sun from the center) is $\rho_{halo}(r_\odot) = 0.3$ GeV cm^{-3}. We also note that at distances from the center up to $r = r_\odot$, baryonic matter dominates in the gravitational potential. An alternative density profile was obtained in [183, 184]. This profile differs from the NFW one mainly in the central part. In the Moore profile, $\rho_h(r) \propto r^{-1.5}$ at small r. Another popular representation of the dark matter halo numerical simulations is the Einasto profile [185],

$$\rho_h(r) = \rho_0 \exp\left\{-\frac{2}{\alpha}\left[\left(\frac{r}{r_s}\right)^{\alpha} - 1\right]\right\}, \quad (46)$$

where $\alpha = 0.16-0.3$ and $r_s \simeq 20$ kpc, and the best phenomenological description of observational data is provided by the Burkert profile [186] (see [79] for a detailed discussion). The halo boundary is usually associated with the sphere of a radius R_{200} inside which the mean dark matter density increases by a factor of 200 relative to the mean cosmological density.

There have been attempts to explain the nature of the universal density profile obtained in numerical simulations. Some of them were mentioned above. In [187], the universal density profile appearance in hierarchical clustering models was explained by the competition of the dynamical friction process and tidal stripping of smaller halos assembled in larger ones. The dynamical friction tends to shift small dense halos toward the center of a large halo, such that its central density increases, and the tidal stripping destroys small halos as they move toward the center, which increases the mass at the periphery of a large halo.

In observations, the structure of the central parts of dark matter halos has not yet been finally established. It remains unknown how close to the center the density continues to increase. There are some galaxy classes (LSB galaxies and some dwarfs) that, according to dynamical models, demonstrate not a central density peak but a core with a slowly increasing or even constant density. This discrepancy with numerical modeling results can be successfully explained by the entropy theory discussed in Section 4.5.

Numerical simulations, for example, Aquarius [188] (extensive numerical simulations are sometimes given proper names, such as Aquarius, Millenium, or Aquila) have revealed the presence of substructures (clumps) on mass scales down to $\sim 10^6 M_\odot$, which is the dynamical mass resolution of the calculations. The obtained clump mass function is $\propto M^{-1.9}$, and the fraction of clumped dark matter mass decreases from the periphery to the center. Apparently, this is due to a more effective tidal disruption of clumps in the central dense parts. The annihilation or decay of dark matter particles in such clumps can produce an inhomogeneous high-energy photon sky background, but this effect has not yet been discovered [63–65]. There is a problem of large-clump overproduction here: according to numerical simulations, too many clumps with dwarf-galaxy masses are formed, but astronomical observations of the Local Group of galaxies have not found the predicted number of dwarf galaxies. Presumably, the issue can be resolved by assuming that the 'extra' large clumps form dark galaxies consisting mostly of dark matter, almost without stars. Stars may not have been formed there due to the absence of effective cooling mechanisms of low-mass baryonic halos.

Many numerical simulations of large halos in galaxies and galaxy clusters have been performed, but only a few studies have dealt with low-mass clump modeling [44, 51, 77, 82]. Numerical modeling of small-scale clumps usually stops before the galaxy formation epoch. For example, in [51], the calculations are restricted to the redshift interval $z \sim 30-500$. The point is that the modeling space region itself enters the nonlinear regime at $z \sim 30$ (this occurs quite rapidly, because the perturbation spectrum at small scales is almost flat), after which it is already difficult to follow the evolution of small-scale clumps inside this region. Numerical simulations have revealed that the mass function of substellar-mass clumps is close to the power-law form $\propto M^{-1.9}$, as obtained in modeling large substructures in galaxies, and these mass functions match quite well when extrapolating to intermediate scales.

The internal density profile in a single clump with a minimal mass was numerically calculated in [77], which is an important result. The obtained density profile can be approximated by a power law $\propto r^{-\beta}$ with $\beta = 1.5-2.0$, which is in good agreement with the theoretical prediction $\beta = 1.7-1.8$ in [55–57]. In [82], the value $\beta = 1.5$ was obtained. The tendency of β to increase in passing from clumps formed via hierarchical clustering of small-scale objects to clumps originated from isolated density perturbations was revealed in [51]. It was shown that in hierarchical clustering, an NFW profile with $\beta = 1$ at the center and a density profile with $\beta \simeq 1.4$ at the center are produced from isolated perturbations. Clumps with the minimal mass M_{min} are also related to clumps formed from isolated perturbations because the perturbation spectrum has a cutoff at smaller masses (more precisely, the Gaussian distribution of perturbations should be taken into account, and therefore even clumps with equal masses M_{min} can show different properties). In [51], from the standpoint of density profile formation,

the boundary between hierarchical and nonhierarchical regimes was found to lie at $\sim 10^2 M_{\min}$.

Numerical modeling of clumps on galaxy scales revealed the dependence of the concentration parameter $C_{\mathrm{NFW},200} = R_{200}/r_{\mathrm{s}}$ in Navarro–Frenk–White formula (45) on the halo mass: $C_{\mathrm{NFW},200} = 8.45 \times (M/10^{12} M_{\odot})^{-0.11}$. However, as pointed out in [51], this dependence cannot be applied to low-mass clumps. A more complicated non-power-law dependence found in [189] can be used. If we ignore this fact and use the mass function $\propto M^{-0.11}$, as has been assumed in some papers, then the annihilation signal enhancement by clumps can be overestimated by 2 to 3 orders of magnitude [51].

In the calculations in [51], caustics similar to those in the Bertschinger [76] and Gurevich–Zybin [55–57] models were found in the formed clumps. According to the estimates in [51], the presence of these caustics can increase the annihilation luminosity of the clump immediately after formation by a factor of more than 1.5 in comparison with that of a clump with a smooth density profile. However, the caustic enhancement of the annihilation signal decreases with time, as the caustics are destroyed by dark matter stream mixing inside the clumps.

We emphasize that the problem of the maximum central clump density, or the problem of the core radius in numerical modeling, has not been solved so far, apparently due to the insufficient mass resolution. Simulations in [77] found a trace of a core with $x_{\mathrm{c}} \simeq 10^{-2}$ (see Fig. 2 in [77]); however, in the calculations in [51, 82], the core was not resolved for x_{c} as small as $\simeq 10^{-3}$.

5. Clumps with minimal mass

Although the spectrum of perturbations generated at the inflation stage can be extended down to microscopic scales, there are some effects that cut off (suppress) the low-scale part of the spectrum at later epochs of cosmological evolution, preventing low-mass clump formation. Many papers have been devoted to the calculation of the minimum possible mass $M_{\min}$, with results that differ by several orders of magnitude, even using similar assumptions about the nature of dark matter particles. However, to date, the problem of $M_{\min}$ has largely been solved and uncertainties are not too large.

We illustrate the spectral cutoff using the 'free streaming' effect. Cold dark matter particles at high temperatures $T > T_{\mathrm{f}} \sim 0.05 m_{\chi}$ are found in chemical equilibrium with cosmic plasma, when the particle number density is determined solely by the temperature. After freezing at $t > t_{\mathrm{f}}$ and $T < T_{\mathrm{f}}$, the dark matter particles stay in kinetic equilibrium with the plasma for some time, as the particle gas temperature T_{χ} follows the plasma temperature T, but their number in a fixed volume remains constant. However, at this stage, the dark matter particles are not fully connected with the plasma any more. The exchange of momentum between the dark matter particles and radiation leads to spatial diffusion of the dark matter particles. They escape small-scale perturbations via diffusion, and therefore the flattening (decay) of perturbations occurs at some mass scale M_{D}.

When the energy relaxation time τ_{rel} of dark matter particles decreases below the Hubble time $H^{-1}(t)$, the particles lose equilibrium with plasma. These conditions determine the kinetic decoupling time t_{d}. The kinetic decoupling time was estimated, for example, in [61]. At $t \geqslant t_{\mathrm{d}}$, the dark matter particles move in the free steaming regime, and all perturbations are flattened on the scale

$$\lambda_{\mathrm{fs}} = a(t_0) \int_{t_{\mathrm{d}}}^{t_0} \frac{v(t')\,\mathrm{d}t'}{a(t')} \tag{47}$$

(where $v(t)$ is the velocity of a dark matter particle) and on smaller scales. For a nonrelativistic particle, $v(t) \propto 1/a(t)$. The corresponding minimal mass of a dark matter clump at the time t_0 is

$$M_{\mathrm{fs}} = \frac{4\pi}{3}\, \rho_{\chi}(t_0)\, \lambda_{\mathrm{fs}}^3\,, \tag{48}$$

which is much larger than M_{D}.

The choice of a mathematical formalism needed to calculate the minimal mass depends on how close the considered scales are to the cosmological horizon and whether macroscopic motions of radiation (including deviations from the perfect fluid model) are important. On scales much smaller than the horizon size, the nonrelativistic Boltzmann equation is sufficient to describe the physics of the phenomena if there are no such macroscopic motions. In Sections 5.1–5.6, we perform nonrelativistic calculations, and then show in which situations relativistic effects become important and describe the results of relativistic calculations.

5.1 Neutralino–lepton scattering cross-section

To calculate the minimal mass $M_{\min}$ of a clump, the scattering cross section of dark matter particles on cosmic plasma particles is of fundamental importance. This cross section is strongly model dependent. We consider the 'standard' neutralino dark matter model in detail. This model is now believed to be the most plausible one; however, other models cannot be excluded. Eventually, the true model can be established only after experimental registration of dark matter by direct or indirect means or by producing dark matter particles in accelerator experiments. We consider the neutralino to be a pure bino ($\chi = \tilde{\mathrm{B}}$).

The scattering cross section of left fermions on a neutralino $\mathrm{f_L} + \chi \to \mathrm{f_L} + \chi$ by angles θ_{12} in the neutralino rest frame is given by [39]

$$\left(\frac{\mathrm{d}\sigma_{\mathrm{el}}}{\mathrm{d}\Omega}\right)_{\mathrm{f_L}\chi} = \frac{\alpha_{\mathrm{EM}}^2}{8\cos^4\theta_{\mathrm{W}}} \frac{\omega^2(1+\cos\theta_{12})}{(m^2 - \tilde{m}_{\mathrm{L}}^2)^2}\,, \tag{49}$$

where $\omega \gg m_{\mathrm{f}}$ is the fermion ($\mathrm{f_L}$) energy in the neutralino rest frame, m is the neutralino mass, $\tilde{m}_{\mathrm{L}}$ is the left fermion mass, and α_{EM} is the electromagnetic coupling constant. For the scattering $\mathrm{f_R} + \chi \to \mathrm{f_R} + \chi$, we have

$$\left(\frac{\mathrm{d}\sigma_{\mathrm{el}}}{\mathrm{d}\Omega}\right)_{\mathrm{f_R}\chi} = 16 \left(\frac{\mathrm{d}\sigma_{\mathrm{el}}}{\mathrm{d}\Omega}\right)_{\mathrm{f_L}\chi}\,, \tag{50}$$

under the condition that $m_{\mathrm{L}} = \tilde{m}_{\mathrm{R}}$, where $\tilde{m}_{\mathrm{R}}$ is the right sfermion mass. We are interested in the scattering processes $\nu + \chi \to \nu + \chi$ and $\mathrm{e} + \chi \to \mathrm{e} + \chi$. In the first case, the cross section is given by (49), and in the second case, it is determined by the sum of scatterings $\mathrm{f_L} + \chi \to \mathrm{f_L} + \chi$ and $\mathrm{f_R} + \chi \to \mathrm{f_R} + \chi$, i.e., is larger than (49) by a factor of 17. We use the notation $\tilde{m}$ for both left and right selectrons and sfermions and $\tilde{M}^2 = \tilde{m}^2 - m^2$.

We note that for order-of-magnitude estimates, the scattering cross section of neutralinos on leptons can be written in the simple form $\sigma \approx T^2/M_{\sigma}^4$ [62], where T is the cosmic plasma temperature and M_{σ} is of the order of the electroweak interaction scale (~ 100 GeV).

5.2 Kinetic decoupling

We use the kinetic equation formalism to study the process of dark matter particles losing kinetic equilibrium with the cosmic plasma. Following [128], we introduce the distribution function $f(x,p,t)$ in comoving coordinates $\mathbf{x}$ and momenta $\mathbf{p} = ma^2\dot{\mathbf{x}}$ (the momentum of a freely moving particle defined in this way is constant). The dark matter particle density is

$$\rho(x,t) = \frac{m}{a^3}\int \mathrm{d}^3 p f(x,p,t) = \bar{\rho}_\chi(t)\big(1+\delta(x,t)\big)\,. \tag{51}$$

The kinetic equation with the collision integral in the Fokker–Planck form [190] can be written as

$$\frac{\partial f}{\partial t} + \frac{p_i}{ma^2}\frac{\partial f}{\partial x_i} - m\,\frac{\partial \phi}{\partial x_i}\frac{\partial f}{\partial p_i} = D_p(t)\,\frac{\partial}{\partial p_i}\left(\frac{p_i}{mTa^2}\,f + \frac{\partial f}{\partial p_i}\right), \tag{52}$$

where ϕ is the gravitational potential, which can be neglected in the epochs $t \leqslant t_{\mathrm{eq}}$, $T(t)$ is the temperature of the surrounding plasma,

$$t = \frac{2.42}{\sqrt{g_*}}\left(\frac{T}{1\ \mathrm{MeV}}\right)^{-2}\ [\mathrm{s}]\,, \tag{53}$$

where g_* is the effective number of degrees of freedom, and $D_p(t)$ is the diffusion coefficient in the momentum space. We let

$$n_0(\omega) = \frac{1}{2\pi^2}\,\frac{\omega^2}{\exp(\omega/T)\pm 1}\,. \tag{54}$$

denote the number density of background relativistic fermions or bosons with one polarization and with the energy ω. According to [190],

$$D_p(t) = \frac{g_{\mathrm{f}}}{3}\int \mathrm{d}\Omega \int \mathrm{d}\omega\, n_0(\omega)\left(\frac{\mathrm{d}\sigma_{\mathrm{el}}}{\mathrm{d}\Omega}\right)_{\mathrm{f}_{\mathrm{L}}\chi}(\delta p)^2\,, \tag{55}$$

where the factor $g_{\mathrm{f}} = 40$ is obtained from counting the degrees of freedom in neutralino–fermion collisions: three neutrinos and antineutrinos (or $\nu_{\mathrm{L}}^{\mathrm{c}}$ in the case of a Majorana neutrino) yield six degrees of freedom, e_{L} and $e_{\mathrm{L}}^{\mathrm{c}}$ (which have two degrees of freedom and two right (singlet) states for electrons and positrons) yield 34 degrees of freedom because their cross section is larger by a factor of 17. Equation (52) with diffusion coefficient (55) coincides with Eqn (16) in [191], up to a numerical factor of the order of unity in the expression for D_p.

We consider the exit (decoupling) of neutralinos from kinetic equilibrium in a homogeneous universe, when the term $\partial/\partial x_i$ in (52) can be neglected. The temperature of the neutralino gas is determined as

$$\int p_i p_j f\,\mathrm{d}^3 p = \bar{\rho}_\chi a^5 T_\chi(t)\,\delta_{ij}\,. \tag{56}$$

Multiplying both sides of (52) by $p_i p_j$ and integrating over $\mathrm{d}^3 p$, we obtain

$$\frac{\mathrm{d}T_\chi}{\mathrm{d}t} + 2\,\frac{\dot{a}}{a}\,T_\chi - \frac{2D_p(t)}{ma^2}\left(1-\frac{T_\chi(t)}{T(t)}\right) = 0\,. \tag{57}$$

The initial condition $T_\chi(t_{\mathrm{i}}) = T(t_{\mathrm{i}})$ for Eqn (57) can be chosen at the freezing time $t = t_{\mathrm{f}}$, as in [191], or at any time t_{i} from the interval $t_{\mathrm{f}} < t_{\mathrm{i}} \ll t_{\mathrm{d}}$, which is more convenient. The solution of Eqn (57) has the form

$$\frac{T_\chi(t)}{T_{\mathrm{d}}} = \frac{1}{\tau}\left[\tau_{\mathrm{i}}^{-1/2}\exp\left(\frac{1}{4\tau^2}-\frac{1}{4\tau_{\mathrm{i}}^2}\right) + \frac{1}{2}\exp\left(\frac{1}{4\tau^2}\right)\int_{\tau_{\mathrm{i}}}^{\tau}\mathrm{d}^3 x\, x^{-5/2}\exp\left(\frac{1}{4x^2}\right)\right], \tag{58}$$

where we introduce the dimensionless variable $\tau = t/t_{\mathrm{d}}$ and the notation

$$t_{\mathrm{d}} \simeq 10^{-3}\left(\frac{m}{100\ \mathrm{GeV}}\right)^{-1/2}\left(\frac{\tilde{M}}{0.2\ \mathrm{TeV}}\right)^{-2}\left(\frac{g_*}{10}\right)^{-3/4}[\mathrm{s}]\,, \tag{59}$$

$$T_{\mathrm{d}} = 30\left(\frac{m}{100\ \mathrm{GeV}}\right)^{1/4}\left(\frac{\tilde{M}}{0.2\ \mathrm{TeV}}\right)\left(\frac{g_*}{10}\right)^{1/8}[\mathrm{MeV}]\,. \tag{60}$$

The asymptotic form of solution (58) is $T_\chi/T_{\mathrm{d}} = \tau^{-1/2}$ at $\tau \ll 1$ and $T_\chi/T_{\mathrm{d}} = \tau^{-1}\Gamma(3/4)/2^{1/2}$ (where $\Gamma(...)$ is the gamma function) at $\tau \gg 1$, as it must be. From solution (58), we can see that the transition from the kinetic equilibrium of neutralinos with relativistic fermions to the nonequilibrium regime occurs very rapidly. Therefore, the treatment of diffusion separately from free streaming seems to be justified.

The time t_{d} and the temperature T_{d} of the kinetic decoupling of the neutralino can also be derived from the simple condition

$$\frac{1}{\tau_{\mathrm{rel}}} \simeq H(t)\,, \tag{61}$$

where $H(t) = 1/(2t)$ is the Hubble parameter and $\tau_{\mathrm{rel}}(T)$ is the energy relaxation time at the electron–neutrino gas temperature T. The relaxation time τ_{rel} is determined by the scattering of neutralinos on the fermions ν_{L}, e_{L}, and e_{R}. The neutralino can be considered to be at rest because its rest-mass frame coincides with the center-of-mass frame up to $\sqrt{T/m_\chi}$. Let δp be the momentum acquired by the neutralino in one scattering: $(\delta p)^2 = 2\omega^2(1-\cos\theta)$, where ω and θ are the energy and the scattering angle of the fermion. Then the relaxation time can be written as

$$\frac{1}{\tau_{\mathrm{rel}}} = \frac{1}{E_{\mathrm{k}}}\frac{\mathrm{d}E_{\mathrm{k}}}{\mathrm{d}t} = \frac{g_{\mathrm{f}}}{2E_{\mathrm{k}}m}\int \mathrm{d}\Omega \int \mathrm{d}\omega\, n_0(\omega)\left(\frac{\mathrm{d}\sigma_{\mathrm{el}}}{\mathrm{d}\Omega}\right)_{\mathrm{f}_{\mathrm{L}}\chi}(\delta p)^2\,, \tag{62}$$

where $E_{\mathrm{k}} \simeq (3/2)\,T$ is the mean kinetic energy of the neutralino, and $(\mathrm{d}\sigma_{\mathrm{el}}/\mathrm{d}\Omega)_{\mathrm{f}_{\mathrm{L}}\chi}$ is given by (49). After integrating in (62), we arrive at

$$\frac{1}{\tau_{\mathrm{rel}}} = \frac{40\Gamma(7)\,\alpha_{\mathrm{EM}}^2}{9\pi\cos^4\theta_{\mathrm{W}}}\,\frac{T^6}{\tilde{M}^4 m}\,. \tag{63}$$

With (53), Eqn (61) implies expressions (59) and (60).

5.3 Diffusion cut-off of the perturbation spectrum

We consider Eqn (52) prior to the kinetic decoupling epoch, i.e., for $t \ll t_{\mathrm{d}}$. It is possible to find the first two moments by integrating (52), first over $\mathrm{d}^3 p$ and then over $p_i\,\mathrm{d}^3 p$. After substituting the first of the obtained expressions into the second one, we find an equation for the Fourier components:

$$\frac{\partial^2\delta}{\partial t^2} + 2\,\frac{\dot{a}}{a}\,\frac{\partial\delta}{\partial t} + D_p(t)\,\frac{1}{mTa^2}\,\frac{\partial\delta}{\partial t} = \frac{k_i k_j}{\bar{\rho}_\chi a^7 m}\int p_i p_j f\,\mathrm{d}^3 p\,. \tag{64}$$

In the limit $\tau \ll 1$, we can neglect the first and second terms in (64) to obtain the equation

$$\frac{\partial\delta(\mathbf{x},t)}{\partial t} = \frac{D(t)}{a^2(t)}\,\Delta_{\mathbf{x}}\,\delta(\mathbf{x},t) \tag{65}$$

with the diffusion coefficient

$$D = \frac{3\pi\cos^4\theta_{\mathrm{W}}\tilde{M}^4}{40\Gamma(6)\,\alpha_{\mathrm{EM}}^2 T^5}\,. \tag{66}$$

The diffusion coefficient $D(t)$ depends on time via $T(t)$.

We find the minimal mass in the perturbation spectrum caused by neutralino diffusion from the perturbation region. The solution of (65) for the Fourier components has the form

$$\delta_{\mathbf{k}}(t) = \delta_{\mathbf{k}}(t_{\mathrm{f}})\,\exp\left[-Cg_*^{5/4}\tilde{M}^4(t^{5/2}-t_{\mathrm{f}}^{5/2})\,k^2\right], \tag{67}$$

where $C = \mathrm{const}$. The factor $Cg_*^{5/4}\tilde{M}^4(t^{5/2}-t_{\mathrm{f}}^{5/2})$ in front of k^2 in (67) is the diffusion length square $\lambda_{\mathrm{D}}^2(t)/a^2(t)$ in comoving coordinates. Then the minimal mass due to the neutralino diffusion from the fluctuation region is

$$M_{\mathrm{D}} = \frac{4\pi}{3}\,\rho_\chi(t_{\mathrm{d}})\,\lambda_{\mathrm{D}}^3(t_{\mathrm{d}}) = 5\times10^{-12}\left(\frac{m}{100\ \mathrm{GeV}}\right)^{-15/8} \times\left(\frac{\tilde{M}}{0.2\ \mathrm{TeV}}\right)^{-3/2}\left(\frac{g_*}{10}\right)^{-15/16} M_\odot. \tag{68}$$

The expression for functional dependence (67), obtained in the diffusion approximation, coincides with the corresponding expression obtained by other means in [191].

5.4 Free streaming

In the limit case $\tau \gg 1$, i.e., after the kinetic decoupling, Eqn (52) takes the simple form

$$\frac{\partial f}{\partial t} + \frac{p_i}{ma^2}\,\frac{\partial f}{\partial x_i} = 0\,. \tag{69}$$

Its solution in the Fourier space is

$$f \propto \exp\left(\frac{\mathrm{i}k_j p_j}{ma(t_{\mathrm{d}})}\,g(t)\right), \tag{70}$$

where

$$g(t) = a(t_{\mathrm{d}})\int_{t_{\mathrm{d}}}^{t}\frac{\mathrm{d}t'}{a^2(t')}\,. \tag{71}$$

Solution (70) is also valid with good accuracy for $\tau \geqslant 1$, because, according to (58), the kinetic decoupling proceeds very rapidly. The momentum distribution at the decoupling time is given by Maxwell distribution (38). Integrating the product of (38) and (70) over d^3p, we obtain

$$n_{\mathbf{k}}(t) = n_{\mathbf{k}}(t_{\mathrm{d}})\exp\left(-\frac{1}{2}\,k^2 g^2(t)\,\frac{T_{\mathrm{d}}}{m}\right), \tag{72}$$

i.e., until the instant t, all perturbations are flattened due to free steaming on the physical scale

$$\lambda_{\mathrm{fs}}(t) = a(t)\,g(t)\left(\frac{T_{\mathrm{d}}}{m_\chi}\right)^{1/2}. \tag{73}$$

This scale corresponds to clumps with the minimal mass

$$M_{\mathrm{fs}}(t) = \frac{4\pi}{3}\,\rho_{\mathrm{m}}(t)\,\lambda_{\mathrm{fs}}^3(t)\,, \tag{74}$$

where $\rho_{\mathrm{m}}(t) = \rho_{\mathrm{eq}}a_{\mathrm{eq}}^3/a^3(t)$. In the RD epoch, $M_{\mathrm{fs}}(t)$ increases logarithmically with time. This growth saturates at the matter-dominated stage. The resultant mass M_{min} at the instant t_0 can easily be found from the Friedmann equation:

$$M_{\mathrm{min}} = \frac{\pi^{1/4}}{2^{19/4}3^{1/4}}\,\frac{\rho_{\mathrm{eq}}^{1/4}t_{\mathrm{d}}^{3/2}}{G^{3/4}}\left(\frac{T_{\mathrm{d}}}{m}\right)^{3/2}\ln^3\left(\frac{24}{\pi G\rho_{\mathrm{eq}}t_{\mathrm{d}}^2}\right). \tag{75}$$

Using (59) and (60), we obtain

$$M_{\mathrm{min}} \simeq 2\times10^{-7}\left(\frac{m}{100\ \mathrm{GeV}}\right)^{-15/8}\left(\frac{\tilde{M}}{0.2\ \mathrm{TeV}}\right)^{-3/2} \times\left(\frac{g_*}{10}\right)^{-15/16}\left(\frac{\Lambda^*}{83}\right)^3 M_\odot\,, \tag{76}$$

where Λ^* is the logarithm from Eqn (75).

Thus, there are two processes of cosmological perturbation flattening in the neutralino gas. The first is neutralino diffusion due to neutralino scattering on neutrinos, electrons, and positrons. This process is effective as long as neutralinos remain in kinetic equilibrium with the cosmic plasma. Before the decoupling instant t_{d}, all perturbations with masses $M < M_{\mathrm{D}} \simeq 10^{-13}-10^{-12}M_\odot$ are smoothened. The second process is the free streaming of neutralinos. It starts at later epochs at $t > t_{\mathrm{d}}$, flattens larger perturbations with $M \leqslant M_{\mathrm{fs}}$, and ultimately determines the minimum possible mass M_{min} [formula (76)] in the present-day mass function of clumps. We note that the supersymmetry parameters are usually chosen in the literature such that M_{min} is of the order of Earth's mass ($\sim 10^{-6}M_\odot$).

Accurate calculations of the perturbation spectrum transformation due to diffusion and free streaming, taking GR corrections to the evolution equations into account, are presented in [41, 90].

5.5 Cosmological horizon and acoustic oscillation effects

In Sections 5.2–5.4, we assumed that all the considered scales, including the free streaming scale, are much smaller than the horizon size. This is indeed the case for a wide range of supersymmetry parameters. However, the supersymmmetry parameters that yield a low value of T_{d} are often considered. In this case, horizon effects, such as acoustic oscillation and an effect similar to Silk decay, become important. These effects cut off the perturbation spectrum at high masses and thus become decisive for M_{min} calculations. Moreover, according to the calculations in [46], the mass spectrum cutoff may not be exponential, and the mass function can increase in accordance with a power law, $\propto M^{-1/3}$, toward low-mass clumps, although the integral contribution of clumps described by this asymptotic behavior to the total mass of clumps is small.

Qualitatively, the role of the cosmological horizon in cutting off the perturbation spectrum can be represented as follows. The evolution of perturbations with masses $M \ll M_{\mathrm{d}}$ and $M \gg M_{\mathrm{d}}$ differ greatly after the horizon crossing [62]. Such fluctuations do not produce a boost in the dark matter peculiar velocity, and therefore perturbations in dark matter do not grow logarithmically. After the kinetic decoupling, their amplitude is 'frozen' until the matter-dominating epoch

begins, and their evolution is described by the Meszaros solution. Thus, at masses close to $M \sim M_{\rm d}$, the perturbation spectrum demonstrates a cutoff and is flattened at smaller masses (or, possibly, has the form $\propto M^{-1/3}$ [46]).

In the opposite case $M \gg M_{\rm d}$, the peculiar velocities take the form $v_{\rm ph} \simeq \delta_{\rm h} c/3$ immediately after the horizon crossing [129]. Unlike thermal velocities, these peculiar velocities are regular and directed toward the perturbation center. Adiabatic perturbations grow according to the law $\delta \propto \ln(t) + \text{const}$ due to the peculiar velocity evolution, $v_{\rm p}(t) \simeq v_{\rm ph} a(t_{\rm h})/a(t)$.

The effect of acoustic oscillations on dark matter density perturbations near the horizon crossing time was studied in [62]. As in the case of baryon acoustic oscillations, oscillations near the horizon scale appear in the dark matter perturbation spectrum.

The most detailed calculations of quasi-free streaming with friction for neutralinos were performed in [46], complementing the calculations in [62]. In [46], expressions for the decoupling temperature and minimal mass were obtained as

$$T_{\rm d} = 7.5\, C^{-1/4} g_*^{1/8} \left(\frac{m}{100\ \text{GeV}}\right)^{5/4} [\text{MeV}]\,, \tag{77}$$

$$M_{\rm min} = 7.59 \times 10^{-3}\, C^{3/4} \left(\frac{m\sqrt{g_*}}{100\ \text{GeV}}\right)^{-15/4} M_\odot\,, \tag{78}$$

with the dimensionless constant

$$C = 256\, (G_{\rm F} m_{\rm W}^2)^2 \left(\frac{\tilde{m}^2}{m^2} - 1\right)^{-2} \sum_L (b_L^4 + c_L^4)\,, \tag{79}$$

where $G_{\rm F}$ is the Fermi coupling constant, $G_{\rm F} m_{\rm W}^2 = 0.0754$, $m_{\rm W}$, $\tilde{m}$, and m are the respective masses of the W-boson, slepton, and neutralino, and b_L and c_L are the respective left and right chiral coefficients; the number of degrees of freedom at the decoupling time is $g_* = 43/4$. The value of C calculated in [39], which is related to the squared matrix element for $1 + \chi \to 1 + \chi$ scattering, differs from that in Eqn (78) by a factor of 1.6. According to (78), the kinetic decoupling under typical supersymmetry parameters, as assumed in [46], occurs at the temperature $T_{\rm d} = 22.6$ MeV, i.e., after the muon–antimuon annihilation but before the e^+e^- annihilation epoch, and the e^+e^- annihilation slightly modifies the perturbation spectrum [46]. The mass in (78), as in [62], is close to the mass inside the horizon at the decoupling time by the order of magnitude. Modeling of the cosmic plasma by a nonperfect fluid [61] gives another way to calculate the minimum mass.

We note that in calculations like those in [46, 62], methods of the relativistic theory of density perturbation evolution, taking the gravitational potential of radiation into account as long as effects near the cosmological horizon are considered.

5.6 The $M_{\rm min}$ mass for superheavy neutralinos

The assumption that dark matter was in chemical and thermal equilibrium with radiation is not necessary and is invalid for sufficiently heavy particles. In this case, the constraints on the minimal halo mass considered in Sections 5.2–5.5 are absent. If the equilibrium did occur, $M_{\rm min}$ would be very small for superheavy particles due to the early kinematic decoupling of clumps from the cosmic plasma [102].

Neutralinos in the superheavy supersymmetry proposed in [22] were considered to be superheavy dark matter particle candidates that interacted with radiation at early epochs. Superheavy supersymmetry is a unique renormalizable model that respects unitarity despite the particle masses that are much larger than the electroweak scale. For example, a neutralino with the mass $m = 10^{11}$ GeV $= 1.78 \times 10^{-13}$ g can be created gravitationally at the end of the inflation stage to provide the value $\Omega_\chi h^2 \approx 0.1$ derived from WMAP observations.

In the conditions of decoupling, $\tau_{\rm rel}^{-1} \simeq H$, the running coupling constant and mixing parameters at a temperature T are used as obtained from the Standard Model, $\sin^2\theta_{\rm W}(T) = 1/6 + 5\alpha(T)/[9\alpha_{\rm s}(T)]$. For $M_{\rm SUSY} = 10^{12}$ GeV, in the case of a bino and a Higgsino, we respectively find $T_{\rm d} \simeq 2\times 10^{11}$ GeV and $T_{\rm d} \simeq 2$ GeV. The dark matter mass inside the horizon at these temperatures is respectively $M_{\rm d} \simeq 6 \times 10^{-12}$ g and $M_{\rm d} \simeq 6 \times 10^{21}$ g. That is, in the case of the bino, the mass $M_{\rm d}$ is higher than the particle mass $m \sim 10^{11}$ GeV $= 1.78 \times 10^{-13}$ g by only a factor of 34.

The free-streaming scale and mass $\lambda_{\rm fs}$ for superheavy dark matter particles are very small. In the case of the bino, the decoupling time is $t_{\rm d} = 7 \times 10^{-30}$ s and $M_{\rm fs} \simeq 4.6 \times 10^{-11}$ g. The latter quantity is larger than the particle mass by only a factor of 260, and all masses of clumps starting from $M \sim 260m$ are possible. In the case of the Higgsino, $M_{\rm fs} \ll m$, and free streaming plays no role in the perturbation evolution. Hence, two mass scales, $M_{\rm d}$ and $M_{\rm fs}$, could play the role of the minimal clump mass $M_{\rm min}$. In the case of the bino, $M_{\rm fs} > M_{\rm d}$, and the cutoff in the mass function starts at $M_{\rm min} \sim M_{\rm fs}$. In the case of the Higgsino, $M_{\rm fs}$ is very small and $M_{\rm min} \sim M_{\rm d}$.

6. Formation of the clump mass function in early hierarchical clustering processes

Dark matter objects with the minimal mass $M_{\rm min}$ were the first gravitationally bound objects in the Universe. Clumps with larger masses, which in the case of the usual power-law spectra were formed at later epochs, consist of less massive clumps and are themselves captured by larger clumps. Most of the small-scale clumps that are present in larger and typically more massive clumps (which we call 'host' clumps) are destroyed by tidal forces. Hierarchical clustering on small scales is a rapid nonlinear process. The formation of new clumps and their capture by more massive objects occur almost simultaneously. Indeed, it follows from the form of the transfer function $T(k)$ that the power-law exponent of the perturbation spectrum on small scales is $n \approx n_{\rm s} - 4 \approx -3$, and the perturbation $\sigma(M) \propto M^{-(n+3)/6}$ is almost independent of M. This leads to a complication in N-body simulations [192]. The clumps are not fully virialized by the time they are captured by the host clumps; therefore, the adiabatic invariants do not prevent clumps from being destroyed at this stage, since the singular density profile in the clumps had not been formed by that time. The internal dynamical time in the clump is of the same order of magnitude as the time of its capture by the host clump.

The described picture of hierarchical clustering is valid only when the perturbation spectrum has no sharp peak, for example, is close to a power law. In peaked spectra, there are long periods without clustering: clumps formed from the peak region can be the only clump population for a long time, and only after a long time delay does the clump formation from spectral parts with larger scales begin and the clumps are

captured by these new structures. In Sections 6.1–6.3, we consider the standard power-law primordial perturbation spectrum and discuss the hierarchical clustering of clumps in a wide mass range.

6.1 Press–Schechter formalism

The Press–Schechter theory is based on the spherical model considered in Section 3.1. The spherical model yields the clump formation threshold $\delta(t) \geqslant \delta_c$ (a more precise criterion is given by the ellipsoidal collapse model), which allows calculating the statistical characteristics of dark matter halos being formed using perturbation properties at the linear stage. The probability that a dark matter particle is in the region with $\delta(t) \geqslant \delta_c$ (with flattening on the scale M) is expressed as

$$P(M) = \frac{1}{\sqrt{2\pi}\sigma(M)} \int_{\delta_c}^{\infty} \mathrm{d}\delta' \exp\left(-\frac{\delta'^2}{2\sigma^2(M)}\right). \qquad (80)$$

Then the differential number density of noncaptured (free) clumps, i.e., those that are not included in large host clumps, is given by the Press–Schechter formula [34]

$$\mathrm{d}n(t, M) = -2\frac{\bar{\rho}_0}{M}\frac{\mathrm{d}P(M)}{\mathrm{d}M}\,\mathrm{d}M = -\left(\frac{2}{\pi}\right)^{1/2}\frac{\bar{\rho}_0}{M\sigma(M)}\frac{\mathrm{d}\sigma(M)}{\mathrm{d}M}\,\nu\exp\left(-\frac{\nu^2}{2}\right)\mathrm{d}M, \qquad (81)$$

where $\nu = \delta_c/\sigma(M)$. In the generalized Press–Schechter theories [88] (see [33] for a very clear presentation), it was possible to construct a powerful mathematical formalism and to make many statistical predictions; in particular, the factor 2 in formula (81) was explained, which was not present in the original theory [91].

From the standpoint of searching for annihilation signatures, it is not only individual clumps with mass function (81) that are of interest; so are clumps captured inside other objects, in particular, inside the dark matter halo of our Galaxy. In the first approximation, the mass function of clumps in the halo at the halo formation time is given by formula (81), with the clump number density increase in proportion to the halo density growth taken into account. This statement is valid in the case where a big difference exists between the clump and halo masses, when the biasing effects are small.[1]

The initial mass function of clumps entering a large-scale halo at the instant of formation was calculated more precisely in [92] using the generalized Press–Schechter theory. Another original approach to the calculation of this mass function was used in [193], where the host halo was considered a part of a closed universe and the Press–Schechter mass function was calculated in this background. The Press–Schechter formalism was used in [194, 195] to study substellar mass function formation, and the authors of [195] concluded that effective clump formation begins only for masses $M \gg M_{\min}$. Those approaches ignore small-scale clump destruction by tidal forces, which modifies the initial mass function. To calculate the mass function of clumps, including clumps inside other structures, using only the statistical Press–Schechter theory is insufficient, and the dynamical clump destruction processes should be taken into account. The dynamical effects (tidal stripping and dynamical friction) have been studied only for large subhalo masses, $M \geqslant 10^6 M_\odot$ (see, e.g., [196]). For the small-scale clumps considered here, a quite different treatment is required, because the hierarchical clustering of such clumps proceeds very rapidly and on the same time scale that their internal density profile is established.

[1] Biasing in astrophysics means the dependence of the properties of galaxies being formed on the mean density of matter on scales greatly exceeding the galaxy scales.

6.2 Tidal processes

The tidal destruction of clumps is a complicated process that depends on many factors: the clump formation history, the density profile in the host clump, the presence of other structures in the host clump, the orbital parameters of individual clumps in the host clump, and so on. These factors can be sufficiently fully taken into account in numerical modeling only; nevertheless, it is possible to make simple analytic estimates.

We consider a host clump with mass M_{DM}, radius R_{DM}, and some distribution of smaller clumps inside it. These small clumps move in the common gravitational potential with the velocity dispersion $\sim V_{\mathrm{DM}} \simeq (GM_{\mathrm{DM}}/R_{\mathrm{DM}})^{1/2}$. By tidally interacting with the environment, a small clump is 'shaken' and its internal energy (the kinetic energy of dark matter particles) increases.

We first consider the interaction of the clump with another, target clump when the first flies with an impact parameter l by the target. The target clump is characterized by a mass M', a radius R', the core radius $R'_c = x'_c R$, and some internal density distribution.

The internal energy increase of a clump with mass M during one collision in the momentum approximation [197] is expressed as

$$\Delta E = \frac{1}{2}\int \mathrm{d}^3 r\, \rho_{\mathrm{int}}(r)(v_x - \tilde{v}_x)^2, \qquad (82)$$

where v_x is the dark matter particle velocity increase along the x axis and $\tilde{v}_x$ is the same quantity for the center of mass of the clumps. It is easy to obtain

$$v_x = \frac{2GM'}{v_{\mathrm{rel}}R'}\,g(y), \qquad (83)$$

where $y = l/R'$, v_{rel} is the relative velocity of the clumps, and the function $g(y)$ depends on their internal structure [39]. The rate of the internal energy increase due to collisions of the selected clump with all other clumps is determined as

$$\dot{E} = \int 2\pi l v_{\mathrm{rel}}\,\mathrm{d}l \int \mathrm{d}M'\psi(M', t)\,\Delta E, \qquad (84)$$

assuming that the mass function $\psi(M', t)$ inside the host clump is known.

As another process that can be responsible for tidal destruction, we consider clump interaction with the common gravitational potential of the host clump. The energy increase per unit mass at a distance r from the barycenter of the selected small clump over the time of one periastron passage (if the orbit can be treated as elliptical) is [197]

$$\langle E_{\mathrm{p}}\rangle = \frac{GM_{\mathrm{DM}}}{R_{\mathrm{DM}}^3}\,r^2\left(\frac{R_{\mathrm{DM}}}{R_{\mathrm{p}}}\right)^{\beta}\chi_{\mathrm{ecc}}(e)\,A(\omega\tau), \qquad (85)$$

where e is the orbital eccentricity, R_{p} is the periastron distance, the function χ_{ecc} is presented in [197], and the

adiabatic correction is $A(x) = (1 + x^2)^{-\gamma}$, $\gamma \simeq 2.5-3.0$. The clump energy increase over one period $T_{\rm orb}$ has the form $\Delta E = \int \langle E_{\rm p} \rangle \, \rho_{\rm int}(r) \, {\rm d}^3 r$, and the energy rate increase is

$$\dot{E} = \frac{2\Delta E}{T_{\rm orb}} \,. \tag{86}$$

As shown in Section 6.3, clumps are tidally destroyed with a high probability, and the survival probability of each clump is $\xi \ll 1$. During the rest lifetime, the surviving clumps are surrounded by other clumps with the mass function $\psi(M', t)$. When the host clump is destroyed, the selected small-scale clump under consideration turns out to be inside a clump with a larger mass and with a small-scale clump distribution $\psi(M', t)$, but with a longer time t. The characteristic formation time of the minimal host clump is close to $t_{\rm f}$, and the destruction time can be much longer than $t_{\rm f}$. The energy increase rate due to both mentioned processes is given by the sum of (84) and (86).

Above, we sketched the ideas of more precise calculations, which were carried out by extracting individual processes from the general complex picture of tidal destructions. However, real processes are so chaotic that it is worth using a simplified approach by assuming that for a clump with mass M and radius R, after the typical gravitational impact, the internal energy increases by the value

$$\Delta E \sim \frac{4\pi}{3} \, G \rho_{\rm DM} M R^2 \,, \tag{87}$$

where $\rho_{\rm DM}$ is the mean density of the host clump.

6.3 Hierarchical clustering taking destructions into account

The process of transition of a clump from one host clump to another occurs almost continuously in time until the last host clump is formed, in which tidal destructions become ineffective. The survival probability of the clump is defined as the fraction of clumps with mass M that survived tidal destructions during the hierarchical clustering. The first host clump mostly contributes to the tidal destruction of the selected clump, especially if their densities are similar. With the dynamical effects in the Press–Schechter theory taken into account, the distribution function of clumps that avoided destruction was calculated in [83] as

$$\xi \, \frac{{\rm d}M}{M} \, {\rm d}\nu \simeq \frac{\nu \, {\rm d}\nu}{\sqrt{2\pi}} \exp\left(-\frac{\nu^2}{2} \right) f_1 \, \frac{{\rm d} \log \sigma_{\rm eq}(M)}{{\rm d}M} \, {\rm d}M \,, \tag{88}$$

where $f_1 \simeq 0.2-0.3$.

Qualitatively, the first factor ν in (88) corresponds to the fact that the clumps that were formed from high peaks (with higher values of ν) are more resistive to the destruction processes than those formed from low peaks (with smaller ν). After integrating (88) over ν, we obtain

$$\xi_{\rm int} \, \frac{{\rm d}M}{M} \simeq 0.02(n+3) \, \frac{{\rm d}M}{M} \,. \tag{89}$$

The effective power-law exponent in (89) is $n = -3(1 + 2\partial \ln \sigma_{\rm eq}(M)/\partial \ln M)$, which very weakly depends on M. Equation (89) assumes that for the typical n, only a small fraction of clumps (about 0.1–0.5%) survive the hierarchical tidal destruction in each logarithmic mass interval $\Delta \ln M \sim 1$. It should be noted that the physical meaning of the survived clump mass function $\xi \, {\rm d}M/M$ is different from that of free clumps described by the Press–Schechter formula $\partial F/\partial M$.

Substellar-mass clump formation was studied in numerical simulations in [44, 77]. The form of the differential clump number density $n(M) \, {\rm d}M \propto {\rm d}M/M^2$ turns out to be close to that obtained for large clumps with masses $M \geqslant 10^6 M_\odot$. The simple law, M^{-1}, of mass function (89) is in good agreement with the results of numerical simulation in [77], up to a normalization coefficient of the order of unity. Good agreement when extrapolating our calculations to the data of numerical modeling of large clumps with $M \geqslant 10^6 M_\odot$ [43] must also be noted.

At later times, mass function (89) is transformed due to tidal interactions with stars of the Galaxy; these processes are considered in Section 7.

7. Destruction of clumps in the Galaxy

The problem of the mechanisms and efficiency of destruction of substructures in galaxies was previously discussed in [198], and for large (galactic scale) dark matter subhalos, it was addressed later in many analytic and numerical studies. Similar studies of small-scale clumps started only recently. Clumps with distribution function (88) joined the Galaxy at the time of its formation, and later these clumps lost mass and were partially or fully destroyed due to tidal interactions with stars or with the collective field of the disc.

In many papers (see, e.g. [43, 48]), a simplified criterion of the clump tidal destruction was used. Namely, a clump is assumed to be destroyed if its total internal energy increase $\sum (\Delta E)_j$ after several disc crossings (or tidal interactions with stars) becomes of the same order as the initial clump binding energy $|E|$, i.e.,

$$\sum_j (\Delta E)_j \sim |E| \,, \tag{90}$$

where the summation is made over successive tidal interaction events. This criterion is valid at the early stages of hierarchical clustering in the clump formation epoch, because the clump density profile formation and tidal impacts occur in one epoch, and the clumps in which the density profiles have not yet been formed and which have no cores are mostly being destroyed. In the case of clump destruction in the Galaxy in later epochs, the gradual mass loss in each of the tidal interactions [199–201] should be taken into account; in particular, this was noted for small-scale clumps in [40, 202, 203].

Condition (40) implies that the clump has lost most of its mass. This simple criterion is useful in calculations if only the main mass loss is of interest. However, to calculate dark matter particle annihilation, it is important to know what the clump remnant is, because the surviving clump cores produce approximately the same annihilation signal as the original clumps. The main difficulty in exactly solving the problem is taking the mass loss in the inner regions of clumps into account during their complicated dynamical restructuring immediately after the tidal impacts.

7.1 Clump destruction by the disc field

We consider clumps that move in orbits in the galactic halo and cross its stellar disc. The Galaxy disc has the surface density

$$\sigma_{\rm s}(r) = \frac{M_{\rm d}}{2\pi r_0^2} \exp\left(-\frac{r}{r_0} \right) , \tag{91}$$

where $M_{\rm d} = 8 \times 10^{10} M_\odot$ and $r_0 = 4.5$ kpc. The increase in the dark matter particle energy relative to the clump center energy after a single disc crossing is expressed as [204]

$$\delta E = \frac{4 g_{\rm m}^2 (\Delta z)^2 m}{v_{z\rm c}^2} A(a)\,, \tag{92}$$

where Δz is the vertical distance (across the disc plane) from the dark matter particle to the clump center, $v_{z\rm c}$ is the vertical clump velocity relative to the disc at the disc crossing time, $A(a)$ is the adiabatic correction, and the gravitational acceleration above the disc is $g_{\rm m}(r) = 2\pi G \sigma_{\rm s}(r)$. The factor $A(a)$ in (92) describes the effect of adiabatic protection from slowly varying tidal forces [205]. This correction is given by the extra factor $A(a)$ in the energy increase calculated in the momentum approximation. In [199], the formula $A(a) = (1 + a^2)^{-3/2}$ was proposed. Here, the adiabatic parameter is determined as $a = \omega \tau_{\rm d}$, where ω is the orbital frequency of the dark matter particle on the clump and $\tau_{\rm d} \simeq H_{\rm d}/v_{z\rm c}$ is the effective duration (fly-by time) of the gravitational impact produced by a disc with the half-thickness $H_{\rm d}$. For the tidal interaction of the clump with bulge and halo stars, the gravitational collision duration is estimated as $\tau_{\rm s} \sim l/v_{\rm rel}$, where l is the impact parameter and $v_{\rm rel}$ is the relative velocity of the clump and the star.

The internal density profile $\rho_{\rm int}(r)$ and the particle energy distribution function in the clump $f_{\rm cl}(\varepsilon)$ (per unit mass) in the model with an isotropic velocity dispersion are related by the integral formula [206]

$$\rho_{\rm int}(r) = 2^{5/2}\pi \int_{\psi(r)}^{0} \sqrt{\varepsilon - \psi(r)}\, f_{\rm cl}(\varepsilon)\, {\rm d}\varepsilon\,. \tag{93}$$

The simplest models assume the isothermal distribution function $f_{\rm cl}(\varepsilon) \propto \exp(-2\varepsilon)$.

The energy addition $\delta\varepsilon$ from the tidal interaction leads to the particle stripping off with energies in the range $-\delta\varepsilon < \varepsilon < 0$, and the clump density change at a radius r is expressed as [83]

$$\delta\rho(r) = 2^{5/2}\pi \int_{-\delta\varepsilon}^{0} \sqrt{\varepsilon - \psi(r)}\, f_{\rm cl}(\varepsilon)\, {\rm d}\varepsilon\,. \tag{94}$$

The adiabatic correction enters this expression via $\delta\varepsilon$ in the lower integration limit, according to formula (92). The clump mass loss in a single disc crossing event is

$$\delta M = -4\pi \int_0^R r^2\, \delta\rho(r)\, {\rm d}r\,. \tag{95}$$

We use NFW profile (45) in the Galaxy halo. The relation between the density profile $\rho_{\rm h}(r)$ and the distribution function is given by the same formula (93) with the substitution $f_{\rm cl} \to F(\varepsilon)$. The distribution function $F(\varepsilon)$ for halo profile (45) is presented in [207], and the clump orbit distribution in the halo can be expressed in terms of it [83]. Further, by choosing the time interval ΔT much longer than the clump orbital period T_t but shorter than the Galaxy age t_0, $T_t \ll \Delta T \ll t_0$, it is possible to determine the mean mass loss by the selected clump due to tidal impacts in successive disc crossings:

$$\frac{1}{M}\left(\frac{{\rm d}M}{{\rm d}t}\right)_{\rm d} \simeq \frac{1}{\Delta T} \sum \left(\frac{\delta M}{M}\right)_{\rm d}\,, \tag{96}$$

where the summation ranges all successive disc crossing points.

The destruction of large subhalos with masses $M \geqslant 10^7 M_\odot$ in their disc crossings was studied in numerical simulations in [208]. Large clumps, unlike the small-scale clumps considered here, can significantly affect the stellar kinematics in the disc.

7.2 Clump destruction by stars

The calculation of the clump internal energy increase during a single stellar encounter with an impact parameter l is similar to the one carried out in Section 6.2 (the star plays the role of the host clump with the mass $M' = m_*$). By integrating (82) over the clump volume with the density profile $\rho_{\rm int}(r)$ from (32), for $l > R$, we obtain the internal energy increase in the form

$$\Delta E = \frac{2(3-\beta)}{3(5-\beta)} \frac{G^2 M R^2 m_*^2}{v_{\rm rel}^2 l^4}\,. \tag{97}$$

The opposite case $l < R$ is considered, for example, in [39]. It is easy to verify that the minimal increase in the internal energy occurs during a tangential stellar fly-by at the distance $l \simeq R$ from the clump center.

Depending on the impact parameter value, for different stellar collisions of the clump, there can be two modes of clump destruction [43]: (1) in one stellar encounter or (2) after many tidal interactions with stars. The clump internal energy increase rate is

$$\dot{E} = 2\pi \int \Delta E(l)\, n_* v_{\rm rel}\, l\, {\rm d}l\,, \tag{98}$$

where n_* is the stellar number density.

Using the results in [209], we approximate the radial stellar number density in the bulge at distances $r = (1-3)$ kpc as

$$n_{\rm b*}(r) = \frac{\rho_{\rm b}}{m_*} \exp\left[-\left(\frac{r}{r_{\rm b}}\right)^{1,6}\right], \tag{99}$$

where $\rho_{\rm b} = 8 M_\odot\ {\rm pc}^{-3}$, $m_* = 0.4 M_\odot$, and $r_{\rm b} = 1$ kpc. The corresponding stellar number density in the halo at $r > 3$ kpc outside the galactic disc can be approximated as [210]

$$n_{{\rm halo},*}(r) = \frac{\rho_{\rm halo}}{m_*} \left(\frac{r_\odot}{r}\right)^3, \tag{100}$$

where $\rho_{\rm halo} = 1.4 \times 10^{-5} M_\odot\ {\rm pc}^{-3}$ and $r_\odot = 8.5$ kpc. In these calculations, we neglect the dark matter halo non-sphericity and the stellar halo flatness [210].

The rough criterion in (90), which characterizes the clump mass loss, yields the clump survival probability as shown in Fig. 7. We see that the disc makes the largest contribution to the clump destruction, and there are almost no clumps in the Galaxy bulge. The sharp jump in the figure is due to the use of the bulge model with a sharp boundary.

Clump destruction by stars was also studied in [47, 203, 211], by numerical calculations in particular.

In some papers, the disc is regarded as a collection of stars, and the tidal interaction is calculated in the same way as when the clump flies through an infinite medium consisting of point-like masses (stars), but during the finite time intervals that the clump crosses the disc. It can be shown that in typical

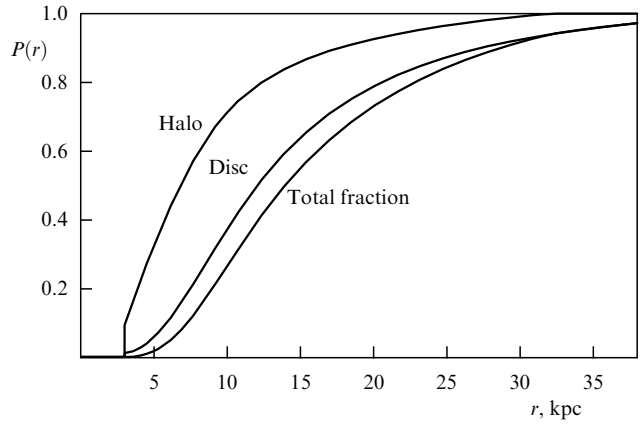

Figure 7. Fraction of clumps with the mass $M = 10^{-6} M_\odot$ and the peak value $\nu = 2$ that were not tidally destroyed by the galactic disc, P_d, by galactic halo stars, P_halo, and the total fraction, $P_\mathrm{tot} = P_\mathrm{halo} P_\mathrm{d}$, as functions of the distance to the galactic center. The rough clump tidal destruction criterion (90) was used. The cut-off at $r < 3$ kpc is due to complete clump disintegration in the galactic bulge.

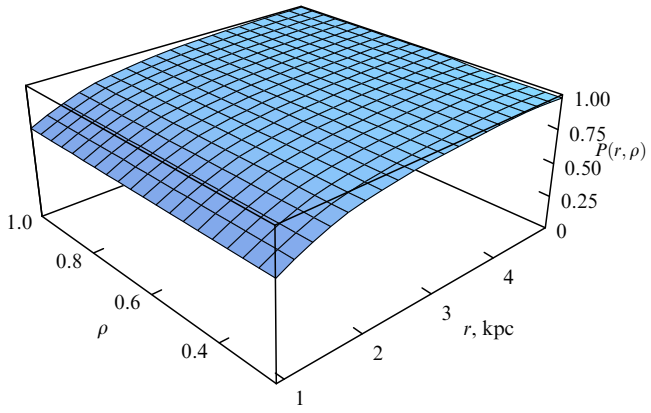

Figure 8. Survival probability $P(r, \rho)$ as a function of the distance to the galactic center r and the mean inner clump density for $x_\mathrm{c} = R_\mathrm{c}/R = 0.05$. This yields the normalized fraction of clumps in the halo that escaped tidal destructions by the disc and halo. The clump density is normalized to 7.3×10^{-23} g cm^{-3} of clumps with the mass $M = 10^{-6} M_\odot$ that originated from 2σ peaks, assuming a power-law perturbation spectrum with the exponent $n_\mathrm{s} = 1$.

cases, the collective field of the disc gives the leading contribution to the clump destruction. The clump internal energy increase in one disc crossing due to interaction with individual stars relative to that caused by the gravitational impact with the collective disc field is

$$\frac{\Delta E^\mathrm{stars}}{\Delta E^\mathrm{disc}} \sim 0.6 \left(\frac{R}{0.015 \text{ pc}} \right)^{-2} \exp\left(\frac{r - r_\odot}{r_0} \right) \cos\theta \,, \quad (101)$$

where $r_0 = 4.5$ kpc and $R = 0.015$ pc is the radius of an Earth-mass clump, $3 \times 10^{-6} M_\odot$, formed from the peak with $\nu = 2$ in the case of the density perturbation spectrum with $n_\mathrm{s} = 0.96$. That is, only for clumps with minimal masses at $r \geqslant r_\odot$ are both contributions comparable, and when the mass and, accordingly, the radius of the clump increase, the collective field effect becomes dominant.

7.3 Remnants of clumps

We now turn to the question of clump core survival. We describe the clump destruction processes in the disc, bulge, and halo by a single equation for the clump mass loss,

$$\frac{\mathrm{d}M}{\mathrm{d}t} = \left(\frac{\mathrm{d}M}{\mathrm{d}t} \right)_\mathrm{d} + \left(\frac{\mathrm{d}M}{\mathrm{d}t} \right)_\mathrm{s} . \quad (102)$$

In [82], Eqn (102) was solved numerically for the time $t_0 - t_\mathrm{G}$ elapsed from the galaxy formation epoch until the present instant t_0.

The dark matter particle annihilation is the most important observational signature of the clumps. The dominance of the central core in the clump annihilation signal is critical for clumps with sufficiently sharp density profiles. Namely, the central core dominates in the annihilation signal in the clump with power-law density profile (32) if $\beta > 3/2$ and $x_\mathrm{c} = R_\mathrm{c}/R \ll 1$. More precisely, the value $\dot{N} \propto \int_{r_0}^{r} 4\pi r'^2 \, \mathrm{d}r' \rho_\mathrm{int}^2(r')$ is virtually independent of r if $r \gg r_0$. As a result, the annihilation luminosity of a clump with a nearly isothermal density profile ($\beta \simeq 2$) is almost constant during the tidal stripping process until the clump radius becomes as small as the core radius. In other words, in the modern Galaxy, the clump remnants stripped by tidal interactions with $x_\mathrm{c} < \mu(t_0) \ll 1$, where $\mu(t) = M(t)/M_\mathrm{i}$, $t_0 \simeq 10^{10}$ yrs is the age of the Galaxy, satisfy Eqn (102) and have the same annihilation luminosity as their progenitors at $\mu = 1$.

Using the solution of Eqn (102), we can calculate the clump survival probability P over the age of the Galaxy. Calculations show that for clumps with $x_\mathrm{c} \ll 0.05$, $P \sim 1$ everywhere (see Fig. 8). Clumps from outer regions can even fly inside the bulge. This means that the clump remnants mostly survive in the tidal interactions in the Galaxy. The probability decreases, $P < 1$, near the galactic center for clumps with $x_\mathrm{c} > 0.05$. This can be easily understood because as $x_\mathrm{c} \to 1$, we return to the old clump destruction criterion (90) with the corresponding survival probabilities [43, 48].

The aggregate surviving clump fraction, taking early hierarchical clustering destructions and destructions in the halo into account, is shown in Fig. 9 as a function of the clump mass and the perturbation spectral exponent for typical clumps produced by perturbations with $\nu = 2$.

The clump mass function in the Galaxy is modified due to the gradual mass loss by the clumps. According to the theoretical model in [39] and numerical modeling in [77], the differential number density of small-scale clumps in the comoving frame is $n(M)\,\mathrm{d}M \propto \mathrm{d}M/M^2$. This distribution is shown in Fig. 10 by the solid line. In the case of flattening of small-scale perturbations with $M < M_\mathrm{min}$, the additional factor $\exp\left[-(M/M_\mathrm{min})^{2/3}\right]$ arises, which is responsible for the perturbation decay at low masses M.

Due to the disc and stellar destructions, the initial (cosmological) clump mass function is transformed into the final (modern) clump mass function, which is shown in Fig. 10 for two distances from the galactic center. The calculations assume the clump core radius to be very small, such that all clump remnant masses are available. With a finite core radius, the mass function would be cut off at the clump core masses. It can be seen from Fig. 10 that the clump remnants exist for $\sim M_\mathrm{min}$. In the bulge near the galactic center, the clump remnants are more numerous because of intensive clump destructions in high-density stellar regions relative to the rarefied stellar halo. The leading contribution to the forma-

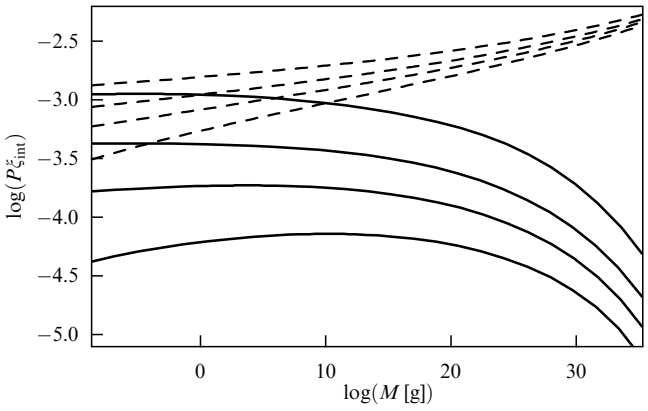

Figure 9. Initial fraction (dashed curves) and the present-day fraction (solid curves) of the surviving dark matter clumps in a unit logarithmic mass interval $\delta M \sim M$ as a function of the clump mass M for the spectral exponents $n_s = 0.949$, 0.963, 0.977, and 1.000 (from top down).

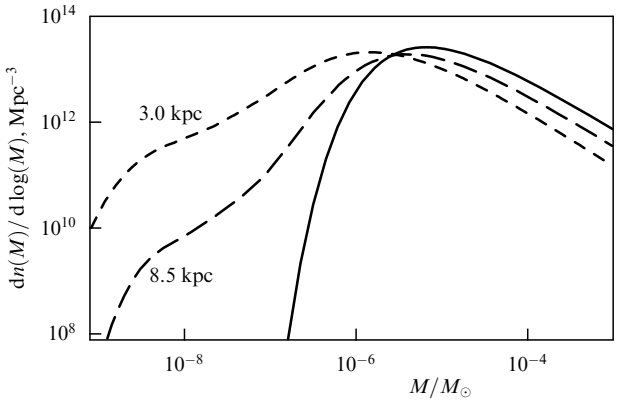

Figure 10. The modified clump remnant mass function calculated numerically at the galactocentric distances 3.0 and 8.5 kpc. The solid curve shows the initial mass function.

tion of the mass function tail at low masses is provided by clumps with orbits close to the disc, which suffer stronger destructions. Another important point is the total destruction of clumps whose orbits lie entirely within the bulge. Nevertheless, the clump number density in the bulge is nonzero because most of the clumps have orbits extending beyond the bulge. These 'transit' clumps spend only a small fraction of their orbital periods inside the bulge and thus avoid total destruction.

8. Particle annihilation in clumps

Particle–antiparticle interaction can result in their annihilation, accompanied by the rest-mass energy transformation into other particles. For example, if photons are present among the annihilation products, they can in principle be registered by gamma telescopes, which provides information on dark matter particles. Unlike charged particles, photons are not deflected by cosmic magnetic fields; therefore, they should be registered from the directions to the sources, which can facilitate their identification.

The local annihilation rate is proportional to the particle number density squared, and is therefore higher in the central parts of dark matter halos. Generally, if any inhomogneities are present, $\overline{\rho^2} > (\bar{\rho})^2$; therefore, inhomogeneities always enhance annihilation signals. An inhomogeneity can appear as a smooth central density increase [for example, according to profiles (45) and (46)] or as a collection of chaotic small-scale inhomogeneities on top of this smooth regular density peak. Dark matter in the smooth profile is frequently referred to as the diffuse halo component. The particle number density in clumps is much higher than in the diffuse component, and hence the clump annihilation signal in many models dominates over the diffuse signal (usually except in the most dense central core of the halo), even if the clumps contain a small fraction of the total halo dark matter.

Recently, an excess of gamma rays from the central parts of the Galaxy has been reported, which cannot be explained by the radiation of ordinary astrophysical sources and can be related to dark matter annihilation. However, these results have not been reliably confirmed, primarily due to uncertain astrophysical backgrounds. Nevertheless, even an upper bound on the annihilation radiation flux can provide invaluable information on possible dark matter particle parameters. As far as we know, the idea to use such gamma-ray background constraints was first proposed in [212].

The annihilation rate (the number of annihilated particles, which is equal to twice the number of annihilation events) in a single clump is given by

$$\dot{N}_{\mathrm{cl}} = 4\pi \int_0^{\infty} r^2\,\mathrm{d}r\,\rho_{\mathrm{int}}^2(r)\,m^{-2}\langle\sigma_{\mathrm{ann}}v\rangle = \frac{3}{4\pi}\,\frac{\langle\sigma_{\mathrm{ann}}v\rangle}{m^2}\,\frac{M^2}{R^3}\,S\,, \tag{103}$$

where v is the relative velocity of two dark matter particles with mass m, and σ_{ann} is the annihilation cross section. The function S in (103) depends on the dark matter distribution inside the clump. In particular, $S = 1$ in the simplest case where the clump has a constant density, i.e., $\rho_{\mathrm{int}}(r) = \mathrm{const}$ at $r \leqslant R$ and $\rho_{\mathrm{int}}(r) = 0$ at $r > R$, and $S \simeq 4/(9x_{\mathrm{c}})$ for the isothermal profile $\rho \propto r^{-2}$ with a small core, $x_{\mathrm{c}} \ll 1$.

In expression (103), Majorana particles are assumed, i.e., those that are identical to their own antiparticles, $\bar{\chi} = \chi$, as is the case for neutralinos. For Dirac particles, ρ_{int} would mean the sum of densities of particles and antiparticles, and the extra factor 1/2 should be incorporated in (103).

8.1 Cross sections and spectra of neutralino annihilation products

The quantity $\langle\sigma_{\mathrm{ann}}v\rangle$ can be expressed in terms of the relative velocity v of two dark matter particles as

$$\langle\sigma_{\mathrm{ann}}v\rangle = a + bv^2 + cv^4 + \ldots\,, \tag{104}$$

where α includes only the s-wave contribution, while b includes contributions from both the s- and p-waves. For small velocities $v \ll 1$, only the first term can be considered.

In the expression for $\langle\sigma_{\mathrm{ann}}v\rangle$, averaging over the thermal particle distribution is assumed. As a rule, thermal distributions are realized in both the early Universe and the typical dark matter halo models. Therefore, the expression for $\langle\sigma_{\mathrm{ann}}v\rangle$ is sufficiently universal, and it can be used to connect particle creation in the early cosmological epochs and their annihilation rate in the modern Universe. In the case of a strongly anisotropic or nonthermal distribution function, an extra factor of the order of unity appears in the expression for $\langle\sigma_{\mathrm{ann}}v\rangle$.

The most probable annihilation channel is into quarks with the subsequent hadronization of the reaction products

and the formation of an almost universal continuum annihilation product spectrum. Gamma quanta in this case are generated basically due to neutral pi-meson decays:

$$\mathrm{x}+\bar{\mathrm{x}}\to\pi^0+\mathrm{all}\,,\quad \pi^0\to\gamma+\gamma\,,$$

where 'all' means all other annihilation products. The fragmentation function $\mathrm{d}N_i/\mathrm{d}x$ for the differential particle number density of type i generated in a single annihilation event with the energy $E=xm$ is calculated in [213, 214], where various analytic approximations are also presented. An important role in the formation of the annihilation spectrum can be played by the intrinsic bremssrahlung radiation from charged particles that can be present among the intermediate annihilation products. In specific calculations, the DarkSUSY computer package [215] is frequently used, which allows obtaining the cross sections and spectra of the annihilation products in different channels under different assumptions about the supersymmetry model parameters.

Some supersymmetry models allow neutralino annihilation predominantly into the lepton channel. These models were especially invoked in connection with data of the PAMELA (Payload for Antimatter Matter Exploration and Light-nuclei in Astrophysics) experiment, which is discussed in detail in Section 9.

In most of the simplest models, the main annihilation signal is generated in the continuum, and spectral lines, even if they are present, are suppressed. Nevertheless, the generation of lines, even if of a very low intensity, is possible by neutralino annihilation into two photons, into a photon and a Z^0 boson, or into a photon and a Higgs boson. The discovery of a narrow spectral line would provide the unique opportunity to extract the signal from the background, because the usual astrophysical sources can hardly generate high-energy spectral lines. In this connection, of great interest have been the recent claims of observations of a possible line at 130 GeV by the Fermi-LAT (Fermi Large Area Telescope) instrument from the central region of the Galaxy [216, 217], as well as a possible indication of the presence of this line from galaxy clusters [218] and from some unidentified Fermi-LAT sources (see a detailed discussion of these issues, which are highly relevant today, in [219]). Intriguing is the $\simeq 1.5^\circ$ shift of the maximum of the emission from the dynamical center of the Galaxy. However, the shift is difficult to accommodate in the annihilation scenario, because the off-center dark matter cusp location would lead to its tidal destruction in interactions with the baryonic matter cusp [220].

We now consider the Sommerfeld enhancement effect, which can significantly boost the particle annihilation cross section at low relative particle velocities, especially inside clumps. The Sommerfeld enhancement became very relevant and widely discussed in connection with the PAMELA experimental results considered in Section 9 because this effect only proved to be capable of producing the required boost factor of several orders of magnitude if clumps with masses $\geqslant 10^5 M_\odot$ are present in the Galaxy. That the Sommerfeld enhancement plays an important role in the annihilation of supersymmetric dark matter particles was first argued in [221, 222]. The Sommerfeld enhancement, which is an increase in the annihilation cross section, is due to multiple exchanges of intermediate bosons between the annihilating particles. This exchange, which occurs according to ladder Feynman diagrams, corresponds to a certain distortion of the wave function of the annihilating particles due to the presence of an additional interaction potential in the Schrödinger equation [223]. For supersymmetric particles, it is important here that the neutralino belongs to a multiplet of states with close masses, between which coannihilation occurs. Therefore, for example, for a bino, which is a singlet, the Sommerfeld enhancement is absent. The Sommerfeld enhancement for superheavy neutralinos was considered in [181].

The Sommerfeld enhancement is most frequently modeled by the Yukawa potential $V(r)=-(\alpha/r)\exp(-m_V r)$, where m_V is the mass of the force-carrier particle. In the Coulomb limit $m_V\to 0$, the boost coefficient $\mathcal{R}$ (the ratio of the perturbative to the nonperturbative annihilation cross sections), which is determined by the relation $\langle\sigma v\rangle=\mathcal{R}\langle\sigma v\rangle_0$, has the form

$$\mathcal{R}=\frac{\pi\alpha}{\beta}\left[1-\exp\left(-\frac{\pi\alpha}{\beta}\right)\right]^{-1}, \tag{105}$$

where $\beta=v/c$. For small β, $\mathcal{R}\propto 1/v$. However, at very small β, of the order of 10^{-4} (in the model with particle masses around 1 TeV considered in [223]), saturation occurs, and no cross-section boost occurs upon a further velocity decrease. When changing the ratio between the masses of the dark matter particle and the interaction carrier particle, resonances appear in the annihilation cross section, in which the enhancement coefficient can be as high as $\sim 10^4-10^5$ [223]. In addition, as shown in [223], due to the Sommerfeld effect, the cross section of the neutralino annihilation into electron–positron pairs is of the same order of magnitude as the cross section of the annihilation into intermediate bosons, whereas in the absence of the Sommerfeld effect, the former cross section is suppressed by the factor $(m_\mathrm{e}/m)^2$.

The annihilation products can also be observed indirectly. For example, the synchrotron radiation of charged particles created in neutralino annihilations can explain the diffuse background radio emission observed by the ARCADE-2 (Absolute Radiometer for Cosmology, Astrophysics, and Diffuse Emission 2) experiment and by other detectors [224].

8.2 Determination of astrophysical backgrounds that are not connected with annihilation

In searches for dark matter particle annihilation, the complicated problem arises of extracting the signal from different backgrounds produced by cosmic rays and usual astrophysical sources. It is most difficult to determine the interstellar cosmic ray contribution, because the rays propagate far away from their sources and generate diffuse gamma-ray backgrounds when interacting with the interstellar gas and radiation field.

The observed fluxes of cosmic ray charged particles are compared with charge particle fluxes in the secondary generation model developed by Ginzburg and Syrovatsky [225, 226], and its modern version is conveniently realized in the GALPROP computer code [227]. This model is key in searching for different spectral anomalies that can suggest dark matter particle annihilation.

Presently, searches for dark matter particle annihilation are mainly carried out by Fermi Space Gamma-ray Observatory (the former Gamma-ray Large Area Space Telescope, GLAST), launched in 2008, and the LAT (Large Area Telescope) is the main instrument aboard this space gamma-ray observatory. In the GeV energy range, Fermi-LAT has a

resolution of about 1 degree, which corresponds to its point-spread function at a level of 68% [228]. Objects with a large angular size, observed by Fermi-LAT, cannot be considered point-like any more, and the telescope sees only part of their gamma-ray emission in each direction. Fermi-LAT enables detection of gamma-ray quanta with energies above 100 MeV and has the sensitivity $\Phi(E > 100\ \mathrm{MeV}) = 6.0 \times 10^{-9}\ \mathrm{cm^2\ s^{-1}}$ for point-like sources. Not all of the point-like sources observed have been identified, and some of them could be produced by annihilation of large dark matter clumps. Bounds on the number of clumps and their progenitor perturbation spectrum in different mass ranges were obtained in [153] by comparing the Fermi-LAT point-like sources and the calculated annihilation signal from clumps, both galactic and extragalactic. In addition, in [153], constraints from diffuse emission, reionization, and gravitational microlensing were considered. A comparison of the Fermi-LAT data with the annihilation signal from clumps calculated for a power-law dependence of the annihilation cross section on the relative particle velocity $\sigma_{\mathrm{ann}} \propto v^{-\beta}$ (taking the Coulomb enhancement into account), where β is a free parameter, was made in [72]; constraints on β and other parameters were obtained.

8.3 Parameterization of the annihilation signal

When calculating the annihilation signal, it is convenient to separate factors related to the dark matter particle properties from 'astrophysical' factors caused by dark matter distribution and clumping. The latter include, in particular, the character of dark matter clustering and the presence of clumps. Following [53], we write the observed flux from the direction ψ averaged over the solid angle $\Delta\Omega$ as

$$J_\gamma(E, \psi, \Delta\Omega) = 9.4 \times 10^{-11}\, \frac{\mathrm{d}S}{\mathrm{d}E}\, \langle J(\psi) \rangle_{\Delta\Omega}\,, \tag{106}$$

where

$$\frac{\mathrm{d}S}{\mathrm{d}E} = \left(\frac{100\ \mathrm{GeV}}{m}\right)^2 \sum_f \frac{\langle \sigma_f v \rangle}{10^{-26}\ \mathrm{cm^3\ s^{-1}}}\, \frac{\mathrm{d}N_\gamma^f}{\mathrm{d}E}\,, \tag{107}$$

$\mathrm{d}N_\gamma^f$ is the number of photons per single annihilation event (per pair of annihilating particles), and the astrophysical factor (in the direction ψ, averaged over the solid angle $\Delta\Omega$) is

$$\langle J(\psi) \rangle_{\Delta\Omega} = \frac{1}{8.5\ \mathrm{kpc}}\, \frac{1}{\Delta\Omega} \int \mathrm{d}\Omega' \int \mathrm{d}L \left(\frac{\rho(r)}{0.3\ \mathrm{GeV\ cm^{-3}}}\right)^2. \tag{108}$$

The integration is carried out along the line of sight. For Dirac particles, an extra factor 1/2 emerges in (106), and $\rho = \rho_+ + \rho_-$ denotes the total dark matter density (the sum of particles and antiparticles).

In the case of an ordinary (~ 100 GeV) neutralino, the generation rate of gamma-ray photons in a clump can be approximately represented as $2\eta_{\pi^0} \dot{N}_{\mathrm{cl}}$, where $\eta_{\pi^0} \sim 10$ is the multiplicity of neutral pions. Here, it is assumed that the neutralino annihilates to produce π^0 with subsequent decays $\pi^0 \to 2\gamma$. The cumulative flux at the angle ψ to the Galaxy center is

$$J_\gamma\left(E > \frac{m_{\pi^0}}{2}, \psi\right) = 1.9 \times 10^{-10} \left(\frac{m}{100\ \mathrm{eV}}\right)^{-2} \frac{\langle \sigma v \rangle}{10^{-26}\ \mathrm{cm^3\ s^{-1}}}\, \langle J(\psi) \rangle_{\Delta\Omega}\,. \tag{109}$$

The astrophysical factor for particle annihilation in clumps has the form

$$\langle J(\psi) \rangle_{\Delta\Omega} = \int \mathrm{d}\xi_{\mathrm{cl}} \left(\frac{\rho_{\mathrm{cl}}}{0.3\ \mathrm{G\,cm^{-3}}}\right) \int_{\mathrm{l.o.s.}} \frac{\mathrm{d}L}{8.5\ \mathrm{kpc}} \left(\frac{\rho_{\mathrm{h}}(r)}{0.3\ \mathrm{GeV\,s^{-3}}}\right), \tag{110}$$

where ξ_{cl} is assumed to include the survival probability P calculated in Section 7.3, and l.o.s. means that the integration is performed along the line of sight.

8.4 Enhancement of the annihilation signal

Annihilation signal enhancement is often referred to as the boost factor. As a rule, the enhancement is considered relative to the model in which the Galaxy halo or another dark matter object does not contain small-scale substructures. For example, a boost factor of 10 is required in the ordinary neutralino annihilation model to explain the gamma-ray excess observed by EGRET (Energetic Gamma Ray Experiment Telescope) [229]. The boost factor in the direction ψ is defined as

$$B(\psi) = \frac{J^{\mathrm{cl}}(\psi) + J^{\mathrm{hom}}(\psi)}{J^{\mathrm{hom}}(\psi)}\,, \tag{111}$$

where $J^{\mathrm{hom}}(\psi)$ is the signal from nonclumped dark matter in the halo. For $\langle \sigma_{\mathrm{ann}} v \rangle = \mathrm{const}$, the enhancement η does not depend on the annihilation cross section and is determined by dark matter clumping only.

To calculate the total signal integrated over all directions, instead of $\Delta\Omega^{-1} \int \mathrm{d}\Omega'$, integration over angles is performed:

$$\int_0^\pi \mathrm{d}\zeta \sin\zeta \int_0^{2\pi} \mathrm{d}\phi \ldots\,, \tag{112}$$

where ζ is the angle between the line of sight and the direction to the Galaxy center. The distance l between the clump and the Galaxy center can be expressed through r (in this case, it is simply the distance from Earth to the clump), $r_\odot$ (the distance from the Sun to the galactic center), and ζ as $l(\zeta, r) = (r^2 + r_\odot^2 - 2rr_\odot \cos\zeta)^{1/2}$. The maximum distance from the Sun to the outer halo boundary in the direction ζ is $r_{\max}(\zeta) = (R_{\mathrm{h}}^2 - r_\odot^2 \sin^2\zeta)^{1/2}$, where $R_{\mathrm{h}} \sim 100$ kpc is the virial radius of the galactic halo and $r_\odot = 8.5$ kpc.

Under the assumption that the clump number density is proportional to the halo density, i.e., $n_{\mathrm{cl}}(l) = \xi \rho_{\mathrm{DM}}(l)/M$, the boost factor can be conveniently estimated as

$$B \approx 1 + \xi S(x_{\mathrm{c}}, \beta)\, \frac{\bar{\rho}_{\mathrm{int}}}{\tilde{\rho}_{\mathrm{DM}}}\,, \tag{113}$$

where $\tilde{\rho}_{\mathrm{DM}} = 4.26 \times 10^{-23}$ g cm^{-3}. For example, for the parameters $\beta \simeq 1.8$, $x_{\mathrm{c}} \simeq 0.05$, $S(x_{\mathrm{c}}, \beta) \simeq 5$, $\tilde{\rho}_{\mathrm{h}} \sim \rho_{\mathrm{DM}}(r_\odot) \sim 0.3$ GeV cm^{-3}, $\bar{\rho}_{\mathrm{int}} \sim 2 \times 10^{-22}$ g cm^{-3}, and $\xi \sim \sim 0.001$, Eqn (113) yields the numerical estimate $B \sim 3$. A close estimate, $B \sim 4$, for annihilation in the galactic halo was recently obtained in [51].

8.5 Annihilation in galaxies and galaxy clusters

Properties of dark matter particles and their clustering can be constrained by comparing the results of model calculations with observations of the gamma-ray background and point-

like gamma-ray sources. Fermi-LAT annihilation limits in galaxy clusters were analyzed in [230–234]. As noted in [235], observations of the Virgo, Fornax, and Coma clusters likely demonstrate some gamma-ray excess, which can be explained by dark matter particle annihilation. Fermi-LAT annihilation limits in the Milky Way were studied, for example, in [236–238]. A direct comparison of signals from the Galaxy and galaxy clusters was performed in [239] (see Fig. 7 and Section 5.3 there) and [240] (see Table 1 there). The signal of unseen galactic satellites was analyzed in [241].

The tightest bounds on the annihilation cross section are presently obtained from dwarf galactic satellite spheroids [230]. The Fermi-LAT limits for these objects are already close to the thermal cross section $\langle\sigma v\rangle \simeq 3\times 10^{-26}$ cm^3 s^{-1}, even in the most conservative case without any boost factor [242, 243]. In the case of the thermal cross section, dark matter particles were produced in the early Universe in an amount just sufficient to explain the dark matter abundance. Dwarf galaxies seem to be very suitable for dark matter particle annihilation searches, insofar as they contain a small amount of gas and have a low star formation rate. For this reason, the cosmic rays must produce a low gamma-ray background. On the other hand, dwarf spheroids exhibit high mass–luminosity ratios ($\sim 10^3 M_\odot/L_\odot$), i.e., they contain a relatively large amount of dark matter. Using the bound $\langle\sigma v\rangle < 3\times 10^{-26}$ cm^3 s^{-1}, the Fermi-LAT collaboration [242] inferred a minimum possible dark matter particle mass in the hadronic and leptonic annihilation channels, ≈ 27 GeV and ≈ 37 GeV respectively. An alternative analysis of signals and backgrounds [243] suggests that the Fermi-LAT observations of dwarf spheroids exclude, at the 95% level, dark matter particles with masses below 40 GeV in the hadronic annihilation channel. In addition, searches for an annihilation signal from globular clusters are being carried out [244]. Some of these objects may be remnants of small satellite galaxies stripped off by tidal forces and may contain an appreciable amount of dark matter. However, no signals from globular clusters have been detected yet.

Details of annihilation signal calculations from dwarf galaxies can be found in the papers cited above; here, as an example, we calculate the signals from the Milky Way and galaxy clusters in detail. In the Virgo cluster, the distance from Earth to the cluster center exceeds the virial cluster radius. Therefore, the integration over L in (108) is bounded by the values $L_{\max,\min}(\psi) = \pm(R^2 - r_{\rm V}^2\sin^2\psi)^{1/2} + r_{\rm V}\cos\psi$ and $\sin\psi < \sin\psi_{\max} = R/r_{\rm V}$, where the distance to the Virgo center is $r_{\rm V} = 16.5$ Mpc [245]. Assuming the NFW profile for the Virgo cluster, we have $a^{\rm V} = 0.58$ Mpc and $\rho_0^{\rm V} = 1.0\times 10^5 M_\odot$ kpc^{-3}.

We first compare the signals from the diffusive dark matter component without clumps. Within the angular size $\delta\psi = 1^\circ$, signals from the Virgo cluster center and from the galactic center are calculated to be

$$\left\langle J(\psi)\right\rangle_{\Delta\Omega}(\text{Milky Way}) \simeq 1.4\times 10^3\,, \tag{114}$$

$$\left\langle J(\psi)\right\rangle_{\Delta\Omega}(\text{Virgo}) \simeq 5\times 10^{-2}\,. \tag{115}$$

Signals integrated over the solid angle $\Delta\Omega = 4\pi$ for the Milky Way and $\Delta\Omega = 2\pi(1-\cos\psi_{\max}) = 0.067$ for the Virgo cluster are

$$\left\langle J(\psi)\right\rangle_{\Delta\Omega}(\text{Milky Way}) \simeq 3\,, \tag{116}$$

$$\left\langle J(\psi)\right\rangle_{\Delta\Omega}(\text{Virgo}) \simeq 9\times 10^{-4}\,. \tag{117}$$

The centers of both the Galaxy and Virgo clusters are fairly poor targets for annihilation signal searches due to a strong background contamination from astrophysical sources, including the cosmic-ray induced gamma-ray flux. In addition, the M87 galaxy with an active nucleus is close to the Virgo center. Chances of detecting the annihilation signal crucially depend on the assumed signal-to-noise ratio, and hence the above estimates remain very uncertain.

We next consider the possible contribution from small-scale clumps with distribution (88). The integration over the clump distribution in Eqn (110) can be performed analytically,

$$\left\langle J(\psi)\right\rangle_{\Delta\Omega} \simeq 7.01\left(\frac{S(x_{\rm c},\beta)}{S(0.01;1.8)}\right)\left(\frac{\sigma_{\rm eq}(M_{\min},n_{\rm s})}{\sigma_{\rm eq}(10^{-6}M_\odot;0.963)}\right)^3 \times\frac{1}{\Delta\Omega}\int {\rm d}\Omega'\int\frac{{\rm d}L\rho(r)}{0.3\ \text{GeV cm}^{-3}}\,, \tag{118}$$

where $S(0.01;1.8)\simeq 14.5$ and $\sigma_{\rm eq}(10^{-6}M_\odot;0.963)\simeq 8.76\times 10^{-3}$. With the contribution from the clump taken into account, for the central parts of the Galaxy and Virgo clusters with the angular size 1°, we find

$$\left\langle J(\psi)\right\rangle_{\Delta\Omega}(\text{Milky Way}) \simeq 1.4\times 10^2\,, \tag{119}$$

$$\left\langle J(\psi)\right\rangle_{\Delta\Omega}(\text{Virgo}) \simeq 13\,, \tag{120}$$

and for signals integrated over angles, we obtain

$$\left\langle J(\psi)\right\rangle_{\Delta\Omega}(\text{Milky Way}) \simeq 15\,, \tag{121}$$

$$\left\langle J(\psi)\right\rangle_{\Delta\Omega}(\text{Virgo}) \simeq 1.3\,. \tag{122}$$

Hence, clump boosting in the Virgo cluster can reach three orders of magnitude.

It is also interesting to compare the signals from clumps with $M_{\min}\sim 10^{-6}M_\odot$ generated from the standard power-law perturbation spectrum normalized to the WMAP data and from diffusive dark matter in the Galaxy. We assume that the clump distribution function due to hierarchical clustering has form (88) and that the clump survival probability can be taken from the results in Section 7.3. The results of these calculations are presented in Fig. 11. It is seen that depending on the angle, the enhancement of the signal due to dark matter clumping reaches 2.5 orders of magnitude.

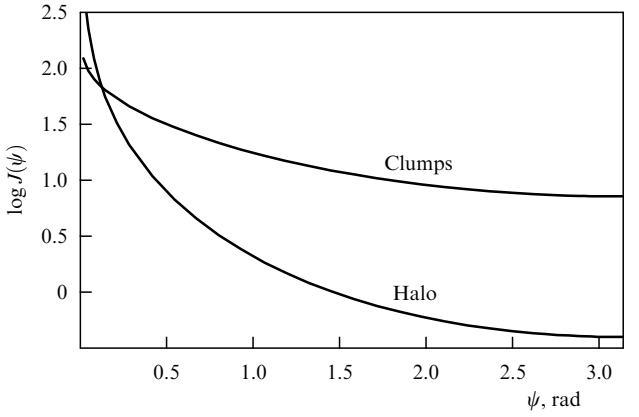

Figure 11. The astrophysical factor $J(\psi)$ (in conventional units) as a function of the angle ψ from the line of sight and the direction to the Galactic center.

8.6 Anisotropy of annihilation signals

The annihilation signal is usually calculated by assuming a spherically symmetric galactic halo. In this case, the anisotropy of the annihilation gamma-ray remission can only be due to the noncentral galactic location of the Sun. Nevertheless, as demonstrated in [63], the halo nonsphericity can be fundamentally important for the annihilation emission. According to observations, axes of the galactic ellipsoidal halo differ by less than 10%–20%; however, a higher difference, up to a factor of two, cannot be excluded [246, 247]. This leads to an order-of-magnitude uncertainty in the predicted amplitude of the annihilation signal from the center and anticenter of the Galaxy [63].

The anisotropy relative to the galactic plane was discussed in [48, 203]. The tidal destruction of a clump is generally anisotropic and depends on the clump orbital inclination to the disc plane. Accordingly, dark matter annihilation in the halo (in surviving clumps) should also be anisotropic. In Fig. 12, the annihilation signal calculated in [48] is shown in the galactic plane and in the normal plane passing through the Galaxy center. For comparison, Fig. 12 also shows the signal from a spherically symmetric halo without clumps. This signal is the same in both planes, and hence it can in principle be extracted from observations. The difference between signals in two orthogonal planes measured for the same angle ζ to the center can be viewed as a measure of the anisotropy. We consider the quantity $\delta = (I_2 - I_1)/I_1$. It takes the maximum value $\delta \simeq 0.09$ for $\zeta \simeq 39^\circ$, which, however, is significantly higher than the Fermi-LAT resolution.

The annihilation signal from the galactic center depends on the dark matter central density profile. If there is a density cusp [176], a bright source in the center of the Galaxy should be present. However, this cusp in the diffuse dark matter distribution can be smeared out by baryons [248]. Small-scale clumps are destroyed more efficiently inside the stellar bulge around the galactic center. It is also possible to observe dark 'gamma-ray' circles in other galaxies, appearing due to the absence of clumps in the central regions of these galaxies [203].

The intrinsic anisotropy of the annihilation signal due to dark matter clustering should also be noted. The corresponding angular spectrum of the annihilation signal fluctuations at small angular scales is related to the dark matter clump spectrum [249–252]. In principle, nearby clumps can appear in gamma-ray observations as point-like sources [63, 72]. Some evidence of small-scale anisotropy produced by a population of point-like sources was found in Fermi-LAT observations [253], and it is too early to rule out that some of these sources can be dark matter clumps. Another secondary source of annihilation anisotropy can be the dipole anisotropy due to the motion of the Sun in the Galaxy; this effect can easily be observed.

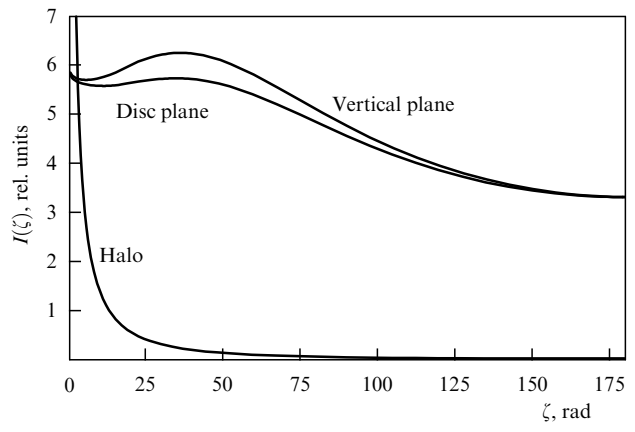

Figure 12. The annihilation signal in the galactic disc plane and in the plane normal to the galactic disc as a function of the angle ζ between the line of sight and the direction to the galactic center. For comparison, the annihilation signal from the galactic halo without clumps is also shown.

8.7 Annihilation in ultradense clumps

The annihilation signal enhancement in clumps, on the one hand, increases the chances of dark matter annihilation detection; on the other hand, in some models, the enhancement turns out to be so strong that the predicted signal exceeds the observed background constraints, which imposes constraints on the parameters of dark matter particles and clustering.

We first discuss standard neutralinos with a mass of the order of the electroweak scale, which are generated according to the thermal scenario. We show that if not all of these particles were assembled into superdense clumps at the RD stage, the annihilation flux would exceed the observed background, and therefore this scenario (superheavy clumps from standard neutralinos) is ruled out. We choose the parameters that minimize the annihilation flux and assume the mean neutralino density in the clumps to be the minimal value corresponding to the clump formation at the end of the RD stage, $\bar{\rho}_{\rm int} = 178\rho_{\rm eq}$. Then the minimal gamma-ray flux averaged over angles is

$$J_\gamma^{\rm tot} = 4.3\langle\sigma v\rangle_{26}\, m_{100}^{-2} \ \ {\rm cm}^{-2}\ {\rm s}^{-1}\ {\rm sr}^{-1}\,, \qquad (123)$$

where m_{100} is the neutralino mass m in units of 100 GeV and $\langle\sigma v\rangle_{26} = \langle\sigma v\rangle/(10^{-26}\ {\rm cm}^3\ {\rm s}^{-1})$. Integral flux (123) is larger than the observed one by five orders of magnitude. However, the decrease in the number of clumps being formed due to the initial nonsphericity of perturbations turns out to be sufficient to reconcile the theory with observations [131]. It is possible to consider more massive neutralinos and to choose the minimum possible annihilation cross section [177] for the strongly suppressed s-wave annihilation channel, $\langle\sigma v\rangle = 1.7\times10^{-30} m_{100}^{-2}\ {\rm cm}^3\ {\rm s}^{-1}$. However, for the dark matter clump fraction $f_{\rm cl} \ll 1$, the annihilation signal would still be several orders of magnitude higher than the diffusive flux measured by EGRET and Fermi-LAT. This excess was noted in [177] in the particular case of clumps in the form of 'neutralino stars'.

The annihilation upper bounds (in the model of usual neutralinos) were used in [152, 158, 159] to conclude that the mass fraction of clumps in dark matter is much less than units. A similar conclusion was reached in [149] from the analysis of the early annihilation effect on the recombination process from CMB measurements. In the standard model of the neutralino ($\sim$ 100 GeV), the simple possibility of avoiding the discrepancy with a strong annihilation signal is provided by a small amplitude of perturbations, when no superheavy clumps can be formed. In particular, the absence of observed point-like gamma-ray sources was used in [103] to conclude that in the e^+e^--annihilation epoch, the amplitude of the perturbation entering the horizon was less than 10^{-3}. In [159], additional constraints on clumps were derived from the analysis of dark matter annihilation effects on the reionization of the Universe.

We now discuss the annihilation of superheavy particles in superdense clumps. Although the existence of superheavy

dark matter particles is theoretically admissible and well justified, their detection appears to be a very difficult problem. Indeed, the creation of such particles in accelerator experiments and their direct registration go far beyond the existing capabilities and those planned for the foreseeable future. The annihilation rate of such heavy particles depends on mass approximately as $\dot{N}_{\rm ann} \propto m^{-4}$. Because the background radiation, such as cosmic rays from astrophysical sources and the diffusive flux of gamma-ray photons, decreases with energy only as $1/E^{\alpha}$ with $\alpha \leqslant 3$ as the particle mass increases, the indirect detection of dark matter particles seems to be more and more an impossible task. One possibility enabling us to overcome this difficulty is the formation of a superdense core in clumps [255]. In [255], with the aim of explaining the origin of ultra-high-energy cosmic rays [256], superheavy dark matter particle annihilation in the dense central part of the clumps was discussed as an alternative to scenarios with superheavy particle decays [20, 21].

Another possibility is the annihilation in superdense clumps considered in [164, 181]. In sufficiently dense clumps, relaxation due to two-particle gravitational scattering can initiate the 'gravothermal catastrophe', and the clump density profile can be transformed into the isothermal profile $\rho \propto r^{-2}$ with a very small core radius. This is the case for the superheavy bino. Due to the density increase, dark matter annihilation is substantially enhanced. Unlike the bino, the vino and Higgsino are strongly coupled to the thermal plasma; therefore, no gravothermal catastrophe is occurs. Virial velocities of dark matter particles in superdense clumps are very small, which leads to the Sommerfeld enhancement of the annihilation rate of the vino and Higgsino. With this effect taken into account, the annihilation flux from superheavy dark matter particles was shown in [164, 181] to be at the observable level for all types of superheavy neutralinos.

Neutralino annihilation in superdense clumps around cosmic string loops was analyzed in [141]. The formation of such clumps was discussed in Section 3.5. A comparison of the calculated signal with Fermi-LAT data treated as the upper bound allows constraining the properties of cosmic strings and dark matter particles.

To conclude this section, we mention three other possible annihilation effects. Charged particles created by the particle annihilation in clumps can form additional inhomogeneities in interstellar magnetic fields, which can affect the cosmic ray diffusion coefficient [257]. The annihilation of neutralinos at redshifts $z \sim 10-30$ can substantially change the thermal balance of gas in the Universe, whereas this process without clumps is ineffective [258]. The annihilation in clumps can also affect the reionization history of the Universe [259].

9. Charge particle fluxes in PAMELA, ATIC, and other experiments

9.1 Observational data

As early as 1994, the balloon experiment HEAT (High Energy Antimatter Telescope) discovered a small excess of e^+ in the energy range 6–10 GeV, possibly suggesting dark matter particle annihilation. The excess of e^+ with the same energies was detected in the AMS-01 (Alpha Magnetic Spectrometer 01) experiment. This positron excess in the energy range 6–10 GeV was not confirmed by later experiments, but 'instead' new results suggested an excess of positrons at higher energies.

The PAMELA detector aboard the Russian satellite *Resurs-DK1* for studying the charged component of cosmic rays was launched into orbit on 15 June 2006. It can register positrons and protons in cosmic rays. The 2008 data release revealed an excess of e^+ in the energy range 10–60 GeV, where no solar modulation is expected. In a short time, this excess was reliably confirmed up to 90 GeV.

Over 850 days of observations from July 2006 to December 2008, the PAMELA detector registered $\simeq 1500$ antiprotons with energies from 60 to 180 GeV; this antiproton flux, up to model and experimental errors, is in good correspondence with the secondary generation of protons in cosmic ray interactions with the interstellar gas [260]. In particular, the PAMELA data reproduce the expected shape of the spectrum with a maximum at about 2 GeV. Thus, the excess of e^+ observed by PAMELA is not associated with the excess of $\bar{p}$.

The ATIC (Advanced Thin Ionization Calorimeter) balloon-borne experiments revealed the presence of an excess of electrons with energies 300–800 GeV, with a sharp cutoff at higher energies. Because electrons can easily be absorbed by the interstellar gas, such an excess can be produced only by a nearby source.

The results of measurements in different experiments significantly differ in some energy ranges. The flux of electrons measured by ATIC somewhat exceeds the standard model prediction, while the PAMELA measurements below 625 GeV are in agreement with the standard generation model [261]. The PAMELA data look somewhat more convincing because the PAMELA detector provides good magnetic separation of particles, has a larger volume calorimeter than ATIC, and is equipped with a neutron detector; in addition, the PAMELA data are visually scrutinized at the final stage.

PAMELA also provided the best constraints to date on antideuterium and antihelium fluxes, except in some energy ranges where more stringent bounds are provided by the BESS (Balloon-borne Experiment with a Superconducting Spectrometer) experiment. These constraints are interesting from the dark matter standpoint, because $d\bar{d}$ and $He\overline{He}$ pairs can, with some probability, be created by dark matter particle annihilation.

Recently, in the AMS-02 experiment aboard the International Space Station, an excess of the positron fraction at energies up to 350 GeV was reported [262], and thus the PAMELA results were confirmed and extended toward higher energies.

9.2 Annihilation scenario and its problems

Dark matter particle annihilation provides an explanation for the observed e^+ excess in the PAMELA experiment. This hypothesis has been widely discussed, suggesting indirect registration of dark matter. Discussions of the annihilating dark matter in connection with the PAMELA data made these studies very topical and stimulated detailed investigations of the neutralino models, accurate calculations of the annihilation cross sections and the annihilation product spectra, etc. Models with decaying dark matter particles have also been discussed. It should be noted from the very beginning that simpler astrophysical explanations have been immediately suggested (see Section 9.3), and the dark matter model is presently not considered to be the lead one.

Explaining the PAMELA results by the annihilation of ordinary neutralinos generated by the thermal mechanism requires invoking a significant boost factor, because the annihilation cross section is determined by the neutralino generation model, and this cross section is too small to create the observed charged particle flow. As we know, high-density clumps can increase the boost factor [263]. Because the particle velocity dispersion in the clumps is low, the Sommerfeld enhancement and radiation corrections, which can increase the annihilation cross section by several orders of magnitude, are equally important. They can increase gamma-ray and positron fluxes due to annihilation [264]. Earlier explanations of the HEAT results by neutralino annihilation also required a boost factor of the order of 30.

Thus, apparently, neutralino annihilation can easily explain the PAMELA data. However, this scenario runs into a serious difficulty. As noted in Section 9.1, PAMELA observations do not show the antiproton excess, whereas typical annihilation models predict the generation of positron and antiproton excesses simultaneously. This problem is pertinent to the boost factor produced due to both clumps and other possible sources, i.e., the problem is inherent to the annihilation scenario in general, irrespective of the clump models.

Another major problem arises in relation to the Fermi-LAT flux bounds from dwarf galaxies and galaxy clusters. These bounds strongly constrain or (in the most typical models) exclude the PAMELA data interpretation of the neutralino annihilation. The point is that for the positron flux registered by PAMELA to be produced, the annihilation cross section must be so large that the gamma-ray signal from dwarf galaxies and clusters should necessarily be observed. This problem is to a great extent dependent on the annihilating particle model, namely, on the predominant annihilation channels. In the simplest case of the usual neutralino, the dark matter annihilation model as an explanation of the PAMELA results can already be excluded due to the absence of antiprotons and disagreement with Fermi-LAT observations, but hypothetical variants with suppressed annihilation into gamma-ray photons and antiprotons are still possible. For example, the annihilation into lepton channels only was considered in [265], and a model invoking the dark sector was studied in [266].

A sufficiently good correspondence of the calculations with the ATIC data can be obtained in the annihilation model for Kaluza–Klein particles with masses ≈ 620 GeV [267]. It can be supposed that ATIC discovered a sufficiently close clump in which annihilation occurs [268], or the annihilation is under way in a dense density peak around an intermediate-mass black hole. We note, however, that dark matter particles of one sort are unlikely to simultaneously explain both PAMELA and ATIC results, although attempts have been made to develop a unified model.

9.3 Alternative explanations

The simplest explanation of the positron excess observed by PAMELA is provided by the assumption that cosmic ray propagation and secondary generation models are incomplete [269]. The corrected model in [269] corresponds to the observed positron excess if the additional positrons result from the annihilation of vino-like neutralinos with masses of 180 GeV, which were produced in the early Universe by a nonthermal mechanism [270].

The e^+ excess registered by PAMELA together with the absence of the corresponding antiproton excess can be explained by the generation of electrons and positrons in pulsars. However, these models encounter difficulties because reproducing different parts of the e^+ spectrum requires assuming different pulsar model parameters; in other words, to reach agreement with observations, the summation of fluxes from several pulsars with different properties is required. A similar explanation of the ATIC results also meets with difficulties, since the electron spectra generated by neutron stars and microquasars are different from the observed one.

An interesting solution can be found in the framework of the model of generation of an e^+ excess in the processes $\pi^+ \to e^+ + \ldots$ during flares on dwarf main-sequence stars, which are the most numerous stars in the Galaxy. It is known from astronomical observations that low-mass stars have quite unsteady photospheres, in which very powerful flares, much more powerful than solar flares, occur. Calculations [271, 272] indicate that stellar flares could reproduce the observed e^+ excess. This model is attractive because it does not postulate any new phenomena and is based only on the known astrophysical processes.

Finally, a simple and elegant solution of the e^+ excess problem is given in [273, 274], where the secondary positrons are assumed to be generated and accelerated by cosmic-ray sources themselves. This model successfully reproduces the observed e^+ spectrum with no antiproton excess and well-studied energy ranges. A concern may arise only with nuclei and antiprotons at very high energies (> 100 GeV), although the reality of such concerns has not been confirmed by specific calculations, and the observational accuracy at these energies is still poor.

10. Other possible observational manifestations of clumps

10.1 Direct detection of dark matter particles. Ministreams

The probability that Earth is now inside a dark matter clump is estimated to be from 0.0001% [211] to 0.1% [68], depending on the clump mass and the assumed perturbation spectrum. If such a rare event is indeed taking place now, the probability of direct and indirect dark matter particle detection should be much higher [68].

It was concluded in [40, 203] that almost all clumps in the Galaxy are tidally disrupted in interactions with stars. As shown in Section 7.3, for a significant fraction of clumps, tidal interactions with stars indeed lead to stripping off their outer layers, i.e., to a substantial mass loss, but this does not imply total clump destruction, because the clump cores can survive [83, 263]. The stripped mass is transformed into 'ministreams' of dark matter [40, 203, 263]. For the direct experimental detection of dark matter, the ministreams are interesting because dark matter particles in them move along several different discrete directions corresponding to the progenitor clumps before the destruction. According to [211], presently some $10^2 - 10^4$ ministreams may be crossing Earth. The ministream formation and evolution during clump destructions by stars were also addressed in [41]. Dark matter in the streams spreads in the space like a broad tail, and therefore the probability of a ministream colliding with Earth is much higher than that of the entire clump crossing.

10.2 Registration of clumps by gravitational wave detectors

It has been argued in some papers that the planned gravitational-wave detectors like LISA (Laser Interferometer Space Antenna) can measure small variations of the gravitational field caused by nearby flying compact objects. LISA was supposed to search for PBHs [275], asteroids [276], or compact dark matter objects of an unknown nature [277]. Clumps can be included into this list. A detectable signal is produced by the tidal gravitational force, which changes the interferometer arm length and, accordingly, causes a phase shift. Using LISA, it is possible to search for compact objects in the mass range $10^{16} \leqslant M \leqslant 10^{20}$ g according to [275], or $10^{14} \leqslant M \leqslant 10^{20}$ g according to the calculations in [277]. The signal is expected to consist of single pulses with the characteristic frequency near the low-frequency sensitivity limit of LISA, and the event rate of these signals can be ~ 1 per decade, assuming that such objects constitute most of the dark matter. In the usual scenario, the clump fraction is only 1%–10% of all dark matter and hence the clump detection rate should be 1–2 orders of magnitude lower. In addition, the radii of such clumps, as a rule, are much larger than the LISA arm length $L \simeq 5 \times 10^{11}$cm, and therefore the tidal force amplitude is smaller. Hence, the detection of standard clumps by LISA seems to be unlikely.

The next generation of gravitational-wave detectors opens more possibilities (see [275] for more details). Superdense clumps, due to their compactness, easily meet the condition $R < L \simeq 5 \times 10^{11}$ cm in the mass range $10^{14} \leqslant M \leqslant 10^{20}$ g, and these clumps, if they exist, can be detected by LISA.

10.3 Neutralino stars and microlensing

To explain microlensing events observed in the Galaxy halo, Gurevich, Zybin, and Sirota were the first to propose the model of gravitationally bound noncompact clumps (self-gravitating clumps) with a mass $\sim (10^{-2}-10^{0})\, M_{\odot}$ consisting of weakly interacting dark matter particles [166]. Because the main dark matter particle candidate was the neutralino, such clumps were dubbed 'neutralino stars'. It was also noted that the neutralino stars produce a very strong annihilation signal even for a very large core size, $R_{\rm c} \sim 0.1R$, and in order to not violate the observational limits, the neutralino was postulated to annihilate with a small cross section in a p-wave. Neutralino stars with a very small core radius complying with the annihilation limits were then considered in [177]; it was shown that in this case, too, the annihilation signal is expected to significantly exceed the observational constraints, even by assuming the minimum possible annihilation cross section available in supersymmetry models.

The criterion for clump formation from adiabatic density perturbations with PBH constraints taken into account was improved in [88]. In particular, it was shown there that to make compact gravitational lenses, the clumps should be produced as early as at the radiation-dominated stage (although at its end). Hence, neutralino stars can be qualified as the superdense clumps considered in Section 3.3. For their formation, a maximum should exist in the standard power-law density perturbation cosmological spectrum. The results in Section 3.3 suggest that in the case of adiabatic perturbations, the existence of such a maximum would inevitably lead to the creation of a significant number of PBHs with masses $\sim 10^{5} M_{\odot}$ at the RD stage.

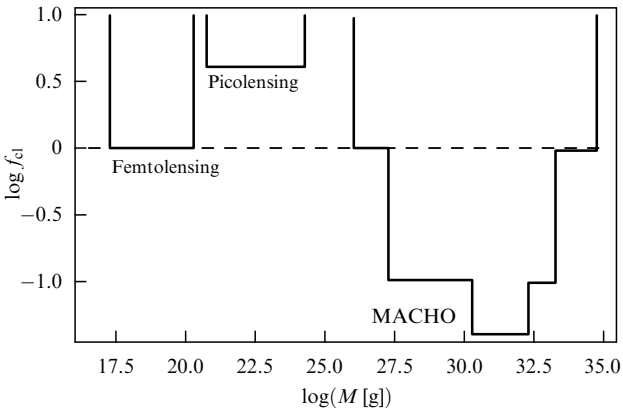

Figure 13. Upper bounds on the relative clumped dark matter fraction $f_{\rm cl} = \Omega_{\rm cl}/\Omega_m$ from microlensing MACHO observations, as well as from femto- and picolensing observations of cosmic gamma-ray bursts [118].

The authors of [166] also noted that the baryonic core, if formed inside clumps, should modify the microlensing light curve by the clumps. In later studies [157, 159, 160], the clumps were also regarded as microlensing objects. Two types of clumps were analyzed in [157]: minihalos around PBHs and clumps without central PBHs. The substellar mass clumps in other galaxies can in theory be detected in gravitational lensing observations of quasars in these galaxies [279, 280]. Gravitational lensing of type-Ia supernovae also yielded constraints on the dark matter clumping [281]. Some clumping constraints can also be derived from pulsar timing observations, because the gravitational field of clumps located near the line of sight must produce delays in the time of arrival of periodical signals from pulsars [282]. Figure 13 displays microlensing constraints obtained by the MACHO (Massive Astrophysical Compact Halo Object) project, as well as femto- and picolensing constraints obtained from gamma-ray burst observations [118].

We note that the problem of microlenses has become less relevant now because all microlensing events can be explained by stars. However, the microlensing observations can be used to impose upper bounds on the number of PBHs and superdense dark matter clumps in some mass ranges, thus constraining the primordial perturbation spectrum on the corresponding scales.

As shown in [166], a clump can serve as a gravitational lens and explain the observed microlensing events only if its radius is less than 10 times the Einstein radius for this object. This condition implies very stringent constraints on the nonlinear compression of clumps. It turned out [88] that clumps can be gravitational lenses only for the high PBH formation threshold $\delta_{\rm th} > 0.5$ obtained in the model of the critical gravitational collapse, whereas the clump model of microlensing objects is excluded for lower values of $\delta_{\rm th}$.

10.4 Baryons in clumps

Dissipative processes in the baryonic gas inside dark matter clumps were studied in [166] and in the clumps around PBHs, in [283]. It was concluded in [166] that the settling of baryons toward the clump center causes the dark matter density to increase as well, which enhances its particle annihilation rate. In addition, it was noted that the baryonic core modifies the microlensing light curve of the clumps.

However, we note that it is hard to expect a noticeable baryonic flux toward substellar-mass clumps, because virial

temperatures in the clumps are too low for the effective baryon cooling to operate. Additionally, due to Compton scattering of CMB photons, baryons cannot be accelerated to virial velocities in clumps; therefore, it is hard to expect the enhancement of baryonic accretion at high redshifts. In particular, baryons from almost homogeneous low-density surroundings can be accreting onto the clumps around PBHs [283].

Sufficiently heavy clumps with masses $\sim 10^5 - 10^6 M_\odot$ that form potential wells into which baryons are collected to form early population-III stars were studied in [157, 284]. These stars can be responsible for the reionization of the Universe at $z \geqslant 10$. The annihilation of dark matter particles captured by a star in the central part of a clump can significantly contribute to the energy balance of the star and affect its evolution [285, 286].

Clumps with masses $M \geqslant 10^{-3} M_\odot$ can be manifested in 21 cm atomic hydrogen line observations by producing temperature fluctuations in the baryonic gas.

10.5 Motion of clumps on the celestial sphere

If a signal from nearby clumps is detected, it will be possible to measure the proper motions of the clump in the sky, as in astrometric observations of nearby stars [69, 72, 288, 289]. However, as shown in [289], the possibility of observing proper motions is limited by annihilation gamma-ray constraints from the galactic center and other sources. The nearby clumps and their proper motion can be detected only for a large annihilation cross section. But then the signal from other sources would violate the existing observational bounds. However, we note that this effect is strongly dependent on the sensitivity and angular resolution of gamma-ray telescopes, and the calculation in [289] was done using the Fermi-LAT parameters. Clearly, with instrumental and observational progress, it may be possible to simultaneously measure the proper motion of clumps in the sky and annihilation signals from different sources.

11. Conclusion

Small-scale dark matter clumps are interesting to study for several reasons.

These early formed objects can be the densest dark matter objects in the Universe; therefore, the dark matter annihilation in these small-scale clumps can be very effective. The clumps enable the annihilation signal to be enhanced in galactic halos by several times or even orders of magnitude. High densities like those in the clumps can appear only in the central dark matter cusps in galactic centers, if the density growth is not stopped at some large radius, or in cusps around central black holes. Thus, the clumps, if they exist, open additional prospects for indirect dark matter detection via the annihilation channel, which may help solve one of the biggest modern mysteries: the nature of dark matter.

If a signal from annihilating dark matter is detected, it will be possible to study the dark matter distribution in greater detail and to obtain information on the primordial perturbation spectrum, from which different-scale structures were formed, as well as to clarify the physics (shape of the scalar field potential or other characteristics) of the inflation stage, when these perturbations were generated. The clumps could shed light on the small scales (in comparison with the galactic scale) at which the perturbations were generated at the end of the inflation stage.

Annihilation in clumps could change the thermal balance in the gas in the pre-galactic epoch and dramatically affect the evolution of the first stars and hence the chemical evolution of matter in galaxies, the number of PBHs, etc.

The physics of dark matter clumps is also concerned with the problem of small-scale perturbation generation, gravitational dynamics, dark matter particle properties, and the annihilation product effects in the clumps; it is a truly interdisciplinary field of modern astrophysics and cosmology.

This paper was supported by the Ministry of Education and Science of the Russian Federation (contract No. 8525) and by grants OFN-17 from the RAS and NSh-871.2012.2.

References

1. Gorbunov D S, Rubakov V A *Introduction to the Theory of the Early Universe*: *Hot Big Bang Theory* (Singapore: World Scientific, 2011) [Translated from Russian: *Vvedenie v Teoriyu Rannei Vselennoi*: *Teoriya Goryachego Bol'shogo Vzryva* (Moscow: LKI, 2008)]
2. Gorbunov D S, Rubakov V A *Introduction to the Theory of the Early Universe*: *Cosmological Perturbations and Inflationary Theory* (Singapore: World Scientific, 2011) [Translated from Russian: *Vvedenie v Teoriyu Rannei Vselennoi*: *Kosmologicheskie Vozmushcheniya. Inflyatsionnaya Teoriya* (Moscow: KRASAND, 2010)]
3. Weinberg S *Cosmology* (Oxford: Oxford Univ. Press, 2008) [Translated into Russian: *Kosmologiya* (Moscow: URSS, 2012)]
4. Lukash V N, Mikheeva E V *Fizicheskaya Kosmologiya* (Physical Cosmology) (Moscow: Fizmatlit, 2010)
5. Bisnovatyi-Kogan G S *Relyativistskaya Astrofizika i Fizicheskaya Kosmologiya* (Relativistic Astrophysics and Physical Cosmology) (Moscow: KRASAND, 2011)
6. Lukash V N, Mikheeva E V, Malinovsky A M *Phys. Usp.* **54** 983 (2011) [*Usp. Fiz. Nauk* **181** 1017 (2011)]
7. Cherepashchuk A M *Phys. Usp.* **56** 509 (2013) [*Usp. Fiz. Nauk* **183** 535 (2013)]
8. Chernin A D *Phys. Usp.* **51** 253 (2008) [*Usp. Fiz. Nauk* **178** 267 (2008)]
9. Lukash V N, Rubakov V A *Phys. Usp.* **51** 283 (2008) [*Usp. Fiz. Nauk* **178** 301 (2008)]
10. Bolotin Yu L, Erokhin D A, Lemets O A *Phys. Usp.* **55** 876 (2012) [*Usp. Fiz. Nauk* **182** 941 (2012)]
11. Massey R et al. *Nature* **445** 286 (2007)
12. Ryabov V A, Tsarev V A, Tskhovrebov A M *Phys. Usp.* **51** 1091 (2008) [*Usp. Fiz. Nauk* **178** 1129 (2008)]
13. Jungman G, Kamionkowski M, Griest K *Phys. Rep.* **267** 195 (1996)
14. Troitsky S V *Phys. Usp.* **55** 72 (2012) [*Usp. Fiz. Nauk* **182** 77 (2012)]
15. Dodelson S, Widrow L M *Phys. Rev. Lett.* **72** 17 (1994); hep-ph/9303287
16. Gorbunov D, Khmelnitsky A, Rubakov V *JCAP* (10) 041 (2008)
17. Sikivie P, arXiv:0909.0949
18. Berezinsky V S *Phys. Lett. B* **261** 71 (1991)
19. Bolz M, Brandenburg A, Buchmüller W *Nucl. Phys. B* **606** 518 (2001); *Nucl. Phys. B* **790** 336 (2008)
20. Berezinsky V, Kachelrieß M, Vilenkin A *Phys. Rev. Lett.* **79** 4302 (1997)
21. Kuzmin V A, Rubakov V A *Phys. Atom. Nucl.* **61** 1028 (1998) [*Yad. Fiz.* **61** 1122 (1998)]
22. Berezinsky V, Kachelrieß M, Solberg M A *Phys. Rev. D* **78** 123535 (2008)
23. Dubrovich V K, Khlopov M Yu *JETP Lett.* **77** 335 (2003) [*Pis'ma Zh. Eksp. Teor. Fiz.* **77** 403 (2003)]
24. Ivanov P, Naselsky P, Novikov I *Phys. Rev. D* **50** 7173 (1994)
25. Lacki B C, Beacom J F *Astrophys. J. Lett.* **720** L67 (2010)
26. Add G et al. (ATLAS Collab.) *Phys. Lett. B* **716** 1 (2012)
27. Chatrchyan S et al. (CMS Collab.) *Phys. Lett. B* **716** 30 (2012)
28. Rubakov V A *Phys. Usp.* **55** 949 (2012) [*Usp. Fiz. Nauk* **182** 1017 (2012)]
29. Nath P, arXiv:1210.0520
30. Belli P et al. *Phys. Rev. D* **84** 055014 (2011)
31. Aalseth C E et al. (and CoGeNT Collab.) *Phys. Rev. Lett.* **107** 141301 (2011)

32. Hinshaw G et al., arXiv:1212.5226
33. Ade P A R et al. (Planck Collab.), arXiv:1303.5062
34. Lacey C, Cole S *Mon. Not. R. Astron. Soc.* **262** 627 (1993)
35. Schmid C, Schwarz D J, Widerin P *Phys. Rev. Lett.* **78** 791 (1997)
36. Wasserman I, in *Second Intern. A.D. Sakharov Conf. on Physics Moscow, Russia 20–24 May 1996* (Eds I M Dremin, A M Semikhatov) (Singapore: World Scientific, 1997) p. 191; astro-ph/9608012
37. Schmid C, Schwarz D J, Widerin P *Phys. Rev. D* **59** 043517 (1999)
38. Schwarz D J, Hofmann S *Nucl. Phys. B Proc. Suppl.* **87** 93 (2000)
39. Berezinsky V, Dokuchaev V, Eroshenko Y *Phys. Rev. D* **68** 103003 (2003)
40. Zhao H et al., astro-ph/0502049
41. Green A M, Hofmann S, Schwarz D J *JCAP* (08) 003 (2005)
42. Moore B et al., astro-ph/0502213
43. Berezinsky V, Dokuchaev V, Eroshenko Yu *Phys. Rev. D* **73** 063504 (2006)
44. Diemand J, Kuhlen M, Madau P *Astrophys. J.* **649** 1 (2006)
45. Green A M, Goodwin S P *Mon. Not. R. Astron. Soc.* **375** 1111 (2007)
46. Bertschinger E *Phys. Rev. D* **74** 063509 (2006)
47. Angus G W, Zhao H S *Mon. Not. R. Astron. Soc.* **375** 1146 (2007)
48. Berezinsky V S, Dokuchaev V I, Eroshenko Yu N *JCAP* (07) 011 (2007)
49. Giocoli C, Pieri L, Tormen G *Mon. Not. R. Astron. Soc.* **387** 689 (2008)
50. Kamionkowski M, Koushiappas S M, Kuhlen M *Phys. Rev. D* **81** 043532 (2010)
51. Anderhalden D, Diemand J *JCAP* (04) 009 (2013); arXiv:1302.0003
52. Koushiappas S M *New J. Phys.* **11** 105012 (2009)
53. Bergström L et al. *Phys. Rev. D* **59** 043506 (1999)
54. Schwarz D J *Ann. Physik* **12** 220 (2003)
55. Gurevich A V, Zybin K P *Sov. Phys. JETP* **67** 1 (1988) [*Zh. Eksp. Teor. Fiz.* **94** 3 (1988)]
56. Gurevich A V, Zybin K P *Sov. Phys. JETP* **67** 1957 (1988) [*Zh. Eksp. Teor. Fiz.* **94** (4) 5 (1988)]
57. Gurevich A V, Zybin K P *Phys. Usp.* **38** 687 (1995) [*Usp. Fiz. Nauk* **165** 723 (1995)]
58. Profumo S, Sigurdson K, Kamionkowski M *Phys. Rev. Lett.* **97** 031301 (2006)
59. Bringmann T *New J. Phys.* **11** 105027 (2009)
60. Weinberg S *Astrophys. J.* **168** 175 (1971)
61. Hofmann S, Schwarz D J, Stöcker H *Phys. Rev. D* **64** 083507 (2001)
62. Loeb A, Zaldarriaga M *Phys. Rev. D* **71** 103520 (2005)
63. Calcáneo-Roldán C, Moore B *Phys. Rev. D* **62** 123005 (2000)
64. Nieto D et al., arXiv:1110.4744
65. Zechlin H-S et al., arXiv:1110.6868
66. Pieri L, Branchini E, Hofmann S *Phys. Rev. Lett.* **95** 211301 (2005)
67. Oda T, Totani T, Nagashima M *Astrophys. J.* **633** L65 (2005)
68. Kamionkowski M, Koushiappas S M *Phys. Rev. D* **77** 103509 (2008)
69. Pieri L, Bertone G, Branchini E *Mon. Not. R. Astron. Soc.* **384** 1627 (2008)
70. Pinzke A, Pfrommer C, Bergström L *Phys. Rev. Lett.* **103** 181302 (2009)
71. Baxter E J et al. *Phys. Rev. D* **82** 123511 (2010)
72. Belotsky K M, Kirillov A A, Khlopov M Yu, arXiv:1212.6087
73. Zhang D *Mon. Not. R. Astron. Soc.* **418** 1850 (2011)
74. Yang Y, Yang G, Zong H *Phys. Rev. D* **87** 103525 (2013)
75. Anderhalden D, Diemand J *JCAP* (04) 009 (2013)
76. Bertschinger E *Astrophys. J. Suppl.* **58** (5) 39 (1985)
77. Diemand J, Moore B, Stadel J *Nature* **433** 389 (2005)
78. Mikheeva E, Doroshkevich A, Lukash V *Nuovo Cimento B* **122** 1393 (2007)
79. Doroshkevich A G, Lukash V N, Mikheeva E V *Phys. Usp.* **55** 3 (2012) [*Usp. Fiz. Nauk* **182** 3 (2012)]
80. Kaplinghat M *Phys. Rev. D* **72** 063510 (2005)
81. Strigari L E, Kaplinghat M, Bullock J S *Phys. Rev. D* **75** 061303(R) (2007)
82. Ishiyama T, Makino J, Ebisuzaki T *Astrophys. J. Lett.* **723** L195 (2010)
83. Berezinsky V, Dokuchaev V, Eroshenko Y *Phys. Rev. D* **77** 083519 (2008)
84. Kolb E W, Tkachev I I *Phys. Rev. Lett.* **71** 3051 (1993)
85. Kolb E W, Tkachev I I *Phys. Rev. D* **50** 769 (1994)
86. Khlopov M Yu , Sakharov A S, Sokoloff D D *Nucl. Phys. B Proc. Suppl.* **72** 105 (1999)
87. Khlopov M *J. Phys. Conf. Ser.* **66** 012032 (2007)
88. Dokuchaev V I, Eroshenko Yu N *JETP* **94** 1 (2002) [*Zh. Eksp. Teor. Fiz.* **121** 5 (2002)]
89. Bardeen J M et al. *Astrophys. J.* **304** 15 (1986)
90. Green A M, Hofmann S, Schwarz D J *Mon. Not. R. Astron. Soc.* **353** L23 (2004)
91. Press W H, Schechter P *Astrophys. J.* **187** 425 (1974)
92. Bond J R et al. *Astrophys. J.* **379** 440 (1991)
93. Bond J R, Myers S T *Astrophys. J. Suppl.* **103** 1 (1996)
94. Ade P A R et al. (Planck Collab.), arXiv:1303.5082
95. Green A M, Liddle A R *Phys. Rev. D* **56** 6166 (1997)
96. Starobinskii A A *JETP Lett.* **55** 489 (1992) [*Pis'ma Zh. Eksp. Teor. Fiz.* **55** 477 (1992)]
97. Blais D et al. *Phys. Rev. D* **67** 024024 (2003)
98. Yokoyama J *Astron. Astrophys.* **318** 673 (1997)
99. García-Bellido J, Linde A, Wands D *Phys. Rev. D* **54** 6040 (1996)
100. Cline J M, Crotty P, Lesgourgues J *JCAP* (09) 010 (2003)
101. Chung D J H et al. *Phys. Rev. D* **62** 043508 (2000)
102. Gelmini G B, Gondolo P *JCAP* (10) 002 (2008)
103. Scott P, Sivertsson S *Phys. Rev. Lett.* **103** 211301 (2009)
104. Kolb E W, Tkachev I I *Astrophys. J. Lett.* **460** L25 (1996)
105. Gott J R (III) *Astrophys. J.* **201** 296 (1975)
106. Gunn J E *Astrophys. J.* **218** 592 (1977)
107. Silk J, Stebbins A *Astrophys. J.* **411** 439 (1993)
108. Zel'dovich Ya B, Novikov I D *Sov. Astron.* **10** 602 (1967) [*Astron. Zh.* **43** 758 (1966)]
109. Hawking S *Mon. Not. R. Astron. Soc.* **152** 75 (1971)
110. Carr B J *Astrophys. J.* **201** 1 (1975)
111. Nadezhin D K, Novikov I D, Polnarev A G *Sov. Astron. J.* **22** 129 (1978) [*Astron. Zh.* **55** 216 (1978)]
112. Novikov I D et al. *Astron. Astrophys.* **80** 104 (1979)
113. Polnarev A G, Khlopov M Yu *Sov. Phys. Usp.* **28** 213 (1985) [*Usp. Fiz. Nauk* **145** 369 (1985)]
114. Bugaev E V, Konishchev K V *Phys. Rev. D* **65** 123005 (2002)
115. Choptuik M W *Phys. Rev. Lett.* **70** 9 (1993)
116. Niemeyer J C, Jedamzik K *Phys. Rev. D* **59** 124013 (1999)
117. Yokoyama J *Phys. Rev. D* **58** 107502 (1998)
118. Carr B J et al. *Phys. Rev. D* **81** 104019 (2010)
119. Sikivie P, Tkachev I I, Wang Y *Phys. Rev. D* **56** 1863 (1997)
120. Navarro J F, Frenk C S, White S D M *Astrophys. J.* **462** 563 (1996)
121. Fukushige T, Makino J *Astrophys. J. Lett.* **477** L9 (1997)
122. Moore B et al. *Astrophys. J.* **524** L19 (1999)
123. Jing Y P, Suto Y *Astrophys. J.* **529** L69 (2000)
124. White S D M, astro-ph/9410043
125. Knobel C, arXiv:1208.5931
126. Tolman R C *Phys. Rev.* **35** 875 (1930)
127. McCrea W H *Proc. R. Soc. London A* **206** 562 (1951)
128. Peebles P J E *The Large-Scale Structure of the Universe* (Princeton, N.J.: Princeton Univ. Press, 1980) [Translated into Russian: *Struktura Vselennoi v Bol'shikh Masshtabakh* (Moscow: Mir, 1983)]
129. Padmanabhan T, Subramanian K *Astrophys. J.* **417** 3 (1993)
130. Eisenstein D J, Loeb A *Astrophys. J.* **439** 520 (1995)
131. Berezinsky V S, Dokuchaev V I, Eroshenko Yu N *JCAP* (11) 059 (2013); arXiv:1308.6742
132. Doroshkevich A G *Astrophysics* **6** 320 (1970) [*Astrofizika* **6** 581 (1970)]
133. Sheth R K, Mo H J, Tormen G *Mon. Not. R. Astron. Soc.* **323** 1 (2001)
134. Shandarin S F, Doroshkevich A G, Zel'dovich Ya B *Sov. Phys. Usp.* **26** 46 (1983) [*Usp. Fiz. Nauk* **139** 83 (1983)]
135. Gurbatov S N, Saichev A I, Shandarin S F *Phys. Usp.* **55** 223 (2012) [*Usp. Fiz. Nauk* **182** 233 (2012)]
136. Shlaer B, Vilenkin A, Loeb A, arXiv:1202.1346
137. Vilenkin A, Shellard E P S *Cosmic Strings and Other Topological Defects* (Cambridge: Cambridge Univ. Press, 1994)
138. Vilenkin A, in *Inflating Horizons of Particle Astrophysics and Cosmology*: *Proc. of the Yamada Conf. LIX, June 20–24, 2005, Tokyo, Japan* (Frontiers Science Ser., No. 46, Eds H Suzuki et al.) (Tokyo: Universal Acad. Press, 2006) p. 159; hep-th/0508135
139. Vanchurin V, Olum K D, Vilenkin A *Phys. Rev. D* **74** 063527 (2006)

140. Blanco-Pillado J J, Olum K D, Shlaer B *Phys. Rev. D* **83** 083514 (2011); arXiv:1101.5173
141. Berezinsky V S, Dokuchaev V I, Eroshenko Yu N *JCAP* (12) 007 (2011)
142. Olum K D, Vilenkin A *Phys. Rev. D* **74** 063516 (2006)
143. Lynden-Bell D *Mon. Not. R. Astron. Soc.* **136** 101 (1967)
144. White S D M, in *Gravitational Dynamics*: *Proc. of the 36th Herstmonceux Conf., in Honour of Professor D. Lynden-Bell's 60th Birthday, Cambridge, UK, August 7–11, 1995* (Eds O Lahav, E Terlevich, R J Terlevich) (Cambridge: Cambridge Univ. Press, 1996) p. 121; astro-ph/9602021
145. Henriksen R N, Widrow L M *Mon. Not. R. Astron. Soc.* **302** 321 (1999)
146. Dokuchaev V I, Eroshenko Yu N *Astron. Lett.* **27** 759 (2001) [*Pis'ma Astron. Zh.* **27** 883 (2001)]
147. Dokuchaev V I, Eroshenko Yu N *Astron. Astrophys. Trans.* **22** 727 (2003)
148. Mack K J, Ostriker J P, Ricotti M *Astrophys. J.* **665** 1277 (2007)
149. Yang Y et al. *Phys. Rev. D* **84** 043506 (2011); arXiv:1109.0156
150. Saito R, Shirai S *Phys. Lett. B* **697** 95 (2011)
151. Yang Y et al. *Eur. Phys. J. Plus* **126** 123 (2011)
152. Yang Y et al. *JCAP*(12) 020 (2011)
153. Carr B J, Rees M J *Mon. Not. R. Astron. Soc.* **206** 801 (1984)
154. Bertone G, Zentner A R, Silk J *Phys. Rev. D* **72** 103517 (2005)
155. Baushev A *Inter. J. Mod. Phys. D* **18** 1195 (2009)
156. Fillmore J A, Goldreich P *Astrophys. J.* **281** 1 (1984)
157. Ricotti M, Gould A *Astrophys. J.* **707** 979 (2009)
158. Josan A S, Green A M *Phys. Rev. D* **82** 083527 (2010)
159. Bringmann T, Scott P, Akrami Y *Phys. Rev. D* **85** 125027 (2012)
160. Li F, Erickcek A L, Law N M *Phys. Rev. D* **86** 043519 (2012)
161. Yang Y et al. *Phys. Rev. D* **87** 083519 (2013); arXiv:1206.3750
162. Yang Y-P, Yang G-L, Zong H-S, arXiv:1210.1409
163. Yang Y-P, Yang G-L, Zong H-S *Europhys. Lett.* **101** 69001 (2013)
164. Berezinsky V et al. *Phys. Rev. D* **81** 103529 (2010)
165. Saslaw W C *Gravitational Physics of Stellar and Galactic Systems* (Cambridge: Cambridge Univ. Press, 1985) [Translated into Russian: *Gravitatsionnaya Fizika Zvezdnykh i Galakticheskikh Sistem* (Moscow: Mir, 1989)]
166. Gurevich A V, Zybin K P, Sirota V A *Phys. Usp.* **40** 869 (1997) [*Usp. Fiz. Nauk* **167** 913 (1997)]
167. Iocco F et al. *JCAP* (11) 029 (2011)
168. Tremaine S, Gunn J E *Phys. Rev. Lett.* **42** 407 (1979)
169. Taylor J E, Navarro J F *Astrophys. J.* **563** 483 (2001)
170. Tremaine S, Henon M, Lynden-Bell D *Mon. Not. R. Astron. Soc.* **219** 285 (1986)
171. Ryden B S *Astrophys. J.* **329** 589 (1988)
172. Ryden B S, Gunn J E *Astrophys. J.* **318** 15 (1987)
173. Hiotelis N *Astron. Astrophys.* **382** 84 (2002)
174. Ascasibar Y et al. *Mon. Not. R. Astron. Soc.* **352** 1109 (2004)
175. Ullio P et al. *Phys. Rev. D* **66** 123502 (2002)
176. Berezinsky V S, Gurevich A V, Zybin K P *Phys. Lett. B* **294** 221 (1992)
177. Berezinsky V, Bottino A, Mignola G *Phys. Lett. B* **391** 355 (1997)
178. Chung D J H, Kolb E W, Riotto A *Phys. Rev. D* **59** 023501 (1999)
179. Kuzmin V A, Tkachev I I *JETP Lett.* **68** 271 (1998) [*Pis'ma Zh. Eksp. Teor. Fiz.* **68** 255 (1998)]
180. Lyth D H, Roberts D, Smith M *Phys. Rev. D* **57** 7120 (1998)
181. Berezinsky V et al. *Phys. Rev. D* **81** 103530 (2010)
182. Bilić N, Munyaneza F, Viollier R D *Phys. Rev. D* **59** 024003 (1998)
183. Moore B et al. *Astrophys. J.* **499** L5 (1998)
184. Moore B et al. *Mon. Not. R. Astron. Soc.* **310** 1147 (1999)
185. Gao L et al. *Mon. Not. R. Astron. Soc.* **387** 536 (2008)
186. Burkert A *Astrophys. J.* **447** L25 (1995)
187. Syer D, White S D M *Mon. Not. R. Astron. Soc.* **293** 337 (1998)
188. Springel V et al. *Mon. Not. R. Astron. Soc.* **391** 1685 (2008)
189. Bullock J S et al. *Mon. Not. R. Astron. Soc.* **321** 559 (2001)
190. Lifshitz E M, Pitaevskii L P *Physical Kinetics* (Oxford: Pergamon Press, 1981) [Translated from Russian: *Fizicheskaya Kinetika* (Moscow: Nauka, 1979)]
191. Zybin K P, Vysotsky M I, Gurevich A V *Phys. Lett. A* **260** 262 (1999)
192. Widrow L M et al. *Mon. Not. R. Astron. Soc.* **397** 1275 (2009)
193. Arhipova N A et al. *Grav. Cosmol. Suppl.* **8** (Suppl. I) 66 (2002)
194. Giocoli C et al. *Mon. Not. R. Astron. Soc.* **395** 1620 (2009)
195. Angulo R E, White S D M *Mon. Not. R. Astron. Soc.* **401** 1796 (2010)
196. Oguri M, Lee J *Mon. Not. R. Astron. Soc.* **355** 120 (2004)
197. Gnedin O Y, Hernquist L, Ostriker J P *Astrophys. J.* **514** 109 (1999)
198. Fall S M, Rees M J *Mon. Not. R. Astron. Soc.* **181** 37P (1977)
199. Gnedin O Y, Ostriker J P *Astrophys. J.* **513** 626 (1999)
200. Taylor J E, Babul A *Astrophys. J.* **559** 716 (2001)
201. Diemand J, Kuhlen M, Madau P *Astrophys. J.* **667** 859 (2007)
202. Goerdt T et al. *Mon. Not. R. Astron. Soc.* **375** 191 (2007)
203. Zhao H et al. *Astrophys. J.* **654** 697 (2007)
204. Ostriker J P, Spitzer L (Jr.), Chevalier R A *Astrophys. J.* **176** L51 (1972)
205. Weinberg M D *Astron. J.* **108** 1403 (1994)
206. Eddington A S *Mon. Not. R. Astron. Soc.* **76** 572 (1916)
207. Widrow L M *Astrophys. J. Suppl.* **131** 39 (2000)
208. D'Onghia E et al. *Astrophys. J.* **709** 1138 (2010)
209. Launhardt R, Zylka R, Mezger P G *Astron. Astrophys.* **384** 112 (2002)
210. Bell E F et al. *Astrophys. J.* **680** 295 (2008)
211. Schneider A, Krauss L, Moore B *Phys. Rev. D* **82** 063525 (2010)
212. Silk J, Bloemen H *Astrophys. J.* **313** L47 (1987)
213. Berezinsky V, Kachelrieß M *Phys. Rev. D* **63** 034007 (2001)
214. Aloisio R, Berezinsky V, Kachelrieß M *Phys. Rev. D* **69** 094023 (2004)
215. Gondolo P et al. *JCAP* (07) 008 (2004)
216. Bringmann T et al. *JCAP* (07) 054 (2012)
217. Weniger C *JCAP* (08) 007 (2012)
218. Hektor A, Raidal M, Tempel E, arXiv:1207.4466
219. Bringmann T, Weniger C *Phys. Dark Universe* **1** 194 (2012); arXiv:1208.5481
220. Gorbunov D, Tinyakov P *Phys. Rev. D* **87** 081302(R) (2013); arXiv:1212.0488
221. Hisano J, Matsumoto S, Nojiri M M *Phys. Rev. Lett.* **92** 031303 (2004)
222. Profumo S *Phys. Rev. D* **72** 103521 (2005)
223. Lattanzi M, Silk J *Phys. Rev. D* **79** 083523 (2009)
224. Hooper D et al. *Phys. Rev. D* **86** 103003 (2012); arXiv:1203.3547
225. Ginzburg V L, Syrovatskii S I *The Origin of Cosmic Rays* ((Oxford: Pergamon Press, 1964)) [Translated from Russian: *Proiskhozhdenie Kosmicheskikh Luchei* (Moscow: Izd. AN SSSR, 1963)]
226. Berezinskii V S et al. *Astrophysics of Cosmic Rays* (Ed. V L Ginzburg) (Amsterdam: North-Holland, 1990) [Translated from Russian: *Astrofizika Kosmicheskikh Luchei* (Ed. V L Ginzburg) 2nd ed. (Moscow: Nauka, 1990)]
227. The GALPROP code for cosmic-ray transport and diffuse emission production, http://galprop.stanford.edu
228. Atwood W B et al. *Astrophys. J.* **697** 1071 (2009)
229. de Boer W et al. *Astron. Astrophys.* **444** 51 (2005)
230. Ackermann M et al. (The Fermi-LAT Collab.) *JCAP* (05) 025 (2010)
231. Yuan Q et al. *Phys. Rev. D* **82** 023506 (2010)
232. Pinzke A, Pfrommer C, Bergström L *Phys. Rev. D* **84** 123509 (2011)
233. Huang X, Vertongen G, Weniger C *JCAP* (01) 042 (2012)
234. Ando S, Nagai D *JCAP* (07) 017 (2012)
235. Han J et al., arXiv:1201.1003
236. Vitale V, Morselli A (for the Fermi/LAT Collab.), arXiv:0912.3828
237. Hooper D, Goodenough L *Phys. Lett. B* **697** 412 (2011)
238. Ellis J, Olive K A, Spanos V C *JCAP* (10) 024 (2011)
239. Sánchez-Conde M A et al. *JCAP* (12) 011 (2011)
240. Gao L et al. *Mon. Not. R. Astron. Soc.* **419** 1721 (2012)
241. Ackermann M et al. (The Fermi LAT Collab.) *Astrophys. J.* **747** 121 (2012)
242. Ackermann M et al. (The Fermi-LAT Collab.) *Phys. Rev. Lett.* **107** 241302 (2011)
243. Geringer-Sameth A, Koushiappas S M *Phys. Rev. Lett.* **107** 241303 (2011)
244. Feng L et al. *JCAP* (04) 030 (2012)
245. Mei S et al. *Astrophys. J.* **655** 144 (2007)
246. Olling R P, Merrifield M R *Mon. Not. R. Astron. Soc.* **311** 361 (2000)
247. Olling R P, Merrifield M R *Mon. Not. R. Astron. Soc.* **326** 164 (2001)
248. Mashchenko S, Couchman H M P, Wadsley J *Nature* **442** 539 (2006)
249. Ando S, Komatsu E *Phys. Rev. D* **73** 023521 (2006)
250. Ando S *Phys. Rev. D* **80** 023520 (2009)

251. Fornasa M et al. *Phys. Rev. D* **80** 023518 (2009)
252. Fornasa M et al. *Mon. Not. R. Astron. Soc.* **429** 1529 (2012); arXiv:1207.0502
253. Gómez-Vargas G (on behalf of the Fermi-LAT Collab.), Komatsu E *Nuovo Cimento C* **034** 327 (2011)
254. Hooper D, Serpico P D *JCAP* (06) 013 (2007)
255. Blasi P, Dick R, Kolb E W *Astropart. Phys.* **18** 57 (2002)
256. Troitsky S V *Phys. Usp.* **56** 304 (2013) [*Usp. Fiz. Nauk* **183** 323 (2013)]
257. de Boer W, Zhukov V, arXiv:0709.4576
258. Myers Z, Nusser A *Mon. Not. R. Astron. Soc.* **384** 727 (2008)
259. Natarajan A, Schwarz D J *Phys. Rev. D* **78** 103524 (2008)
260. Adriani O et al. *Phys. Rev. Lett.* **105** 121101 (2010)
261. Adriani O et al. (PAMELA Collab.) *Phys. Rev. Lett.* **106** 201101 (2011)
262. Aguilar M et al. (AMS Collab.) *Phys. Rev. Lett.* **110** 141102 (2013)
263. Diemand J et al. *Nature* **454** 735 (2008)
264. Bergström L, Bringmann T, Edsjö J *Phys. Rev. D* **78** 103520 (2008)
265. Cirelli M et al. *Nucl. Phys. B* **813** 1 (2009)
266. Cholis I et al. *Phys. Rev. D* **80** 123518 (2009)
267. Chang J et al. *Nature* **456** 362 (2008)
268. Cumberbatch D, Silk J *Mon. Not. R. Astron. Soc.* **374** 455 (2007)
269. Kane G, Lu R, Watson S *Phys. Lett. B* **681** 151 (2009)
270. Adriani O et al. *Nature* **458** 607 (2009)
271. Stozhkov Yu I, Galper A M "Iternational PAMELA experiment", Report on G T Zatsepin Seminar "Neutrino and nuclear astrophysics" February 18, 2011
272. Stozhkov Yu I *Bull. Russ. Acad. Sci. Phys.* **75** 323 (2011) [*Izv. Ross. Akad. Nauk Fiz.* **75** (3) 352 (2011)]
273. Blasi P *Phys. Rev. Lett.* **103** 051104 (2009)
274. Blasi P, Serpico P D *Phys. Rev. Lett.* **103** 081103 (2009)
275. Seto N, Cooray A *Phys. Rev. D* **70** 063512 (2004)
276. Tricarico P *Class. Quantum Grav.* **26** 085003 (2009)
277. Adams A W, Bloom J S, astro-ph/0405266
278. Lewis G F, Gil-Merino R *Astrophys. J.* **645** 835 (2006)
279. Chen J, Koushiappas S M *Astrophys. J.* **724** 400 (2010)
280. Zackrisson E et al. *Mon. Not. R. Astron. Soc.* **431** 2172 (2013)
281. Metcalf R B, Silk J *Phys. Rev. Lett.* **98** 071302 (2007); *Phys. Rev. Lett.* **98** 099903(E) (2007)
282. Siegel E R, Hertzberg M P, Fry J N *Mon. Not. R. Astron. Soc.* **382** 879 (2007)
283. Ricotti M, Ostriker J P, Mack K J *Astrophys. J.* **680** 829 (2008)
284. Freese K et al. *Astrophys. J.* **693** 1563 (2009)
285. Casanellas J, Lopes I, arXiv:1002.2326
286. Smith R J et al. *Astrophys. J.* **761** 154 (2012); arXiv:1210.1582
287. Zurek K M, Hogan C J *Phys. Rev. D* **76** 063002 (2007)
288. Koushiappas S M *AIP Conf. Proc.* **921** 142 (2007); astro-ph/0703778
289. Ando S et al. *Phys. Rev. D* **78** 101301(R) (2008)